6-2021

One Dimensional Study of Magnetoplasmadynamic Thrusters for a Potential New Class of Heavy Ion Drivers for Plasma Jet Driven Magnetoinertial Fusion

Patrick M. Brown

One Dimensional Study of Magnetoplasmadynamic Thrusters for a Potential New Class of Heavy Ion Drivers for Plasma Jet Driven Magnetoinertial Fusion

THESIS

Patrick M Brown, Civilian, USAF

AFIT-ENP-MS-21-J-025

DEPARTMENT OF THE AIR FORCE
AIR UNIVERSITY

AIR FORCE INSTITUTE OF TECHNOLOGY

Wright-Patterson Air Force Base, Ohio

AFIT-ENP-MS-21-J-025

One Dimensional Study of Magnetoplasmadynamic Thrusters for a Potential New Class of Heavy Ion Drivers for Plasma Jet Driven Magnetoinertial Fusion

THESIS

Presented to the Faculty

Department of Engineering Physics

Graduate School of Engineering and Management

Air Force Institute of Technology

Air University

Air Education and Training Command

in Partial Fulfillment of the Requirements for the

Degree of Master of Science in Applied Physics

Patrick M Brown, B.S.

Civilian, USAF

June 17, 2021

AFIT-ENP-MS-21-J-025

One Dimensional Study of Magnetoplasmadynamic Thrusters for a Potential New Class of Heavy Ion Drivers for Plasma Jet Driven Magnetoinertial Fusion

THESIS

Patrick M Brown, B.S.
Civilian, USAF

Committee Membership:

John McClory, Ph.D.
Chair

CDR Royce James, Ph.D.
Member

Jason Cassibry, Ph.D.
Member

Abstract

Plasma Jet Driven Magnetoinertial Fusion (PJMIF) requires high velocity heavy ion drivers in order to compress a magnetized target to fusion conditions. Previous work with heavy ion drivers has revealed sub-par accelerations due to plasma instabilities; thus, it is necessary to investigate new methods of heavy ion plasma acceleration. One such method is Magnetoplasmadynamic (MPD) thrusters. Past studies of these thrusters have been conducted at an initial temperature at or below the energy of full ionization. Here MPD thrusters are investigated using a Godunov type MHD solver with an Harten-Lax van Leer-D (HLLD) flux solving scheme. In these investigations, the initial pressure is fixed at $10^4 Pa$, much higher than in previous studies. It is found that velocities of $42 km/s$ are possible with an applied current of $1 kA$ and a plasma number density (number of plasma particles, electrons and ions, per cubic meter) of $2 \times 10^{20} m^{-3}$. However, this velocity decreases with increasing current over the first few microseconds of plasma injection due to the plasma being accelerated out of the chamber before the full effects of hydrodynamic expansion and acceleration can be experienced. Additionally, for MPD thrusters operating with currents ranging from $1 kA$ to $4 kA$, a number density of $2 \times 10^{22} m^{-3}$ is found to be the maximum operational plasma density for low powered MPD thrusters. At higher densities the plasma resistivity is too high and the plasma becomes trapped in the MPD channel, resulting in the plasma not escaping the MPD.

Table of Contents

Page

List of Figures

List of Tables

One Dimensional Study of Magnetoplasmadynamic Thrusters for a Potential New Class of Heavy Ion Drivers for Plasma Jet Driven Magnetoinertial Fusion

I. Introduction

1.1 Problem Background

Since the beginning of fusion energy research, there have been two dominant approaches to achieving sustained fusion reactions. First, magnetic confinement utilizes high powered electromagnets to create intense magnetic fields to contain and compress plasma to fusion energies [11]. Second, inertially confined fusion (ICF) utilizes high intensity lasers to ionize and compress targets to fusion conditions [11]. Both of these methods have been the subject of a great deal of research and many advances have been made in these approaches; but, there are still numerous problems that have yet to be solved or overcome. A third approach to plasma containment and sustained fusion reactions has recently been developed, plasma jet driven magnetoinertial fusion (PJMIF) [12]. The PJMIF process is attractive since it sits at the minimum of the cost v.s. plasma density curve; additionally the propossed sizes of PJMIF reactors are on the scale of an adult human, much smaller than other proposed schemes. A comparison of the cost vs plasma density for magnetic confinement, ICF, and PJMIF is shown in Figure 1, as well as an example of the proposed size of a basic PJMIF reactor.

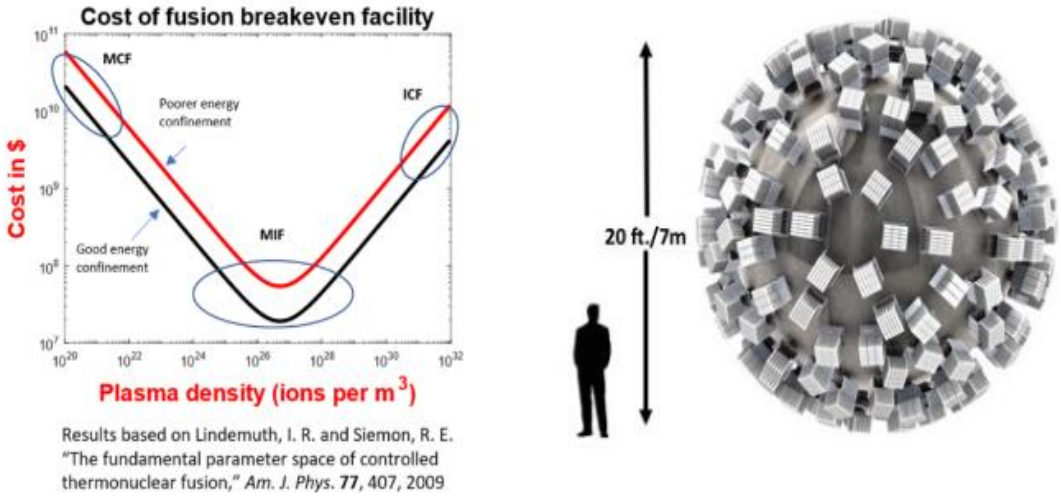

Figure 1: Right: Comparison of the cost vs plasma density for magnetic confinement, ICF, and PJMIF. Left: Example of the proposed size of a basic PJMIF reactor. Reproduced with permission from [1].

PJMIF works by using a combination of effects from both magnetic confinement and ICF. It first establishes a magnetized target of fusion fuel at the center of the device. This target usually consists of an ionized mixture of deterium-tritium plasma. Next, energetic pulses of heavy ion plasma are propelled toward the magnetized target from a series of heavy ion drivers placed on the outer surface of the reactor [13]. Once these fast moving pulses of heavy ions collide with the magnetized target at the center of the reactor, they form a spherical liner at the edge of the target surface [14]. This liner then forms a similarly spherical surface which moves inward at a high velocity and compresses the magnetized target to fusion conditions [14], as shown in Figure 2. PJMIF processes are currently under experimental investigation with the Plasma Liner Experiment (PLX) at the Los Alamos National Laboratory [12].

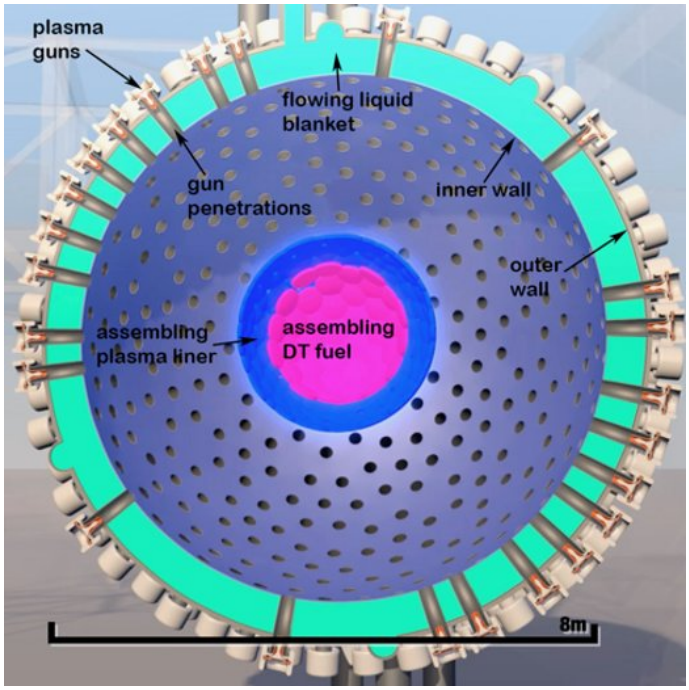

Figure 2: PJMIF design concept. Reproduced with permission from [2].

The main areas of PJMIF research currently under investigation are plasma drivers, magnetized plasma targets, and plasma compression. For the plasma driver research, Table 1 shows the required jet parameters for both the PLX experiment and fusion reactors [12]. It also shows the parameters that have been achieved by railgun and coaxial plasma accelerators [15].

Table 1: Summary of Plasma Jet Requirements for PJMIF.

Jet Parameter	Railgun Achieved	Coaxial Achieved	PLX	Fusion
Density (cm^{-3})	10^{17}	10^{15}	10^{17}	10^{18}
Velocity (km/s)	>40	90	50	50-100
Liner Species	Ar	C_2H_4	Ar, Xe	Xe

There are three main types of plasma drivers currently under investigation; de-

flagration type accelerators, snow plow type accelerators, and slab type accelerators. A deflagration type accelerator is a type of plasma driver whereby a high voltage is applied between electrodes causing an arc to form in the plasma accelerating it forward by the Lorentz force [2]. The basic layout of a deflagration type driver is shown in Figure 3.

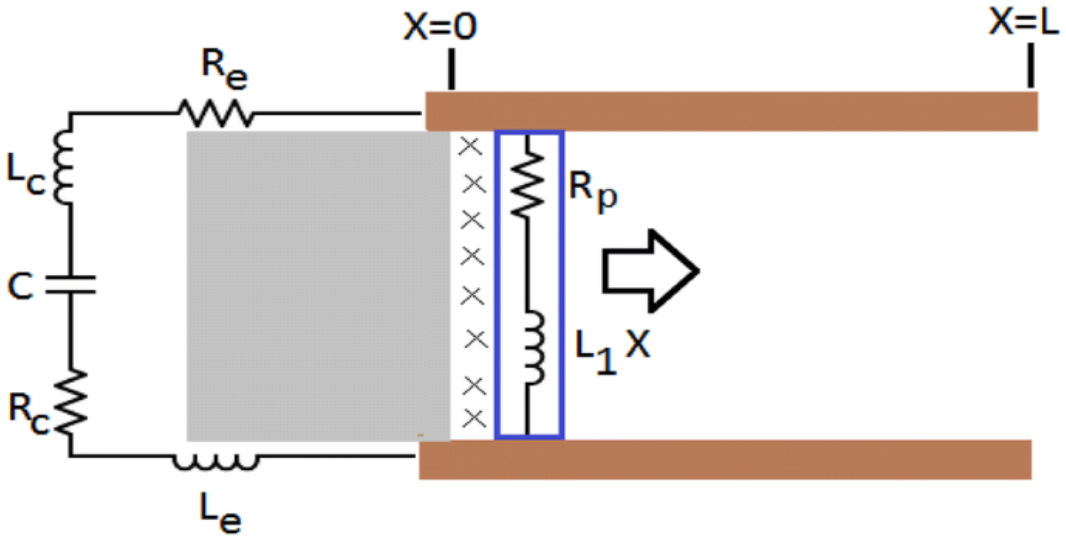

Figure 3: Basic layout of a deflagration type plasma accelerator. R represents a resistor, L for an inductor, and C for a capacitor.

The snow plow type accelerator uses a gun that is pre-filled with ionized gas. Electrons are then accelerated by the Lorentz force, which drags the electrons in the plasma by ambipolar diffusion. The dragged electrons then pull the ions in the plasma by the Lorentz force causing the plasma to be accelerated [2]. The layout of a snow plow type plasma accelerator is shown in Figure 4.

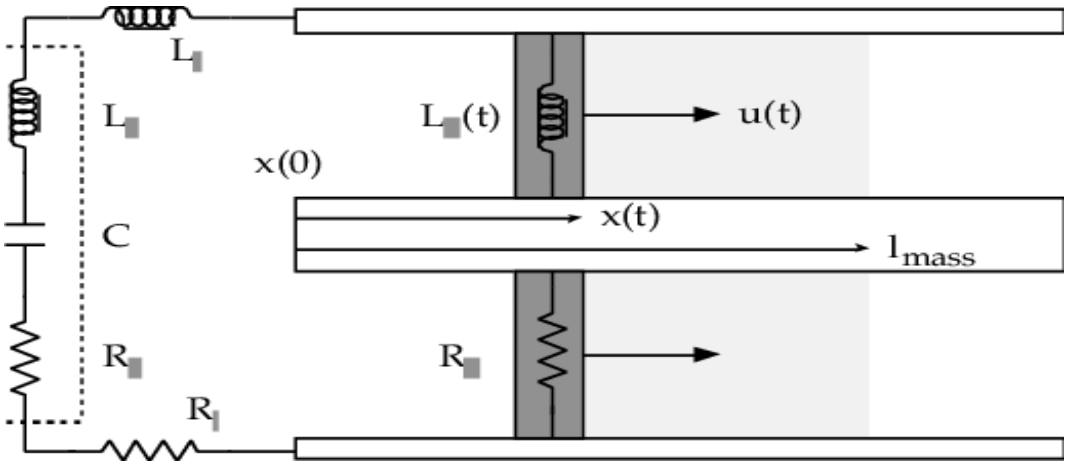

Figure 4: Basic layout of a snow plow type plasma accelerator. R represents a resistor, L for an inductor, and C for a capacitor.

The slab, or coaxial, driver method uses a fast gas injection to form an initial gas slab which is pre-ionized, forming a compact, dense, and highly collisional plasma [16]. This type of plasma accelerator is the most common accelerator design used in heavy ion driver research [17]. The layout of a coaxial plasma accelerator is shown in Figure 5.

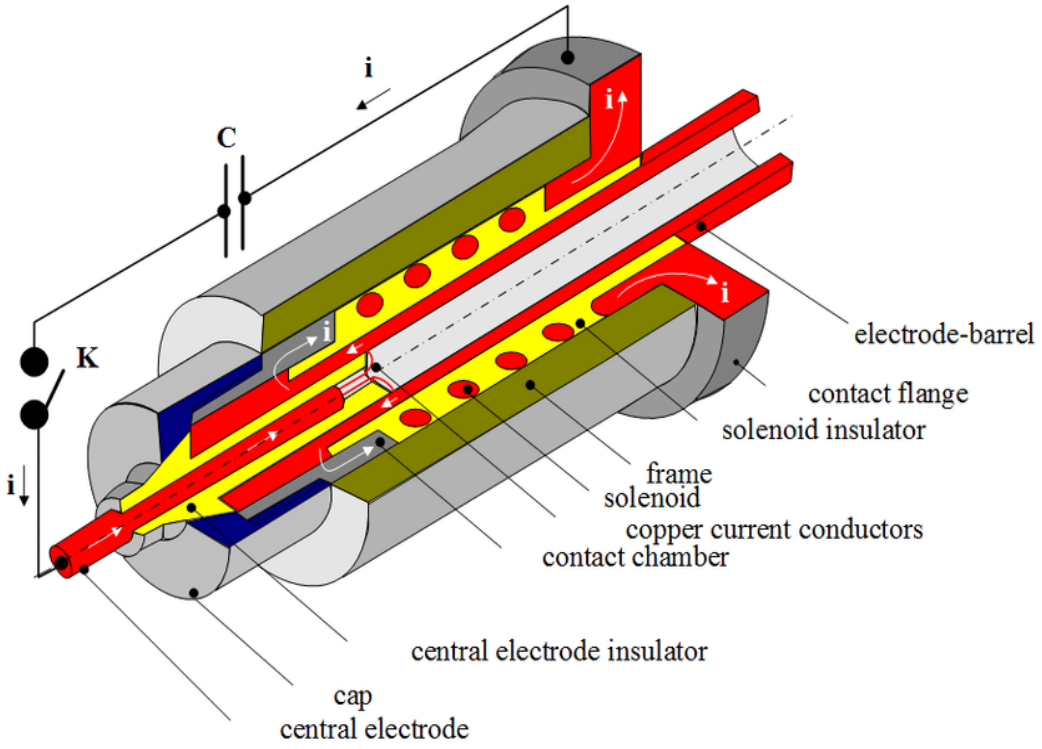

Figure 5: Basic layout of a coaxial plasma accelerator. Reproduced with permission from [3].

Of these three methods, the slab method is the only one that has exhibited the capability of achieving the accelerations necessary for sustained fusion reactions; however, the plasmas that have been accelerated by the slab method are still lacking the necessary number densities for a PJMIF heavy ion driver [16]. This method is subject to the blow-by effect, which causes the back surface of the beam to accelerate much faster than the beam front, causing the plasma's rear surface to overtake the beam front. This results in extreme beam dispersion effects [16]. The deflagration method has shown the capability of accelerating a very dense plasma, but the achieved velocities are too low for PJMIF purposes.

As a result, a new class of heavy ion plasma drivers is being considered. Specifically, a class based on the same type of acceleration mechanisms used in Hall-type

electromagnetic thrusters. The most powerful of these type of thrusters are the Magnetoplasmadynamic (MPD) thrusters [18]. The MPD thrusters use the $\overrightarrow{j} \times \overrightarrow{B}$ Lorentz force to accelerate the plasma. This is produced by the application of a current density between the central cathode and outer anode surface shown in Figure 6.

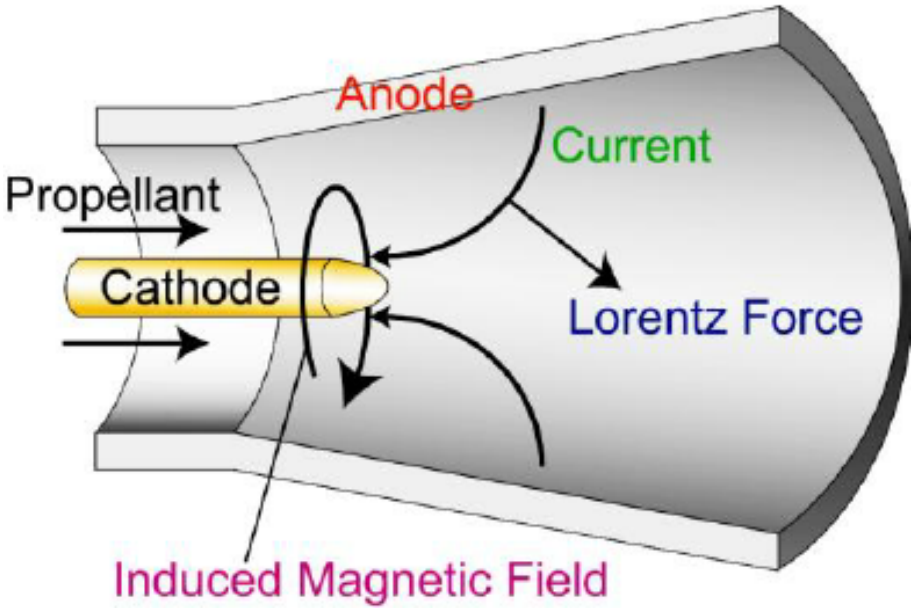

Figure 6: Typical layout of an MPD thruster. Reproduced with permission from [4].

Typically non-ionized or only slightly ionized gas is injected into the MPD thruster [19]. The effects of ionization are beyond the scope of this thesis, therefore it will be assumed that the plasma enters the thruster fully ionized [20]. A detailed analysis of MPD thrusters is provided in Chapter 2. The research efforts of this thesis are devoted to analyzing the possibility of using low powered MPD thrusters as a new method for accelerating heavy ion plasmas for PJMIF heavy ion drivers.

1.2 Research Objectives

The objective of this thesis is to provide 1D studies of low powered MPD thrusters. Specifically, this research will examine the effects of the applied current density within

the MPD thruster on the final axial velocity of the plasma and the expansion of the plasma density within the MPD chamber. This thesis will also analyze the effects of an applied solenoidal magnetic field within the MPD thruster on the axial and azimuthal components of the velocity; specifically, the generation of swirling motion within the plasma. Finally, this thesis will study the effects that the plasma number density has on the plasma motion and final plasma velocity. Specifically, the number density at which the plasma acceleration is minimized and the plasma becomes trapped in the MPD chamber. From these studies, conclusions will be drawn on the possibility of using low powered MPD thrusters as heavy ion drivers for PJMIF experiments and controlled fusion schemes.

II. Theory

2.1 Literature Review

MPD thrusters operate by the principle of electromagnetic acceleration, defined as the acceleration of a body of ionized gas by the interaction of a current driven through the ionized gas with magnetic fields established by these currents and, possibly, by external magnetic coils [5]. When compared to electrostatic acceleration mechanisms, electromagnetic acceleration is more technologically complex, thus the development of electromagnetic accelerators still requires a great deal of study. The simplest form of electromagnetic acceleration is shown in Figure 7 [5]. Here the gas has a 1D flow velocity of $\overrightarrow{u}$, scalar conductivity σ, and a current density of $\overrightarrow{j} = \sigma(\overrightarrow{E} + \overrightarrow{u} \times \overrightarrow{B})$. This establishes a force density of $\overrightarrow{f} = \overrightarrow{j} \times \overrightarrow{B}$ imparted onto the plasma.

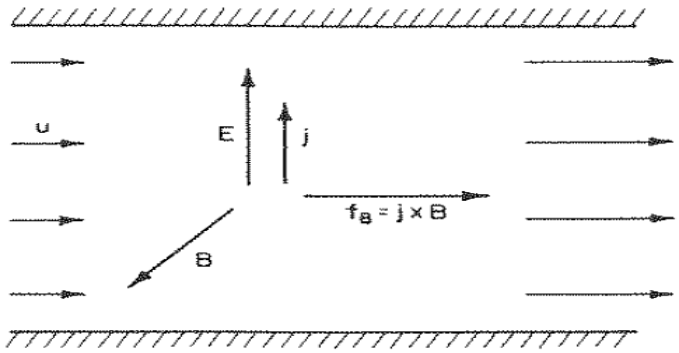

Figure 7: Basic concept of electromagnetic acceleration. Reproduced with permission from [5].

The acceleration mechanisms can also be understood from the particle point of view where the current carrying electrons attempt to follow the applied electric field, which are then turned in the stream direction by the applied magnetic field [21]. The electrons then impart momentum onto the plasma ions through collisions or microscopic polarization fields. Table 2 shows the terminal performance characteristics for

early MPD thruster development [5]. From Table 2, we know that at low current levels between $1500A$ and $2500A$, high specific impulses and thrusts are possible with heavy ion gases such as ammonia and argon.

Table 2: Terminal performance characteristics for early MPD thruster development.

Terminal Performance Characteristics					
Propellant	Hydrogen			Argon	
Current (A)	1500		2500	1500	2100
Mass Flow Rate (g/s)	0.05	0.02	0.05	0.032	0.032
Voltage	71	68	78	25	30
Thrust (N)	1.21	0.98	2.22	0.54	0.68
Specific Impulse (s)	2460	5000	4520	1720	2160
Efficiency (%)	13.7	23.6	25.4	12.1	11.5

The most useful method for analyzing the physical processes and the effect they have in the motion of the plasma is magnetogasdynamics (magnetohydrodynamics) [21]. In this method, the ionized gas is treated as a continuum fluid whose properties may be described by a set of bulk parameters and whose dynamical behavior may be described by a set of conservation laws [21]. In the continuum representation, several components of magnetogasdynamic interactions can be proposed. First, a stream wise (axial) acceleration is generated by the crossing of the radial arc current and the self generated azimuthal magnetic field. This is refered to as the electromagnetic "blowing" force [5]. Second, there may be an electromagnetic "pumping" force caused by the interaction of the axial components of the arc current and the azimuthal magnetic field. This establishes a radial gradient in the gas dynamic pressure giving

rise to a reaction force on the cathode surface [5]. Third, if a solenoidal magnetic field is applied in the axial direction swirling motion may be generated by the $j_r B_z$ or $j_z B_r$ interactions [5]. A schematic of these affects is shown in Figure 8 [5].

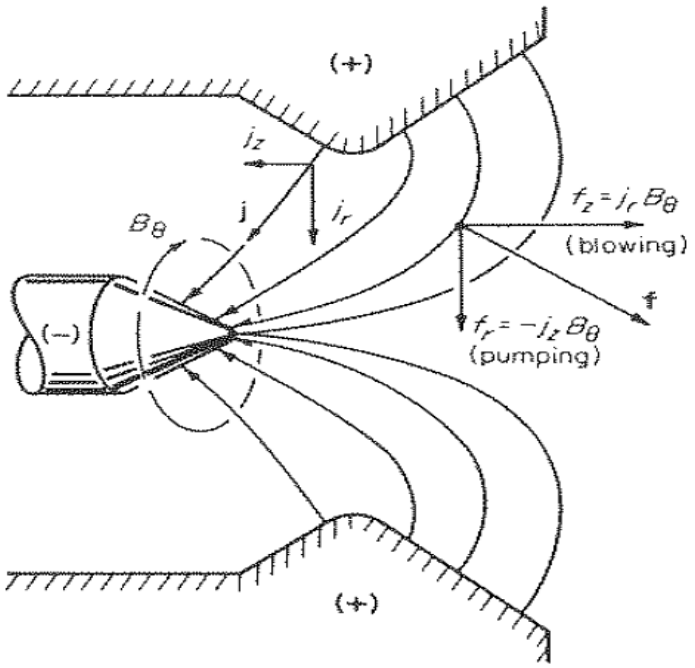

Figure 8: Schematic of MPD acceleration forces. Reproduced with permission from [5].

Many studies have been conducted on MPD thrusters without an applied magnetic field [22]. These studies have revealed that MPD thrusters are capable of achieving plasma velocities of several kilometers per second. Reference [23] shows the results of one such study. In this 2D study, as in almost all of the other studies reviewed for this research, the plasma was composed of argon gas and initially kept at a fixed temperature of $1eV$. This corresponds to the minimum temperature capable of maintaining full ionization when injected into the MPD thruster. This study also used an advanced equation of state that incorporated the effects of viscosity and drag through the use of the viscous stress tensor. It also used the Spitzer-Harm resistivity as later

described in Section 2.4. The length of the thruster was kept at $26.5cm$ and the plasma was injected at a rate of $6g/s$ [23]. It was found that the plasma obtained a velocity of $3.4km/s$ over a time of $12ms$. This shows that MPD thrusters can achieve high velocities and accelerations over a very short period of time; and therefore could potentially be of use in heavy ion plasma drivers.

The generation of swirling motion in the plasma has also been extensively studied [24]. To understand the effect of the swirling motion on the thrust of an MPD thruster, we must first review the invariance of the magnetic moment defined as [11]:

$$\mu = \frac{1}{2} m v_{\perp}^2 / B, \tag{1}$$

where $v_{\perp}$ is the velocity perpendicular to the magnetic field and B is the magnitude of the magnetic field. This quantity is called the first adiabatic invariant and is constant (invariant) along the magnetic field lines. From this invariance we can see the effect of the swirling motion and diverging magnetic field lines. Setting two points along the plasma flow, point 1 at the exit of the MPD thruster channel and point 2 within the diverging magnetic field lines, we can set the magnetic moment at both points equal to each other as in equation (2).

$$\frac{v_{\perp 1}^2}{B_1} = \frac{v_{\perp 2}^2}{B_2} \tag{2}$$

From equation (2) it is clear that a lower B_2 value results in a lower $v_{\perp 2}$ [11]. This decrease in perpendicular motion transfers energy into axial motion causing an increase in the axial velocity.

For low-powered MPD geometries, [6] presents several studies of the generation of swirling motion and the effect on thruster performance. The results of one of these studies is presented in Figure 9. This study was conducted for the Meyers

100kW MPD thruster. The discharge current applied to the MPD was $1000A$ with a propellant of argon plasma. The injection rate of the plasma was $0.1g/s$ and the range of applied magnetic fields studied was $20mT - 150mT$. The geometries of the thrusters used are shown in Table 3.

Table 3: Geometries of Meyers 100kW MPD thrusters.

Geometry	r_a (cm)	L_a (cm)	r_c (cm)	L_c (cm)
A	2.5	7.6	0.64	7.65
B	3.81	7.6	0.64	7.65
C	5.1	7.6	0.64	10.15
D	5.1	15.2	0.64	10.15
E	5.1	7.6	1.27	10.15
F	5.1	15.2	1.27	10.15
G	3.81	7.6	0.64	7.65
H	2.5-5.1	7.6	0.64	10.15

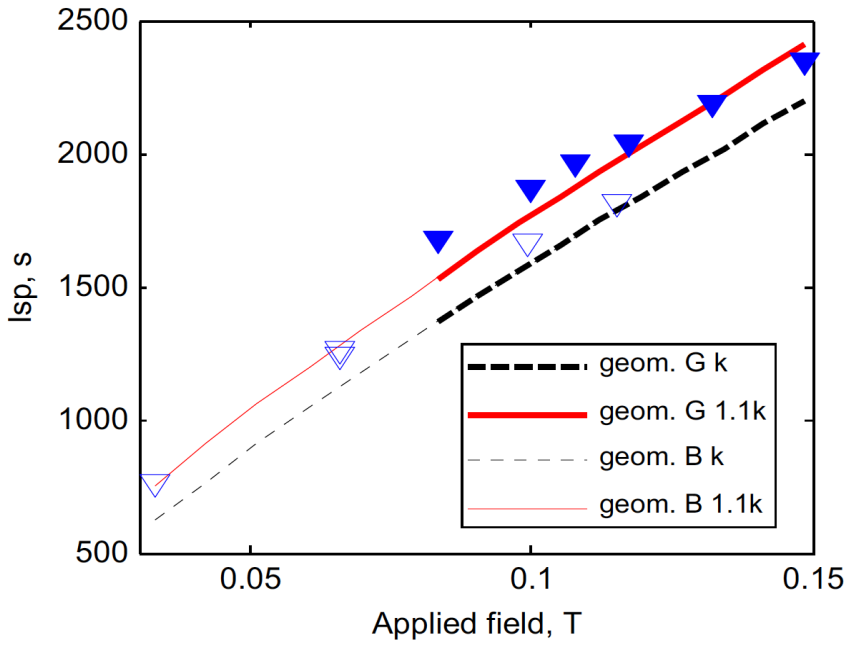

Figure 9: Specific impulse achieved by Meyers 100kW MPD thursters. Reproduced with permission from [6].

The above studies have proven that an MPD thruster is capable of accelerating a heavy ion gas with velocities on the order of several kilometers per second and are capable of achieving high specific impulse and thrust to the plasma jet. In sections 2.2 and 2.3, a basic theoretical background of the MPD thrusters used in these studies is presented, as well as the development of the magnetogasdynamic equations.

2.2 Magnetoplasmadynamic Thrusters

As stated in the Introduction, the most powerful class of Hall-type thrusters are MPD thrusters. The typical layout of an MPD thruster is shown in Figure 10.

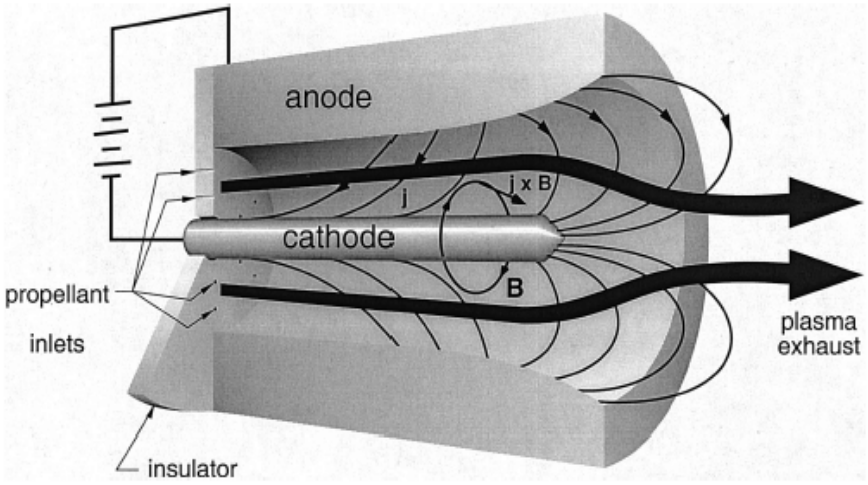

Figure 10: Typical MPD thruster layout. Reproduced with permission from [7].

The MPD thruster functions similar to that of a coaxial plasma accelerator (slab), but is not subject to the same blow-by effects [25]. The MPD thruster is composed of a cathode placed at the center of the thruster axis and an anode that forms the outer wall of the thruster. Electrons flow from the cathode to the anode, forming a current density that flows back from the anode to the cathode. This forms the $\overrightarrow{j} \times \overrightarrow{B}$ Lorentz force. This type of configuration with no externally applied magnetic field is called a self field MPD Thruster. Initially, I will analyze only this configuration. An applied field MPD is analyzed later in this thesis. The propellant used in these types of thrusters is typically a low mass plasma such as hydrogen; but numerous tests have been run using higher mass plasma, such as argon [25], and have shown great promise. In real world MPD thrusters, the plasma is injected into the MPD thruster non-ionized and the current density between the anode and cathode serves to both accelerate and ionize the plasma. Modelling this type of interaction is complicated and requires simultaneously solving the Saha equation or some other more complicated equation of state [5]; it is for this reason that in many simplified studies, including this thesis, the plasma is assumed to enter the chamber fully ionized [5].

2.2.1 Cylindrical Cathode MPD

In order to understand how an MPD thruster operates, it is necessary to first analyze the most simplified models first. The simplest MPD geometry to analyze is the cylindrical cathode MPD. This is shown in Figure 11.

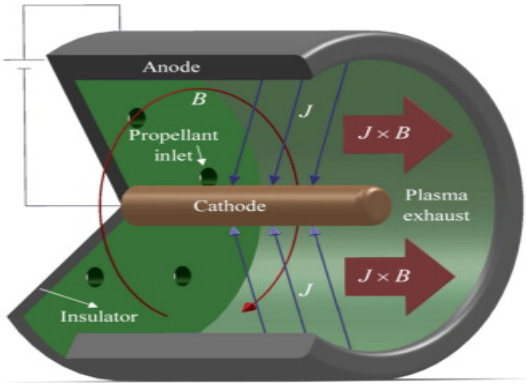

Figure 11: Cylindrical cathode MPD thruster. Reproduced with permission from [8].

From this figure the only integrating surface for Ampere's law is the cylinder surface surrounding the cathode. By applying this law, the magnetic field is given by equation (3) in cylindrical coordinates (r,θ,z); where $J = 2\pi r z_0 j_r$ is the total arc current and z_0 is the length of the cathode. This magnetic field is in the $-\hat{\theta}$ direction.

$$B_\theta = \frac{\mu_0 J}{2\pi r}(1 - \frac{z}{z_0}) \tag{3}$$

From this magnetic field the expression for the force experienced by the plasma, the thrust, is given by equation (4), where r_a is the radius of the anode and r_c is the radius of the cathode.

$$F = \frac{\mu J^2}{4\pi}(ln\frac{r_a}{r_c}) \tag{4}$$

2.2.2 Hybrid MPD

Now that the basic model of the MPD thruster has been established with the cylindrical model, let us take a look at a realistic model of an MPD thruster.

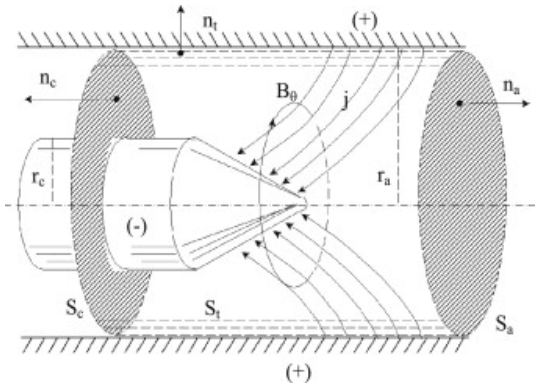

Figure 12: Integrating surfaces for the MPD thruster. Reproduced with permission from [6].

The layout of the hybrid MPD geometry is shown in Figure 12. The conical cathode has an initial radius of r_c and the conical surface follows the equation $r_c * (1 - \frac{z}{z_0})$ where z_0 is the length of the cathode. Now consider the typical situation of having a uniform current along the cathode surface where J is the total current. From Gauss's law the magnetic field of the MPD thruster is shown by equation (5) in cylindrical coordinates (r,θ,z), where the direction of the magnetic field is $-\hat{\theta}$.

$$B_\theta = \begin{pmatrix} \frac{\mu_0 J}{2\pi r_c^2} r & r < r_c \\ \\ \frac{\mu_0 J}{2\pi r} & r > r_c \end{pmatrix} \tag{5}$$

From this magnetic field the expression for the force experienced by the plasma, the thrust, is given in equation (6) where r_a is the radius of the anode and r_c is the radius of the cathode.

$$F = \frac{\mu J^2}{4\pi}(ln\frac{r_a}{r_c} + \frac{3}{4}) \tag{6}$$

2.2.3 Applied Magnetic Field MPD Thruster

There are numerous effects that an applied magnetic field can have on the plasma within the MPD chamber; but the main effect I will discuss here is the production of swirling motion within the plasma.

To analyze the swirling motion caused by the applied field, the magnetic stress tensor will be used. The force density from the electromagnetic fields onto the plasma is expressed in equation (7).

$$\overrightarrow{f} = \overrightarrow{j} \times \overrightarrow{B} = \frac{1}{\mu_0}(\nabla \times \overrightarrow{B}) \times \overrightarrow{B} \tag{7}$$

The total force exerted onto the plasma is given in equation (8).

$$\overrightarrow{F} = \int_V \overrightarrow{f} = \int_V \overrightarrow{j} \times \overrightarrow{B} \tag{8}$$

Now we can introduce the magnetic stress tensor in equation (9).

$$\frac{1}{\mu_0}(\nabla \times \overrightarrow{B}) \times \overrightarrow{B} = \nabla \bullet \mathbf{B} - \frac{1}{\mu_0}\overrightarrow{B}(\nabla \bullet \overrightarrow{B}) \tag{9}$$

Where $\mathbf{B}$ is the magnetic stress tensor. Note, $\nabla \bullet \overrightarrow{B} = 0$. The magnetic stress tensor in cylindrical coordinates is given in equation (10).

$$\frac{1}{\mu_0}\begin{bmatrix} B_r^2 - \frac{B^2}{2} & \frac{B_r B_\theta}{r} & B_r B_z \\ \frac{B_\theta B_r}{r} & \frac{B_\theta^2}{r^2} - \frac{B^2}{2r^2} & \frac{B_\theta B_z}{r} \\ B_z B_r & \frac{B_\theta B_z}{r} & B_z^2 - \frac{B^2}{2} \end{bmatrix} \tag{10}$$

In order to produce only swirling motion, the applied magnetic field inside the thrust chamber must be in the z direction. Here, the applied magnetic field inside the thrust chamber will be a constant solenoidal field. This magnetic stress tensor is then given in equation (11).

$$\frac{1}{\mu_0}\begin{bmatrix} -\frac{B^2}{2} & 0 & 0 \\ 0 & \frac{B_\theta^2}{r^2} - \frac{B^2}{2r^2} & \frac{B_\theta B_z}{r} \\ 0 & \frac{B_\theta B_z}{r} & B_z^2 - \frac{B^2}{2} \end{bmatrix} \tag{11}$$

The swirling motion results from the force applied to the plasma in the azimuthal ($\hat{\theta}$) direction. From Figure 4, noting that the magnetic field on the S_a surface is zero, the only contribution to the azimuthal force comes from $\mathbf{B} \bullet \hat{n_c}$. The azimuthal force component is then given in equation (12).

$$F_\theta = \int_{S_c} \frac{B_\theta B_z}{\mu_0 r} dS \tag{12}$$

Using the magnetic field for the hybrid self-field MPD as B_θ and taking B_z to be constant, the total azimuthal force is calculated in equation (13).

$$F_\theta = B_z J(ln\frac{r_a}{r_c} + \frac{1}{2}) \tag{13}$$

By unit analysis, this is a force per unit length; therefore, it results in angular acceleration. For simplicity we assume the plasma rotates as a rigid body. Therefore, the torque generated by the rotation is given in equation (14), where m is the mass of the plasma column with a mass flow rate of $\dot{m} = \frac{m}{\tau}$.

$$M = F_\theta \tilde{r}^2 = I\frac{\omega}{\tau} = m\tilde{r}^2\frac{\omega}{\tau} \tag{14}$$

The moment of inertia, I, is defined in equation (15).

$$I = \int_0^{r_a} \rho r^2 2\pi r dr = m\tilde{r}^2 \tag{15}$$

Therefore, the angular velocity of the plasma column can be computed in equation (16).

$$\omega = \frac{F_\theta}{\dot{m}} = \frac{B_z J}{\dot{m}}(ln\frac{r_a}{r_c} + \frac{1}{2}) \tag{16}$$

Equation (16) shows that the greater the applied magnetic field, the greater the resulting angular plasma velocity.

2.2.4 Conductivity

To understand conductivity in a plasma [26], it is necessary to look at the basic effects of the Lorentz force. We start with the Lorentz force in the laboratory frame of motion given in equation (17).

$$\overrightarrow{F} = q(\overrightarrow{E} + \overrightarrow{v} \times \overrightarrow{B}) \tag{17}$$

When transitioning to a co-moving frame with non-relativistic velocities, we know that both q and $\overrightarrow{B}$ cannot depend on the shift of reference frame. Therefore the electric field must change from one frame to another. Let $\overrightarrow{E}'$ be the electric field

in the co-moving frame with velocity $\overrightarrow{u}$ relative to the laboratory frame. Making a Galilean transformation, the electric field in the two frames are related by equation (18).

$$\overrightarrow{E} + \overrightarrow{v} \times \overrightarrow{B} = \overrightarrow{E}' + (\overrightarrow{v} - \overrightarrow{u}) \times \overrightarrow{B} \tag{18}$$

This results in equation (19).

$$\overrightarrow{E}' = \overrightarrow{E} + \overrightarrow{u} \times \overrightarrow{B}. \tag{19}$$

The frame with velocity $\overrightarrow{u}$ is chosen to be the frame moving at the plasma's mean mass velocity. Let us now consider a plasma with number density n_j of the j^{th} charged particle with charge q_j and velocity $\overrightarrow{v_j}$. The net Lorentz force per unit volume, the force density, is given in equation (20).

$$\overrightarrow{f} = \sum_j n_j q_j (\overrightarrow{E} + \overrightarrow{v_j} \times \overrightarrow{B}) \tag{20}$$

We then make the MHD approximation of a neutral plasma defined in equation (21).

$$\sum_j n_j q_j = 0 \tag{21}$$

The force density is now given by equation (22).

$$\overrightarrow{f} = \sum_j (n_j q_j \overrightarrow{v_j}) \times \overrightarrow{B} \tag{22}$$

The current density within the plasma is defined in equation (23).

$$\overrightarrow{j} = \sum_j n_j q_j \overrightarrow{v_j} \tag{23}$$

Therefore, the Lorentz force density is given in equation (24), where $\overrightarrow{v_j}$ can be the velocity of any frame chosen, including the plasma frame.

$$\overrightarrow{f} = \overrightarrow{j} \times \overrightarrow{B} \tag{24}$$

Since the electron mobility in a plasma is much higher than that of the ions, the dominant contribution to the current comes from the electrons. Therefore, in the plasma the current density is given by equation (25).

$$\overrightarrow{j} = -en_e\overrightarrow{v_e} \tag{25}$$

Now let us consider the net Lorentz force per unit volume on the swarm of electrons in the plasma given by equation (26), where ν_e is the electron collision frequency and the first equation on the right hand side is Newton's second law.

$$\overrightarrow{f_e} = -n_e m_e \overrightarrow{v_e}\nu_e = \frac{m_e\nu_e}{e}\overrightarrow{j} \tag{26}$$

This gives the current density in equation (27).

$$\overrightarrow{j} = \frac{e^2 n_e}{m_e\nu_e}(\overrightarrow{E}' + \overrightarrow{v_e} \times \overrightarrow{B}) \tag{27}$$

Therefore, the current density can be expressed in terms of the electric field and the $\overrightarrow{j} \times \overrightarrow{B}$ force as in equation (28).

$$\overrightarrow{j} = \frac{e^2 n_e}{m_e\nu_e}\overrightarrow{E}' - \frac{e}{m_e\nu_e}\overrightarrow{j} \times \overrightarrow{B} \tag{28}$$

Now we can define two important parameters, the scalar conductivity σ given in equation (29), and the Hall parameter as shown in equation (30).

$$\sigma = \frac{e^2 n_e}{m_e \nu_e} \tag{29}$$

$$\beta = \frac{eB}{m_e \nu_e} \tag{30}$$

From equation (30) we can define the Hall parameter in vector form by equation (31).

$$\vec{\beta} = \beta \frac{\vec{B}}{B} \tag{31}$$

This gives the generalized Ohm's law as shown in equation (32).

$$\sigma \overrightarrow{E}' = \overrightarrow{j} + \overrightarrow{j} \times \overrightarrow{\beta} \tag{32}$$

The Hall parameter is usually much smaller than the scalar conductivity term, so it can be ignored. Since, $\overrightarrow{E}' = \overrightarrow{E} + \overrightarrow{u} \times \overrightarrow{B}$, the generalized Ohm's law is now given in equation (33).

$$\overrightarrow{j} = \sigma(\overrightarrow{E} + \overrightarrow{u} \times \overrightarrow{B}) \tag{33}$$

Defining the resistivity to be the inverse of the conductivity, the resistivity is shown in equation (34).

$$\eta \equiv \frac{1}{\sigma} \tag{34}$$

This results in the form of Ohm's law most commonly used in the MHD formulation of plasma physics.

$$\overrightarrow{E} + \overrightarrow{u} \times \overrightarrow{B} = \eta \overrightarrow{j} \tag{35}$$

2.2.4.1 Scalar Conductivity

The scalar conductivity is shown in equation (29), but this equation is not useful in MHD formulations. Therefore more general expressions are used which are based on temperature. One of these expressions is the Spitzer-Harm formulation [21]. The Spitzer-Harm formulation of scalar conductivity is defined in equation (36) and equation (37).

$$\sigma = (1.53 * 10^{-2})\frac{T^{3/2}}{ln\Lambda} \tag{36}$$

$$ln\Lambda = ln\frac{12\sqrt{2\pi}(k_b\epsilon_0 T)^{3/2}}{q^3 n^{1/2}} \tag{37}$$

Where $ln\Lambda$ is the Coulomb logarithm, k_b is Boltzmann's constant, $q = e$ for a singly ionized plasma, and n is the number density ($\frac{\rho}{m_i+m_e}$).

2.3 Magnetohydrodynamic Equations

Several basic assumptions are applied in the single fluid description of MHD [27]. First, the plasma moves as a single fluid. The number density of electrons and ions is assumed to be equal, $n_e = n_i = n$. This provides the mass density for the plasma as in equation (38).

$$\rho = n_i m_i + n_e m_e = n(m_i + m_e) \tag{38}$$

From this expression the plasma velocity is derived in equation (39).

$$\overrightarrow{v} = \frac{1}{\rho}(n_i m_i \overrightarrow{v_i} + n_e m_e \overrightarrow{v_e}) = \frac{m_i \overrightarrow{v_i} + m_e \overrightarrow{v_e}}{m_e + m_i} \tag{39}$$

This results in the plasma current density given in equation (40).

$$\overrightarrow{j} = e(n_i \overrightarrow{v_i} - n_e \overrightarrow{v_e}) = ne(\overrightarrow{v_i} - \overrightarrow{v_e}) \tag{40}$$

The second important assumption is that of quasi-neutrality, where it is assumed that the plasma has a neutral charge at lengths greater than that of the Debye length. Next we utilize Maxwell's equations given by the following expressions.

$$\nabla \times \overrightarrow{E} = -\frac{\partial \overrightarrow{B}}{\partial t} \tag{41}$$

$$\nabla \times \overrightarrow{B} = \mu_0 \overrightarrow{j} + \frac{1}{c^2} \frac{\partial \overrightarrow{E}}{\partial t} \tag{42}$$

$$\nabla \bullet \overrightarrow{E} = 0 \tag{43}$$

$$\nabla \bullet \overrightarrow{B} = 0 \tag{44}$$

These are combined with the gas dynamic equations that describe the hydrodynamic evolution of the mass density ρ and pressure p given in equation (45) and equation (46) respectively.

$$\frac{\partial \rho}{\partial t} + \nabla \bullet (\rho \overrightarrow{v}) = 0 \tag{45}$$

$$\frac{\partial p}{\partial t} + \overrightarrow{v} \bullet \nabla p + \gamma p \nabla \bullet \overrightarrow{v} = 0 \tag{46}$$

From these, the basic equations of MHD are derived and given in equations (47) through (50), where γ is the thermodynamic constant.

$$\frac{\partial \rho}{\partial t} + \nabla \bullet (\rho \overrightarrow{v}) = 0 \tag{47}$$

$$\rho(\frac{\partial \overrightarrow{v}}{\partial t} + \overrightarrow{v} \bullet \nabla \overrightarrow{v}) + \nabla p - \frac{1}{\mu_0}(\nabla \times \overrightarrow{B}) \times \overrightarrow{B} = 0 \tag{48}$$

$$\frac{\partial p}{\partial t} + \overrightarrow{v} \bullet \nabla p + \gamma p \nabla \bullet \overrightarrow{v} = 0 \tag{49}$$

$$\frac{\partial B}{\partial t} - \nabla \times (\overrightarrow{u} \times \overrightarrow{B} - \eta \overrightarrow{j}) = 0 \tag{50}$$

For ideal MHD, the plasma is assumed to have perfect (infinite) conductivity. This means that the plasma has zero resistivity. All the equations are the same except for (50) which becomes equation (51) with the assumption of perfect conductivity.

$$\frac{\partial B}{\partial t} - \nabla \times (\overrightarrow{u} \times \overrightarrow{B}) = 0 \tag{51}$$

There are two more important equations that play a key role in the MHD models. First, we defined the plasma equation of state to be the ideal gas equation defined in equation (52).

$$p = (n_e + n_i) k_b T \tag{52}$$

Next, the internal energy of the plasma is defined in equation (53).

$$e = \frac{1}{\gamma - 1} \frac{p}{\rho} = c_v T. \tag{53}$$

It is also important to note the entropy density defined in equation (54).

$$S = p\rho^{\gamma-1}. \tag{54}$$

From these equations we derive two more important (yet interchangeable) MHD equations, which are given in equation (55) and equation (56), where $\frac{D}{Dt}$ is $\frac{\partial}{\partial t} + \overrightarrow{v} \bullet \nabla$, the adiabatic derivative.

$$\frac{De}{Dt} + (\gamma - 1)e\nabla \bullet \overrightarrow{v} = 0 \tag{55}$$

$$\frac{DS}{Dt} = 0 \tag{56}$$

2.3.1 1D Steady State Magnetohydrodynamic Equations

The MHD equations given in the section above are the most commonly used forms. They can, however, be recast into a form utilizing the temperature, T, instead of the energy density [5]. This is done through the use of the ideal gas relation between ρ, p, and T given in equation (57); where c_p is the specific heat at constant pressure and is related to the thermodynamic constant γ through the relation $\frac{c_p}{c_v} = \gamma$.

$$c_p T = \frac{\gamma}{\gamma - 1}\frac{p}{\rho} \tag{57}$$

Using this relation, the MHD equations take the forms given in equation (58), equation (59), and equation (60); with the generalized Ohm's law given in equation (61).

$$\frac{\partial \rho}{\partial t} + \nabla \bullet (\rho \overrightarrow{u}) = 0 \tag{58}$$

$$\rho(\frac{\partial \overrightarrow{u}}{\partial t} + \overrightarrow{u} \bullet \nabla \overrightarrow{u}) = -\nabla p + (\overrightarrow{j} \times \overrightarrow{B}) \tag{59}$$

$$\rho(\frac{\partial}{\partial t} + \overrightarrow{u} \bullet \nabla)(c_p T + \frac{u^2}{2}) = \frac{\partial p}{\partial t} + \overrightarrow{j} \bullet \overrightarrow{E} \tag{60}$$

$$\overrightarrow{j} = \sigma(\overrightarrow{E} + \overrightarrow{u} \times \overrightarrow{B}) \tag{61}$$

Let us assume we have a 1D flow in the $\hat{z}$ direction with current and electric field in the $\hat{r}$ direction and therefore a magnetic field only in the $\hat{\theta}$ direction (self-field MPD). In the steady state regime, equation (58) becomes equation (62).

$$\frac{d}{dz}(\rho \overrightarrow{u}) = 0. \tag{62}$$

From this, the simple solution of equation (63) is derived, where F is a constant.

$$\rho \overrightarrow{u} = F \tag{63}$$

In the steady state regime, equation (59) and equation (60) become equation (64) and equation (65).

$$\rho \overrightarrow{u} \frac{du}{dz} = -\frac{dp}{dz} + (\overrightarrow{j} \times \overrightarrow{B})_z \tag{64}$$

$$\rho \overrightarrow{u} \frac{d}{dz}(c_p T + \frac{u^2}{2}) = j_r E \tag{65}$$

For a 1D flow scenario, the generalized Ohm's law is give by equation (66).

$$j_r = \sigma(E + (\overrightarrow{u} \times \overrightarrow{B})_r). \tag{66}$$

We then solve the system of equations given by equation (64) and (65) to get the simultaneous differential equations given by equation (67) and equation (68).

$$\frac{dp}{dz} = -[\frac{p}{u} + \frac{\gamma - 1}{\gamma}F]\frac{du}{dz} + \frac{\gamma - 1}{\gamma}(j_r\frac{E}{u}) \tag{67}$$

$$\frac{du}{dz} = \frac{j_r B_\theta - \frac{\gamma-1}{\gamma}\frac{j_r E}{u}}{F[1 - (\frac{p}{uF} + \frac{\gamma-1}{\gamma})]} \tag{68}$$

These equations, along with the temperature, can be solved simultaneously by standard numerical methods. This gives the evolution of the plasma motion in the steady state regime from the solutions of the equations (67) and (68). The steady state solutions of the plasma motion can be used to gain insight into the long term operation of the MPD thrusters, which is of interest to long term space exploration missions. However, for PJMIF purposes heavy ion drivers operate in a time domain much shorter than the time required to reach the steady state regime. As such, the heavy ion drivers are subject to time dependent effects not included in the steady state regime; but this regime can still provide some useful insight.

2.3.2 1D Steady State MPD Thruster Description and Critical Ionization Velocity

For the self-field MPD thruster, there exists a magnetic field only in the $\hat{\theta}$ direction given by (5). Therefore, at the inlet of the MPD thruster, the magnitude of the magnetic field is given by equation (69).

$$B_{\theta i} = \frac{\mu_0 J}{2\pi r} \tag{69}$$

Assuming that the axial plasma velocity, v_z, is uniform over the inlet channel the thrust is given by Maecker formula, as shown in equation (70) [28].

$$T = \dot{m}[[v_z]] = \frac{\mu_0 J^2}{4\pi}(ln(\frac{r_a}{r_c}) + A) \tag{70}$$

In equation (70) $\dot{m}$ represents the assigned propellant mass flow rate, $[[v_z]] = v_{zo} - v_{zi}$ is the difference between the outlet and inlet propellant speeds, and A is a parameter dependent on the geometry of the MPD currents and electrodes. The energy balance yields equation (71) [28], where ΔV is the potential difference between the electrodes.

$$\frac{1}{2}\dot{m}[[v_z^2]] = J\Delta V \tag{71}$$

Therefore, equation (71) shows that the only requirement for obtaining higher plasma velocity is the application of a higher current. However, it is important to note that equations (70) and (71) assumed that the propellant was fully ionized when enetering the MPD chamber. This is not true in most real world MPD experiments and devices. This assumption neglects the energy lost due to the ionization of the gas by the MPD current and the acceleration dynamics within the region of ionization. In low current regimes, like those studied in this thesis, it is well known that the ionization limits the acceleration of the plasma [28]. Until the plasma is completely ionized, the plasma velocity in the steady state regime is limited to the critical ionization velocity, as shown in (72) [28], where E_{ion} is the ionization energy of the plasma and M is the atomic mass of the propellant.

$$v_{crit} = \sqrt{2E_{ion}/M} \tag{72}$$

For example, the ionization energy of xenon is $12.1298eV$ giving a critical velocity of $4222.05m/s$. This means that until the plasma in the MPD channel is fully ionized it can only achieve a maximum velocity of $4222.05m/s$. The time-dependent domain has a similar limitation from the effects of ionization, but the dynamics are not as simple as the steady state regime. However, since the MPD models considered in this thesis use simplified equations of state, it is safe to assume that a non-ionized plasma

would have the same limiting value in the time-dependent domain.

Since the plasma velocity is limited by the critical velocity, the thrust also has a limiting value given by equation (73) [28].

$$T \leq 2\dot{m}v_{crit} \tag{73}$$

Therefore, in any model of MPD thruster operation considering non-ionized injected plasma, the critical velocity represents the maximum obtainable plasma velocity and significantly limits the thrust of the MPD.

2.4 Estimate of Plasma Jet Power

The magnitude of the exit velocity at the outlet of the MPD thruster is given by equation (74); where u_e is the exit velocity of the plasma column, $\dot{m}$ is the mass flow rate, F is the force exerted onto the plasma by the MPD, J is the applied current, r_a is the anode radius, and r_c is the cathode radius.

$$u_e = \frac{F}{\dot{m}} = \frac{\mu_0 J^2}{4\pi\dot{m}}(ln\frac{r_a}{r_c} + \frac{3}{4}) \tag{74}$$

Therefore, the mass flow rate of the plasma column is given by equation (75).

$$\dot{m} = \frac{F}{u_e} = \frac{\mu_0 J^2}{4\pi u_e}(ln\frac{r_a}{r_c} + \frac{3}{4}) \tag{75}$$

The power obtained by the plasma jet at the outlet of the MPD thruster is then given by (76).

$$P_{jet} = \frac{F^2}{2\dot{m}} \tag{76}$$

From this, an estimate of the power obtained by the plasma jet for both low and high powered MPD thrusters can be obtained and is presented in Table 4.

Table 4: Power Obtained by the Plasma Jet for Both Low and High Powered MPDs.

J(A)	P_{jet}(W), $u_e = 50km/s$	P_{jet}(W), $u_e = 100km/s$
1000A	5.89×10^3	1.18×10^4
2000A	2.36×10^4	4.72×10^4
3000A	5.31×10^4	1.06×10^5
4000A	9.43×10^4	1.89×10^5
10000A	5.89×10^5	1.18×10^6
15000A	1.33×10^6	2.65×10^6
20000A	2.36×10^6	4.72×10^6

From Table 4, it is clear that in order to reach MW levels of plasma jet power, high powered MPD thrusters are required. However, low powered MPD thrusters are shown to be capable of achieving high powered plasma jets, even with an exit velocity of $100km/s$. Therefore, low powered MPD thrusters show promise as a potential new class of heavy ion drivers. This thesis will be devoted to investigating the possibility of using low powered MPD thrusters as heavy ion drivers for the PLX experiment and PJMIF.

2.5 Summary of the MPD Thrusters Studied in this Thesis

As stated in Section 2.1, low powered MPD thrusters are capable of achieving plasma velocities on the order of several kilometers per second. These velocities are too small to be used in a heavy ion driver for PJMIF purposes. In order to increase the plasma velocities obtained by low power MPD thrusters, this thesis will study the

effects of maintaining the initial plasma at a high initial pressure. Specifically, the injected plasma will be kept at an initial pressure of $10^4 Pa$. Using the ideal gas law, the temperature of $1keV$ as used in Section 2.1 corresponds to an initial pressure of $32.02Pa$, much lower than the pressures studied in this thesis. A plasma composed of xenon gas, rather than argon, is studied in this thesis. Xenon has not been studied to the same degree as fuel for low powered MPD thrusters. This thesis will also study the effects of low power solenoidal magnetic fields on the plasma motion in order to study the generation and affects of the swirling motion.

The Hybrid MPD model of Section 2.2.2 represents the self-field magnetic field created by driving a current density through the plasma. The applied axial solenoidal magnetic fields are predicted to generate a swirling motion within the plasma as described in Section 2.2.3. The resistivity felt by the plasma will be modelled as the scalar value described in Section 2.2.4. As described in Section 2.1, the most commonly used method for modelling the plasma motion in an MPD thruster is the set of MHD equations described in Section 2.3. These equations will be used to model the plasma motion in this thesis. This research effort will study two regimes of plasma motion. The first is the 1D steady state regime as described in Section 2.3.1. The second is the 1D time dependent domain, which is modelled by the full set of MHD equations presented in Section 2.3. The methods used for numerically modeling the plasma motion described by this theory is presented in Chapter 3.

III. Numerical Methods

3.1 Numerically Solving 1D Steady State MHD

The 1D steady state equations can be simultaneously solved with standard numerical algorithms. For this thesis a fifth-order Runge-Kutta method was chosen because it is well suited for a small step size, which is required in order to maintain a high accuracy for the simulation results [29]. This method is summarized in equation (77).

$$x(t+h) = x(t) + \frac{16}{135}K_1 + \frac{6656}{12825}K_3 + \frac{28561}{56430}K_4 - \frac{9}{50}K_5 + \frac{2}{55}K_6 \tag{77}$$

$$K_1 = hf(t, x)$$

$$K_2 = hf(t + \frac{1}{4}h, x + \frac{1}{4}K_1)$$

$$K_3 = hf(t + \frac{3}{8}h, x + \frac{3}{32}K_1 + \frac{9}{32}K_2)$$

$$K_4 = hf(t + \frac{12}{13}h, x + \frac{1932}{2197}K_1 - \frac{7200}{2197}K_2 + \frac{7296}{2197}K_3)$$

$$K_5 = hf(t + h, x + \frac{439}{216}K_1 - 8K_2 + \frac{3680}{513}K_3 - \frac{845}{4104}K_4)$$

$$K_5 = hf(t + \frac{1}{2}h, x - \frac{8}{27}K_1 + 2K_2 - \frac{3544}{2565}K_3 + \frac{1859}{4104}K_4 - \frac{11}{50}K_5)$$

In these equations, $x(t)$ represents the time dependent variable for which we wish to find a numerical solution. The function $f(t, x)$ is the differentiable function that determines the solution for $x(t)$ and h is the step size chosen to be small enough so as to minimize any errors present in the system. The full origins and derivation of these systems of equations is found in Ref [29].

3.2 Conservative MHD Equations

The MHD equations are difficult to solve without any further simplifications of the algebra [30]. In this section, I will describe how these simplifications are made and how they affect the numerical algorithms. For now let us use the ideal MHD equations. The resistive solutions will be described later on in this chapter.

3.2.1 Conservative Equations

A system of quasi-linear PDEs is said to be in conservative form if all terms can be written as a generalized divergence of the dependent variables or simple functions of them, i.e. in the form of equation (78) [30].

$$\frac{\partial}{\partial t}(...) + \nabla \bullet (...) = 0 \tag{78}$$

When equations are written in this form it is simple to obtain local and global conservation laws for them. It is also simple to obtain jump conditions at shock points. Numerical algorithms that solve these types equations are very powerful and usually very accurate.

3.2.2 Conservative MHD

Let us now derive the conservative form of the MHD equations. The ideal MHD equations in cgs units are given in equations (79) - (85) [31].

$$\frac{\partial \rho}{\partial t} + \nabla \bullet (\rho \overrightarrow{v}) = 0 \tag{79}$$

$$\rho \frac{\partial \overrightarrow{v}}{\partial t} + \rho \overrightarrow{v} + \nabla p - \frac{1}{c} \overrightarrow{j} \times \overrightarrow{B} = 0 \tag{80}$$

$$\overrightarrow{j} = \frac{c}{4\pi}\nabla \times \overrightarrow{B} \tag{81}$$

$$p = (\gamma - 1)\rho e \tag{82}$$

$$\frac{\partial e}{\partial t} + \overrightarrow{v} \bullet (\nabla e) + (\gamma - 1)e\nabla \bullet \overrightarrow{v} = 0 \tag{83}$$

$$\frac{\partial \overrightarrow{B}}{\partial t} + c\nabla \times \overrightarrow{E} = 0 \tag{84}$$

$$\overrightarrow{E} = -\frac{1}{c}\overrightarrow{v} \times \overrightarrow{B} \tag{85}$$

Equation (79) is already in conservative form (mass conservation). The rest, however, must be manipulated. A few vector identities useful for this purpose are given in equations (86) - (89).

$$\nabla \bullet (\overrightarrow{a}\,\overrightarrow{b}) = \overrightarrow{a}\nabla \bullet \overrightarrow{b} + \overrightarrow{b}\nabla \bullet \overrightarrow{a} \tag{86}$$

$$\overrightarrow{a} \times (\nabla \times \overrightarrow{b}) = (\nabla\,\overrightarrow{b}) \bullet \overrightarrow{a} - \nabla \bullet (\overrightarrow{a}\,\overrightarrow{b}) - \overrightarrow{b}\nabla \bullet \overrightarrow{a} \tag{87}$$

$$\nabla \times (\overrightarrow{a} \times \overrightarrow{b}) = \nabla \bullet (\overrightarrow{b}\,\overrightarrow{a} - \overrightarrow{a}\,\overrightarrow{b}) \tag{88}$$

$$\nabla(\overrightarrow{a} \bullet \overrightarrow{b}) = (\nabla\,\overrightarrow{a}) \bullet \overrightarrow{b} + (\nabla\,\overrightarrow{b}) \bullet \overrightarrow{a} \tag{89}$$

The first term in equation (80), the momentum equation, is then converted into equation (90).

$$\rho\frac{\partial\overrightarrow{v}}{\partial t}+\rho\overrightarrow{v}\bullet\nabla\overrightarrow{v}=\frac{\partial}{\partial t}(\rho\overrightarrow{v})+\nabla\bullet(\rho\overrightarrow{v}\overrightarrow{v}) \tag{90}$$

The last term in the momentum equation then given by equation (91).

$$-\overrightarrow{j}\times\overrightarrow{B}=\frac{c}{4\pi}\nabla(\frac{1}{2}B^2)-\frac{c}{4\pi}\nabla\bullet(\overrightarrow{B}\overrightarrow{B}) \tag{91}$$

Alfven's equation then becomes:

$$\nabla\times\overrightarrow{E}=-\frac{1}{c}\nabla\times(\overrightarrow{v}\times\overrightarrow{B})=\frac{1}{c}\nabla\bullet(\overrightarrow{v}\overrightarrow{B}-\overrightarrow{B}\overrightarrow{v}). \tag{92}$$

In order to conserve total energy we need to manipulate several equations. The first is to take $\overrightarrow{v}\bullet$ Momentum Equation as in equation (93).

$$\frac{\partial}{\partial t}(\frac{1}{2}\rho v^2)+\nabla\bullet(\frac{1}{2}\rho v^2\overrightarrow{v})+\overrightarrow{v}\bullet\nabla p-\frac{1}{c}\overrightarrow{v}\bullet\overrightarrow{j}\times\overrightarrow{B}=0 \tag{93}$$

Now we take ρ times the internal energy equation as in equation (94).

$$\frac{\partial}{\partial t}(\rho e)+\nabla\bullet(\rho e\overrightarrow{v})+p\nabla\bullet\overrightarrow{v}=0 \tag{94}$$

Finally we take $\frac{1}{4\pi}\overrightarrow{B}\bullet$ Alfven's Equation as in equation (95).

$$\frac{\partial}{\partial t}(\frac{1}{2}\frac{B^2}{4\pi})+\frac{1}{4\pi}\nabla\bullet[\overrightarrow{B}\bullet\overrightarrow{B}\overrightarrow{v}-\overrightarrow{v}\bullet\overrightarrow{B}\overrightarrow{B}]+\frac{1}{c}\overrightarrow{v}\bullet\overrightarrow{j}\times\overrightarrow{B}=0 \tag{95}$$

Combining equations (93), (94), and (95) gives the conservative form of the energy equation as expressed in equation (96).

$$\frac{\partial}{\partial t}(\frac{1}{2}\rho v^2+\rho e+\frac{1}{2}\frac{B^2}{4\pi})+\nabla\bullet[(\frac{1}{2}\rho v^2+\rho e+p+\frac{B^2}{4\pi})\overrightarrow{v}-\overrightarrow{v}\bullet\frac{1}{4\pi}\overrightarrow{B}\overrightarrow{B}]=0 \tag{96}$$

Alfven's equation becomes:

$$\frac{\partial \overrightarrow{B}}{\partial t} + \nabla \bullet (\overrightarrow{v}\overrightarrow{B} - \overrightarrow{B}\overrightarrow{v}) = 0. \tag{97}$$

Finally the momentum equation is given by equation (98), where $\hat{I}$ is the identity matrix.

$$\frac{\partial}{\partial t}(\rho \overrightarrow{v}) + \nabla \bullet [\rho \overrightarrow{v}\overrightarrow{v} + (p + \frac{1}{2}\frac{B^2}{4\pi})\hat{I} - \frac{1}{4\pi}\overrightarrow{B}\overrightarrow{B}] = 0 \tag{98}$$

Combining these equations together and converting to Heaviside-Lorentz units we obtain the conserved ideal MHD equations.

$$\frac{\partial \rho}{\partial t} + \nabla \bullet (\rho \overrightarrow{v}) = 0 \tag{99}$$

$$\frac{\partial \rho \overrightarrow{v}}{\partial t} + \nabla \bullet (\rho \overrightarrow{v}\overrightarrow{v} + p_T \hat{I} - \overrightarrow{B}\overrightarrow{B}) = 0 \tag{100}$$

$$\frac{\partial e}{\partial t} + \nabla \bullet ((e + p_T)\overrightarrow{v} - (\overrightarrow{v} \bullet \overrightarrow{B})\overrightarrow{B}) = 0 \tag{101}$$

$$\frac{\partial \overrightarrow{B}}{\partial t} + \nabla \bullet (\overrightarrow{v}\overrightarrow{B} - \overrightarrow{B}\overrightarrow{v}) + \nabla\psi = 0 \tag{102}$$

$$\frac{\partial \psi}{\partial t} + c_h^2 \nabla \bullet \overrightarrow{B} = -(\frac{c_h^2}{c_p^2})\psi \tag{103}$$

In these equations $p_T = p + B^2/2$ is the total pressure, $e = p//(\gamma - 1) + \rho v^2/2 + B^2/2$ is the total energy density, $\gamma = 5/3$, and ψ is a virtual potential for hyperbolic divergence cleaning. In other words, ψ is used to ensure that $\nabla \bullet \overrightarrow{B} = 0$ within acceptable error. The hyperbolic divergence cleaning method is not necessary for 1D

simulations, but is provided here for context [32].

3.3 Numerically Solving the Conservative MHD Equations

The main purpose of numerically solving the above equations is to create a flux conserving scheme [33]. Let us start with the 1D problem. The first step is to create cells out of the grid. The cell centers are now called grid points located at x_i and the location of the cell walls is given by equation (104).

$$x_{i+1/2} = \frac{1}{2}(x_i + x_{i+1}) \tag{104}$$

Assume that we have a constant grid spacing dx between cell edges and cell centers. For our conserved quantities q_i^n the total amount in each cell is $Q_i^n = q_i^n V$. We formulate the fluxes of these quantities at the cell edges/interfaces, $f_{i+1/2}$, which is shown in equation (105), where S is the surface area of the cell interface.

$$\frac{\partial Q_i}{\partial t} = (f_{i-1/2} - f_{i+1/2})S \tag{105}$$

The discrete form of equation (105) is shown in equation .

$$\frac{Q_i^{n+1} - Q_i^n}{dt} = (f_{i-1/2}^{n+1/2} - f_{i+1/2}^{n+1/2})S \frac{\partial Q_i}{\partial t} = (f_{i-1/2} - f_{i+1/2})S \tag{106}$$

Therefore, the conserved quantities are given by equation (107).

$$\frac{q_i^{n+1} - q_i^n}{dt} = \frac{f_{i-1/2}^{n+1/2} - f_{i+1/2}^{n+1/2}}{dx} \tag{107}$$

In explicit notation this is given by equation (108).

$$q_i^{n+1} = q_i^n + \frac{dt}{dx}(f_{i-1/2}^{n+1/2} - f_{i+1/2}^{n+1/2}). \tag{108}$$

There now remains two main questions. How do we solve the fluxes at each cell interface and how do we advance in time?

3.3.1 MUSCL/Total Variation Diminishing (TVD) Schemes

Since each of the conserved variables is calculated at the cell centers, it is necessary to interpolate their values to the cell edges for calculation of the fluxes. This requires the use of a numerical assumption. One method of accomplishing interpolation is to assume a piecewise linear model [34]. This creates a subgrid model where each cell has its own linear or higher order interpolation from the cell center to the cell edges. These schemes are called Monotonic Upwind-centered Scheme for Conservation Laws (MUSCL) schemes. Within each cell, the state at the beginning of the time step is given by equation (109), where σ_i^n is some slope which interpolates the value to the edge.

$$q(x, t = t_n) = q_i^n + \sigma_i^n(x - x_i) \qquad x_{i-1/2} < x < x_{i+1/2} \tag{109}$$

Assume for the moment that the velocity u is greater than 0 and constant. At the interface, the conserved flux is given by equation (110).

$$f_{i-1/2}(t) = uq_{i-1}^n + u\sigma_{i-1}^n(\frac{1}{2}dx - u(t - t_n)) \tag{110}$$

Equation (110) is then averaged over a time step dt, which results in equation (111).

$$uq_{i-1}^n + \frac{1}{2}u\sigma_{i-1}^n(dx - udt) \tag{111}$$

Therefore the difference between the two averaged fluxes $f_{i+1/2}$ and $f_{i-1/2}$ is:

$$u(q_i^n - q_{i-1}^n) + \frac{1}{2}u(\sigma_i^n - \sigma_{i-1}^n)(dx - udt). \tag{112}$$

Therefore, in discrete notation equation (112) is given by equation (113).

$$q_i^{n+1} = q_i^n - \frac{udt}{dx}(q_i^n - q_{i-1}^n) - \frac{udt}{dx}\frac{1}{2}(\sigma_i^n - \sigma_{i-1}^n)(dx - udt) \tag{113}$$

Since the conserved variables are cell centered values, but the flux functions are evaluated at the cell interfaces, we need a way of interpolating the cell centered functions to cell edges. When these functions are interpolated a new maximum or minimum cannot be created, otherwise this will cause non-physical oscillations in the plasma motion. One way to accomplish this is through the use of slope limiter functions as previously described. These functions interpolate the cell centered values to the cell edges, while ensuring non-physical oscillations are not created. The question now is what do we chose for the limiter function?

3.3.1.1 Minmod Limiter

The choice made in this thesis is the minmod limiter [35]. The minmod limiter is defined in equation (114).

$$\sigma_i^n = minmod(\frac{q_i^n - q_{i-1}^n}{\delta x}, \frac{q_{i+1}^n - q_i^n}{\delta x}) \tag{114}$$

The $minmod(a, b)$ function is defined in equation (115).

$$minmod(a,b) = \begin{pmatrix} a & if & \mid a \mid < \mid b \mid and & ab > 0 \\ b & if & \mid a \mid > \mid b \mid and & ab > 0 \\ 0 & if & ab \leq 0 & \end{pmatrix} \tag{115}$$

Another way of looking at this limiter function is through the definition in equation (116) and equation (117); where $minmod(a, b) = \frac{sign(a)+sign(b)}{2} min(\mid a \mid, \mid b \mid)$.

$$u^{-}_{i+1/2} = u_i + \frac{1}{2} minmod(u_{i+1} - u_i, u_i - u_{i-1}) \tag{116}$$

$$u^{+}_{i+1/2} = u_i - \frac{1}{2} minmod(u_{i+2} - u_{i+1}, u_{i+1} - u_i) \tag{117}$$

These two definitions are equivalent and the second one is implemented in the code. The reason this limiter was chosen is that it provides second order accuracy for the interpolation scheme. The minmod limiter was also chosen because it is the standard limiter function used in these types of solvers, as well as in previous studies conducted with this specific code base.

3.3.1.2 Second Order Runge-Kutta TVD Method

Now that we have defined a method for interpolating the cell centered values of the conserved variables to the cell interfaces, we will define a second order accurate method for calculating the time change of the conserved variables. This will be accomplished through the use of the Total Variation Diminishing method [34]. The Total Variation is a measure of the oscillations in a simulation and is defined in equation (118).

$$TV(u) = \sum_j \mid u_{j+1} - u_j \mid \tag{118}$$

A Total Variation Diminishing (TVD) scheme is one that has the property of:

$$TV(u^{n+1}) < TV(u^n). \tag{119}$$

The equation we wish to solve is defined in equation (120).

$$u_t = L(u) \tag{120}$$

In 1D MHD this equation is given by equation (121).

$$u_t = -f(u)_x \tag{121}$$

The TVD second order Runga-Kutta method is defined in equation (122) and equation (123). This is a two step method. The first step is performed as an initial guess step, the result of which ($u^{(1)}$) is then used in the second step to produce the final result (u^{n+1}) for the full time step.

$$u^{(1)} = u^n + dtL(u^n) \tag{122}$$

$$u^{n+1} = \frac{1}{2}u^n + \frac{1}{2}u^{(1)} + \frac{1}{2}dtL(u^n) \tag{123}$$

Since the slope limiter is chosen to be second order accurate, it is then necessary to chose a time advancing method that is also second order accurate. This TVD scheme provides a second order accurate method for advancing the conserved variables in time.

3.3.2 Flux Solvers

Now that we have chosen a method for interpolating the conserved variables from the cell centers to the cell interfaces and a method for advancing the conserved variables in time, it is necessary to chose a method for solving the spatial variation of the MHD equations. There are numerous methods for doing this, but most are beyond the scope of this thesis. For this thesis the Godunov method was selected [9]. This is a well known, and a relatively easy to understand, numerical method. This

method functions by considering the solution to the Riemann problem at each cell interface. A full treatment of the Riemann problem is beyond the scope of this thesis, but a general overview is now provided. At each cell interface, it is assumed that the plasma encounters a shock surface. At these surfaces the shock waves travel along the characteristic surfaces defined by the eigenvalues of the conservative MHD equations defined in section 3.3.2.2. At each of these cell interfaces the jump conditions are then used to solve for the spatial variation of the plasma motion across each interface. The full collection (unity) of the plasma motion across each interface is then used as the solution of the spatial variation of the MHD equations for a single time step. As stated in Section 3.3.1.2, the TVD scheme requires two time step calculations for a second order accurate scheme. As a result the Godunov method is solved twice, once per each TVD step, for a full step in time. The full Godunov method is explained below.

3.3.2.1 Godunov Method

Figure 13 shows the typical layout of the standard Godunov Numerical Scheme.

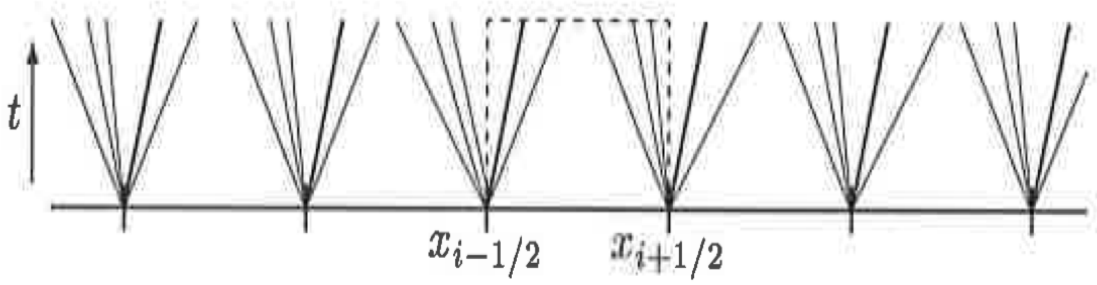

Figure 13: Layout of the Godunov scheme. Reproduced with permission from [9].

The Godunov method considers the numerical solution of the hyperbolic conservation laws defined in equation (124).

$$\overrightarrow{u} + \overrightarrow{f}(\overrightarrow{u})_x = 0 \tag{124}$$

This method considers the numerical values of the solutions $\overrightarrow{u}_i^n$ to be the cell averages of the analytical function at the time step n,

$$\overrightarrow{u}_i^n = \frac{1}{dx}\int_{x_{i-1/2}}^{x_{i+1/2}} \overrightarrow{u}(x, ndt)dx. \tag{125}$$

This assumes a piece-wise constant data representation. At each cell interface the associated Riemann problem is solved and the unity of all Riemann problems are used to update the numerical solution at that time step. We can then define the numerical flux as shown in equation (126) and equation (127).

$$\overrightarrow{f}_{i-1/2}^n = \overrightarrow{f}(\overrightarrow{u}_{i-1}^n, \overrightarrow{u}_i^n) = \frac{1}{dt}\int_{t^n}^{t^{n+1}} \overrightarrow{f}(\overrightarrow{u}(x_{i-1/2}, t))dt \tag{126}$$

$$\overrightarrow{f}_{i+1/2}^n = \overrightarrow{f}(\overrightarrow{u}_{i+1}^n, \overrightarrow{u}_i^n) = \frac{1}{dt}\int_{t^n}^{t^{n+1}} \overrightarrow{f}(\overrightarrow{u}(x_{i+1/2}, t))dt \tag{127}$$

With these two numerical fluxes defined, we can then state the Godunov method in conservative, discrete, form shown in equation (128).

$$\overrightarrow{u}_i^{n+1} = \overrightarrow{u}_i^n - \frac{dt}{dx}(\overrightarrow{f}_{i+1/2}^n - \overrightarrow{f}_{i-1/2}^n) \tag{128}$$

Now that the discrete form of the Godunov method has been established, it is necessary to develop a method for numerically calculating the flux variation across each cell interface. There are numerous methods for accomplishing this, most of which are beyond the scope of this thesis. In the next section, I will cover one such method used to solve the Riemann problem at each cell interface, the HLLD solver.

3.3.2.2 The HLLD Solver

This subsection reviews the derivation and analysis of the HLLD solver presented in [36]. The typical layout of the HLLD flux solver method is shown in Figure 14.

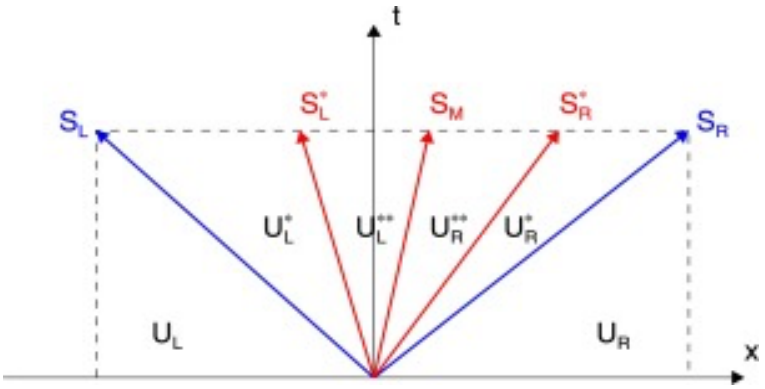

Figure 14: The HLLD scheme. Reproduced with permission from [10].

Consider the ideal 1D conservative MHD equations in the $\hat{x}$ direction given by equation (129).

$$\frac{\partial \overrightarrow{U}}{\partial t} + \frac{\partial \overrightarrow{F}}{\partial x} = 0 \tag{129}$$

The conserved variables, U, is are given in equation (130); and the fluxes of these variables are given in equation (131).

$$\overrightarrow{U} = \begin{pmatrix} \rho \\ \rho u \\ \rho v \\ \rho w \\ B_y \\ B_z \\ e \end{pmatrix} \tag{130}$$

$$\overrightarrow{F} = \begin{pmatrix} \rho u \\ \rho u^2 + p_T - B_x^2 \\ \rho v u - B_x B_y \\ \rho w u - B_x B_z \\ B_y u - v B_x \\ B_z u - w B_x \\ (e + p_T)u - B_x(\overrightarrow{v} \bullet \overrightarrow{B}) \end{pmatrix} \tag{131}$$

These equations have seven eigenvalues: two Alvfen waves (c_a), four magneto-sonic waves (two fast and two slow) ($c_{f,s}$), and an entropy wave (c_u). The eigenvalues correspond to the speeds of these waves; which are then presented in equation (132), equation (133), and equation (134):

$$c_a = \frac{B_x}{\sqrt{\rho}} \tag{132}$$

$$c_{f,s} = \sqrt{\frac{\gamma p B^2 + \sqrt{(\gamma p + B^2)^2 - 4\gamma p B_x^2}}{2\rho}} \tag{133}$$

$$c_u = u \tag{134}$$

We assume that the normal velocity is constant over the Riemann fan in Figure 14. It is assumed in [36] that the normal velocity corresponds to the entropy (contact) wave, S_M. This also leads to the result that the total pressure is constant over the Riemann fan. Slow shocks cannot be formed inside the Riemann fan; however rotational discontinuities can be formed and propagate along with the Alfven waves. The Reimann fan is then divided into four intermediate states: $\overrightarrow{U}_L^*$, $\overrightarrow{U}_L^{**}$, $\overrightarrow{U}_R^{**}$, and $\overrightarrow{U}_R^*$. The choice of S_M is given by equation (135) [36].

$$S_M = \frac{(S_R - u_R)\rho_R u_R - (S_L - u_L)\rho_L u_L - p_{T_R} + p_{T_L}}{(S_R - u_R)\rho_R - (S_L - u_L)\rho_L} \tag{135}$$

The constant normal velocity leads to:

$$u_L^* = u_L^{**} = u_R^{**} = u_R^* = S_M. \tag{136}$$

This also leads to a constant total pressure across the Riemann fan given by equation (137).

$$p_{T_L}^* = p_{T_L}^{**} = p_{T_R}^{**} = p_{T_R}^* = p_T^* \tag{137}$$

From equation (137), the total pressure is given by equation (138).

$$p_T^* = \frac{(S_R - u_R)\rho_R p_{T_L} - (S_L - u_L)\rho_L p_{T_R} + \rho_L\rho_R(S_R - u_R)(S_L - u_L)(u_R - u_L)}{(S_R - u_R)\rho_R - (S_L - u_L)\rho_L} \tag{138}$$

The intermediate wave speeds are defined in equation (139) and equation (140) [36].

$$S_L^* = S_M - \frac{\mid B_x \mid}{\sqrt{\rho_L^*}} \tag{139}$$

$$S_R^* = S_M + \frac{\mid B_x \mid}{\sqrt{\rho_R^*}} \tag{140}$$

The outer wave speeds are defined in equation (141) and equation (143) [36].

$$S_L = min(u_L, u_R) - max(c_{fL}, c_{fR}) \tag{141}$$

$$S_R = max(u_L, u_R) + max(c_{fL}, c_{fR}) \tag{142}$$

By applying the jump conditions across each of the wave boundaries for each intermediate state, we can solve for each of the conserved variables along with the velocities and pressure at each intermediate state. Therefore, the HLLD flux is then given in equation (143) [36].

$$\overrightarrow{F}_{HLLD} = \begin{pmatrix} \overrightarrow{F}_L & S_L > 0 \\ \overrightarrow{F}^*_L & S_L \leq 0 \leq S^*_L \\ \overrightarrow{F}^{**}_L & S^*_L \leq 0 \leq S_M \\ \overrightarrow{F}^{**}_R & S_M \leq 0 \leq S^*_R \\ \overrightarrow{F}^*_R & S^*_R \leq 0 \leq S_R \\ \overrightarrow{F}_R & S_R < 0 \end{pmatrix} \tag{143}$$

At each cell interface, the magnitudes and directions of the eigenvalues are calculated using the method described above. From these calculations the flux is then calculated from equation (143). This is then used as the spatial variation of the MHD equations at the specified cell interface. The unity of all the cell interface solutions is then used as the complete spatial variation of the MHD equations at the given time step.

3.3.3 Resistive MHD

The Godunov method and HLLD flux solver both assumed that the MHD equations were in the ideal from (no resistivity); but in order to capture the effects felt by the plasma in an MPD thruster, it is necessary to include the influence of resistivity on the solutions. Since the time step and spatial variation methods were both second order accurate, the method for calculating the resistive flux should also be second order accurate [37]. A method for accomplishing this is now described.

3.3.3.1 Spatial Discretization of the Current for a Uniform Grid

Since the flux for the magnetic field contains the Hall term and $\vec{J} = c\nabla \times \vec{B}$, it is necessary to calculate the current with second order accuracy at the cell interfaces. For a Cartesian grid, this can be accomplished by a simple central difference and averaging method [38].

For the x-face, the currents are given in equation (144), equation (145), and equation (146).

$$J^x_{i+1/2,j,k} = c[\frac{B^z_{i,j+1,k} + B^z_{i+1,j+1,k} - B^z_{i,j-1,k} - B^z_{i+1,j-1,k}}{4dy} - \frac{B^y_{i,j,k+1} + B^z_{i+1,j,k+1} - B^z_{i,j,k-1} - B^z_{i+1,j,k-1}}{4dz}] \tag{144}$$

$$J^y_{i+1/2,j,k} = c[\frac{B^x_{i,j,k+1} + B^x_{i+1,j,k+1} - B^x_{i,j,k-1} - B^x_{i+1,j,k-1}}{4dz} - \frac{B^z_{i+1,j,k} - B^z_{i,j,k}}{dx}] \tag{145}$$

$$J^z_{i+1/2,j,k} = c[\frac{B^y_{i+1,j,k} - B^y_{i,j,k}}{dx} - \frac{B^x_{i,j+1,k} + B^x_{i+1,j+1,k} - B^x_{i,j-1,k} - B^x_{i+1,j-1,k}}{4dy}] \tag{146}$$

For the y-face, the currents are given in equation (147), equation (148), and equation (149).

$$J^x_{i,j+1/2,k} = c[\frac{B^z_{i,j+1,k} - B^z_{i,j,k}}{dy} - \frac{B^y_{i,j,k+1} + B^z_{i,j+1,k+1} - B^z_{i,j,k-1} - B^z_{i,j+1,k-1}}{4dz}] \tag{147}$$

$$J^y_{i,j+1/2,k} = c[\frac{B^x_{i,j,k+1} + B^x_{i,j+1,k+1} - B^x_{i,j,k-1} - B^x_{i,j+1,k-1}}{4dz} - \frac{B^z_{i+1,j,k} + B^z_{i+1,j+1,k} - B^z_{i-1,j,k} - B^z_{i-1,j+1,k}}{4dx}] \tag{148}$$

$$J^z_{i,j+1/2,k} = c[\frac{B^y_{i+1,j,k} + B^y_{i+1,j+1,k} - B^y_{i-1,j,k} - B^y_{i-1,j+1,k}}{4dx} - \frac{B^x_{i,j+1,k} - B^x_{i,j,k}}{dy}] \quad (149)$$

For the z-face, the currents are given in equation (150), equation (151), and equation (152).

$$J^x_{i,j,k+1/2} = c[\frac{B^z_{i,j+1,k} + B^z_{i,j+1,k+1} - B^z_{i,j-1,k} - B^z_{i,j-1,k+1}}{4dy} - \frac{B^y_{i,j,k+1} - B^z_{i,j,k}}{dz}] \quad (150)$$

$$J^y_{i,j,k+1/2} = c[\frac{B^x_{i,j,k+1} - B^x_{i,j,k}}{dz} - \frac{B^z_{i+1,j,k} + B^z_{i+1,j,k+1} - B^z_{i-1,j,k} - B^z_{i-1,j,k+1}}{4dx}] \quad (151)$$

$$J^z_{i,j,k+1/2} = c[\frac{B^y_{i+1,j,k} + B^y_{i+1,j,k+1} - B^y_{i-1,j,k} - B^y_{i-1,j,k+1}}{4dx} - \frac{B^x_{i,j+1,k} + B^x_{i,j+1,k+1} - B^x_{i,j-1,k} - B^x_{i,j-1,k+1}}{4dy}] \quad (152)$$

Since this thesis deals with 1D models of MPD thrusters with the axis of the MPD on the z-axis ($\nabla = \frac{\partial}{\partial z}$), the currents can be reduced to only the z-face currents given by equation (153), equation (154), and equation (154).

$$J^x_{i,j,k+1/2} = -c[\frac{B^y_{i,j,k+1} - B^y_{i,j,k}}{dz}] \quad (153)$$

$$J^y_{i,j,k+1/2} = c[\frac{B^x_{i,j,k+1} - B^x_{i,j,k}}{dz}] \quad (154)$$

$$J^z_{i,j,k+1/2} = 0 \quad (155)$$

These currents are then used in the calulation of the resistive flux as described in the following section.

3.3.3.2 Resistive Flux for a Uniform Grid

Resistivity enters into the MHD equations in the energy density equation and in Alfven's equation. The fluxes for these equations must be corrected to handle resistivity. The resistive flux terms are given by equation (156), equation (157), equation (158), and equation (159).

$$F_e^{res} = \frac{c}{2}\eta J^x_{i,j,k+1/2}(B^y_{i,j,k+1} + B^y_{i,j,k}) - \frac{c}{2}\eta J^y_{i,j,k+1/2}(B^x_{i,j,k+1} + B^x_{i,j,k}) \tag{156}$$

$$F_{bx}^{res} = -c\eta J^y_{i,j,k+1/2} \tag{157}$$

$$F_{by}^{res} = c\eta J^x_{i,j,k+1/2} \tag{158}$$

$$F_{bz}^{res} = 0 \tag{159}$$

After the ideal MHD equations are spatially solved using the Godunov method, these resistive fluxes are then added to the calculated ideal fluxes. This maintains the second order accuracy of the scheme of the flux solver. More accurate methods are employed in other studies, but these methods are beyond the scope of this thesis.

3.4 Open-MHD

The code base for this thesis was taken from the open source MHD simulation code Open-MHD, written by Dr. S. Zenintani. The code was originally written in FORTRAN but for the purposes of this thesis and computational ease it was coded into Matlab. The Matlab script was extensively tested and was successful in reproducing the results from [39] and [40]. For the studies of the MPD thrusters, the number of grid points was set to $500 + 2$. This number corresponds to a similar accuracy as in the examples. The initial solution domain was split into two regions. The region of z less than zero was set as the region with no magnetic fields and the initial injected plasma. The region of z greater than zero was modelled as the MPD thruster with an approximated vacuum density and vacuum pressure. This region is described in detail in Chapter 4. The length of the MPD thruster was chosen as $15.6cm$ as in [6]. The Open-MHD code base uses the Godunov method and HLLD flux solver to solve for the spatial variation of the MHD equations. The time step method is the TVD second order Runge-Kutta method as described above. The slope limiter is chosen as the minmod limiter as well.

IV. Results and Analysis

4.1 Steady State Simulations

In order to get a basic idea of the expected behavior of the MPD thruster the steady state solution outlined in Chapter 2 will be investigated. For these simulations the initial plasma pressure will be fixed at $10^4 Pa$. This was done in an attempt to boost the acceleration of the plasma through the MPD channel. Initially, the plasma number density is fixed at $1 \times 10^{20} m^{-3}$. These studies will test four main areas that effect the plasma acceleration: initial velocity, applied current, initial plasma pressure, and plasma number density. The application of an applied solenoidal magnetic field in the z-direction will not be tested in this steady state model for reasons outlined in Chapter 2. Application of a solenoidal magnetic field will be tested in the time dependent studies.

4.1.1 Current and Velocity Tests

For the first series of studies, the MPD thrusters will be analyzed in the steady state limit as described in Chapter 2 and Chapter 3. This is done so as to investigate the behavior of the MPD thrusters in the regime long after any time dependent effects are present and can effect the thrust.

For the first test the initial velocity of the plasma is set to $1000 m/s$ and there is an applied current of $1000 A$.

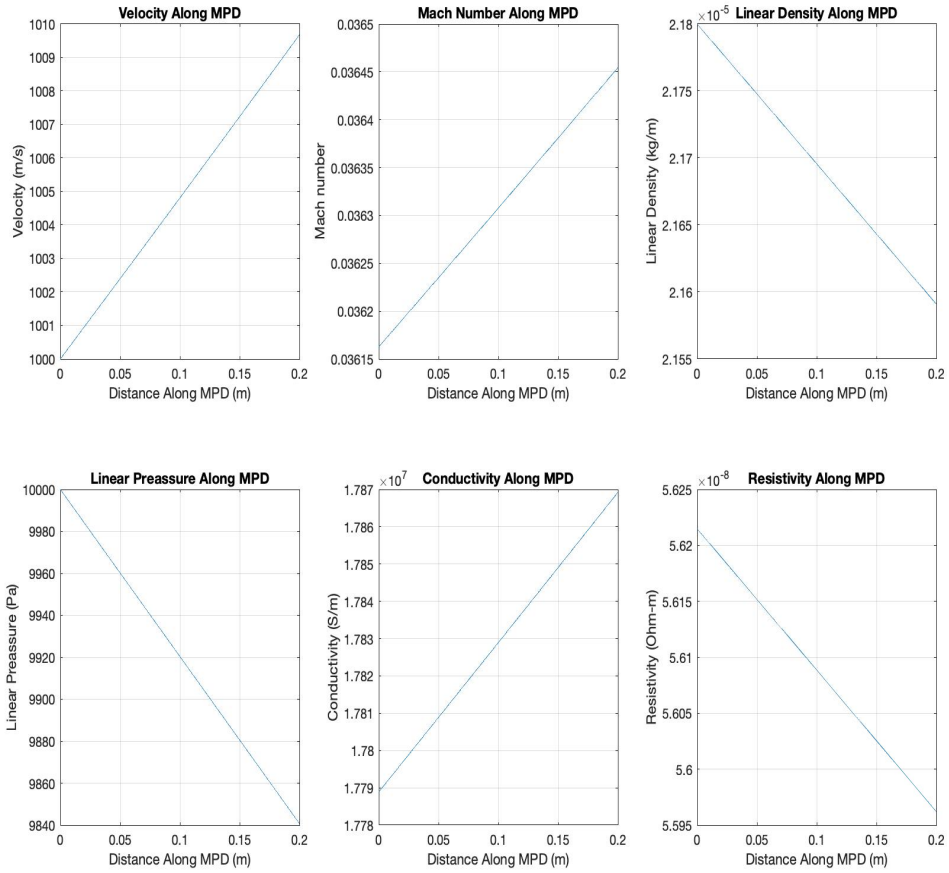

Figure 15: Steady state MPD thruster with $J = 1000A$ and $u_0 = 1000m/s$.

Figure 15 shows the behavior of the low power MPD thruster. This figure shows that in the steady state limit the acceleration achieved by the plasma is minimal, only achieving a $10m/s$ velocity boost. This is much too small to be of use for a plasma accelerator; however, Figure 15 also shows that the density of plasma decays by a very small amount, showing that there is little change in the shape of the plasma plume. The remainder of the studies with different applied current and initial velocities are given in Appendix A, Section A.1.1.

It is clear from these observations, including those in the appendix, that in the

steady state limit, a high current and high initial velocity is required for any meaningful acceleration to occur. This is important for the operation of a long duration MPD thruster such as those used in deep space missions. For heavy ion drivers, the steady state regime is clearly to be avoided; but, we can still extract some trends from the steady state models that can be useful for heavy ion driver operation.

4.1.1.1 Summary of the Current and Velocity Tests

Figure 16 shows the summary of the results for the steady state applied current and velocity tests.

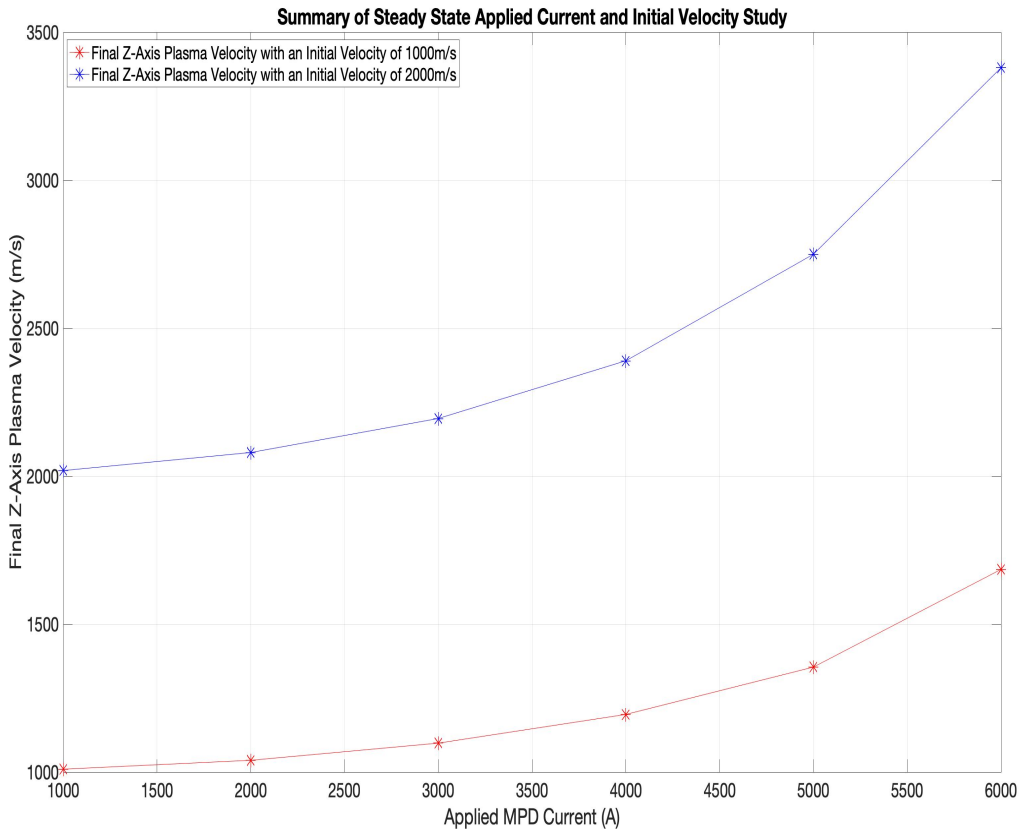

Figure 16: Summary of the results for the steady state applied current and velocity tests.

From Figure 16 it is clear that current has a positive effect on the plasma acceleration in the steady state limit. The higher the applied current, the greater the final velocity, as discussed earlier. Figure 16 also shows that an initial velocity of $1000m/s$ only results in a minimal plasma acceleration in the steady state limit, whereas an initial velocity of $2000m/s$ results in a sizeable acceleration. Figure 16 also demonstrates that in the steady state limit, the plasma does not receive a significant acceleration until a current of at least $3000A$ is applied to the MPD. From this it is deduced that an MPD operating in the steady state limit must have a large applied current in order to operate as an effective thruster or plasma accelerator. Therefore, a steady state MPD thruster is a poor choice for a heavy ion plasma driver.

4.1.2 Pressure Tests

In this study, the effect of increasing the initial pressure of the plasma will be examined. Specifically, the pressure will be raised to the value of $10^5 Pa$. It is of interest for PJMIF heavy ion drivers to keep the applied power of the MPD as low as possible, thereby limiting the amount of energy required to accelerate the plasma, leading us to examine low power MPD thrusters.

The first test will be of the $1000A$ MPD thruster with an initial velocity of $1000m/s$.

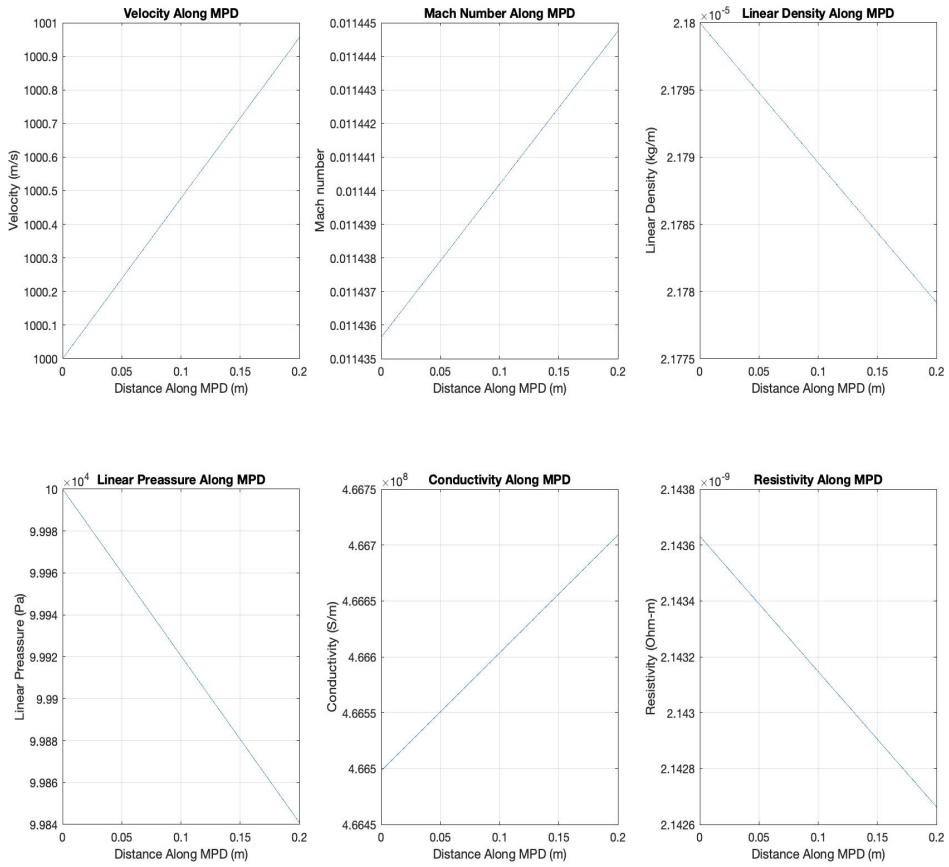

Figure 17: Steady state MPD thruster with $J = 1000A$, $u_0 = 1000m/s$, and $p_0 = 10^5 Pa$.

Figure 17 shows that the higher pressure decreases the acceleration significantly. Specifically, the plasma velocity is only increased by $1m/s$. This amount of acceleration is incredibly poor and of no use to a heavy ion driver. It is also worth noting that the plasma expands away from the z-axis at rate similar to that of the previous $1000A$ cases. With a higher initial pressure, the assumption is the plasma would expand at a higher rate; though, it is possible that this current is too low to test this assumption. Additional results are shown in Appendix A, Section A.1.2.

4.1.2.1 Summary of the Pressure Tests

Figure 18 shows the summary of the results for the steady state initial plasma pressure tests.

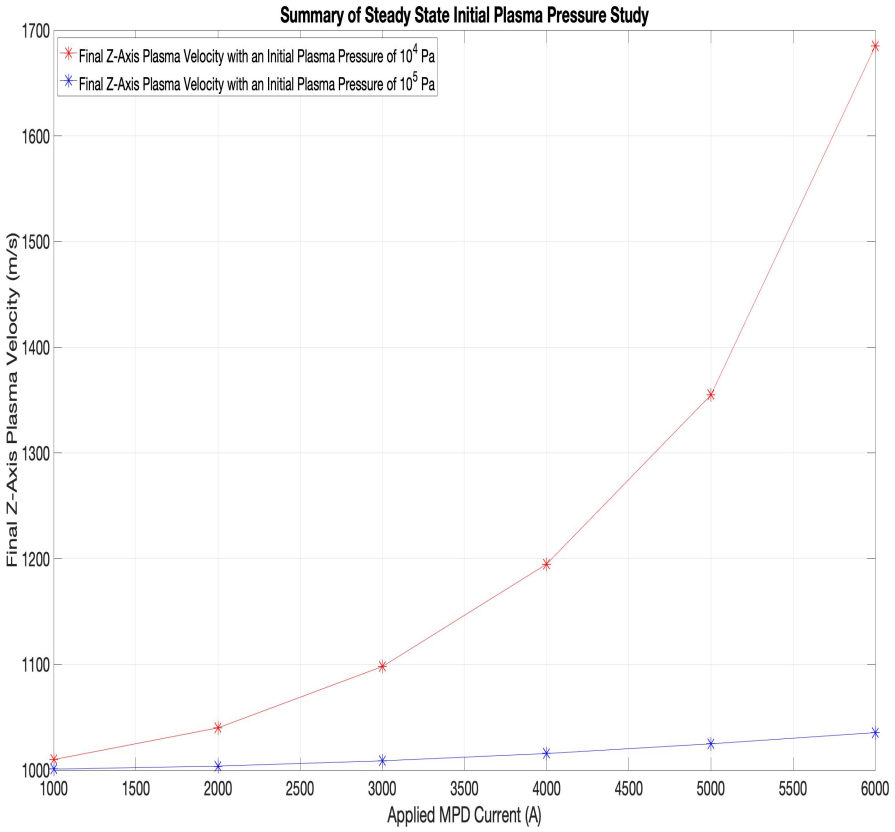

Figure 18: Summary of the results for the steady state initial plasma pressure tests.

Figure 18 demonstrates that at a pressure greater than $10^4 Pa$, specifically $10^5 Pa$, the plasma acceleration is minimal. The initial pressure of $10^5 Pa$ results in a velocity gain of only $35.5 m/s$, where the pressure of $10^4 Pa$ results in a velocity gain of $685 m/s$. This demonstrates that in the steady state limit, pressures above $10^4 Pa$ show minimal acceleration and a steady state MPD thruster operates more effectively when the plasma is kept at a lower pressure.

4.1.3 Number Density Tests

The last set of tests performed with the steady state model are those of the number densities. The number density of the plasma has been kept at the value of $10^{20}m^{-3}$ in the simulations previously discussed; values above this will be tested here. This increase in density is required since the plasma for heavy ion drivers must be very dense, as shown in Table 1.

First, a density of $10^{21}m^{-3}$ will be tested. In the first test, the MPD will be given an applied current of $2000A$ and an initial plasma velocity of $2000m/s$.

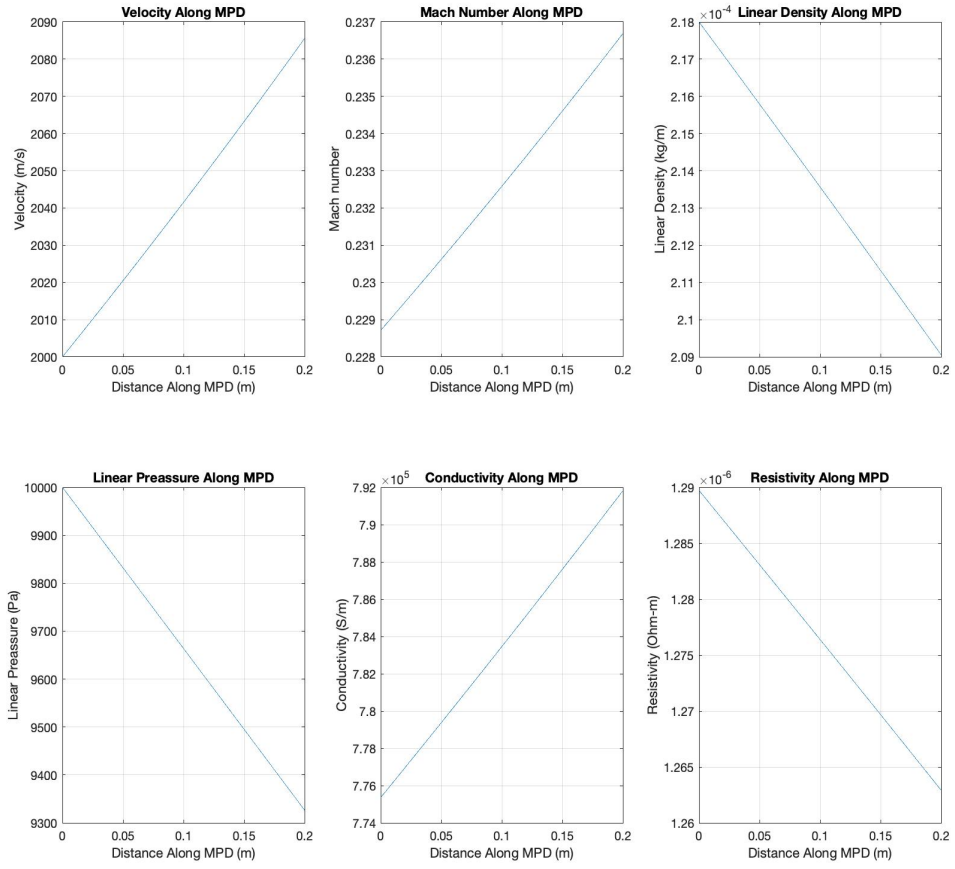

Figure 19: Steady state MPD thruster with $J = 2000A$, $u_0 = 2000m/s$, and $n = 10^{21}m^{-3}$.

From Figure 19 it is seen that the plasma experiences a small acceleration, where the plasma velocity is increased by $86m/s$. This acceleration is again much too small for any meaningful use. The plasma is once again shown to expand away from the z-axis at rate similar to that of the previous cases. It is worth noting that the resistivity is increased by an order of magnitude from the previous cases as well. This is expected, as the greater the number density, the greater the number of self interactions within the plasma. Additional results are shown in Appendix A, Section A.1.3.

4.1.3.1 Summary of the Number Density Tests

Figure 20 shows the summary of the results for the steady state plasma number density tests.

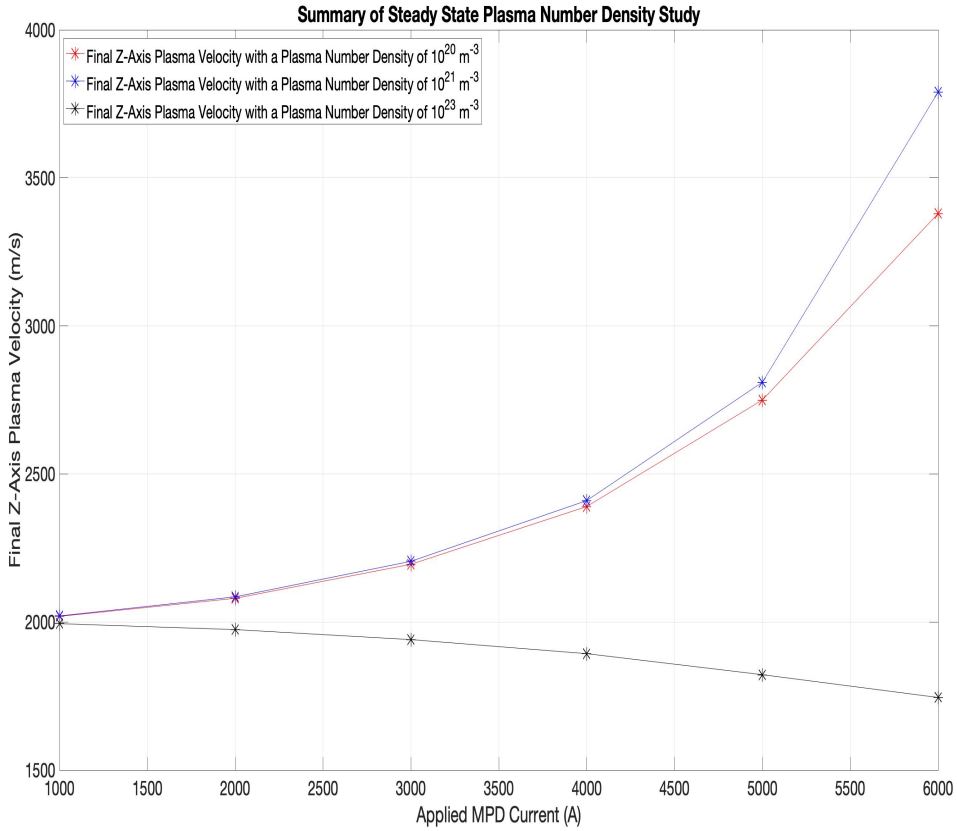

Figure 20: Summary of the results for the steady state plasma number density tests.

Figure 20 shows that a steady state MPD thruster can operate effectively with plasma propellant composed of number densities of $10^{20}m^{-3}$ and $10^{21}m^{-3}$. However, when a plasma propellant consisting of a number density of $10^{23}m^{-3}$, the plasma is decelerated in the MPD channel. The initial velocity of the plasma was $2000m/s$ in these studies, so the plasma is injected with enough initial momentum to exit the thruster; but, this does demonstrate that the plasma can become trapped in the MPD channel if it does not have a significant amount of momentum when initially injected. This is investigated in the time dependent studies.

4.1.4 Limitations of Steady State Simulations

The full theory behind the 1D steady state model of the MPD thruster is provided in Chapter 2. The first limitation of this model is that it is 1D. There are many interactions along the x and y directions which are ignored in this model. Specifically, this model considers a 1D flow of plasma, requiring that the plasma can only flow in the z direction. In order to capture the x and y motion of the plasma, a full 3D steady state model is required which is significantly more complicated and should be the subject of future work. Secondly, this model is in the steady state regime; therefore, many time-dependent interactions that are assumed to have been removed from the plasma over time. This also means that the steady state regime does not model the effects that would be seen in a heavy ion plasma driver, since plasma drivers are pulsed systems that operate on a very short time scale. It does, however, provide some guidance on what tests to conduct in the time dependent model.

4.2 Time Dependent Simulations

As stated in Chapter 2, the majority of MPD simulations occur at a fixed initial temperature that is either at or below the temperature of ionization. This usually corresponds to a temperature of around $1eV$. For these simulations however, it is the initial plasma pressure that will be fixed; specifically at $10^4 Pa$. This was done in an attempt to boost the acceleration of the plasma through the MPD channel. The initial velocity is also fixed at $100m/s$. Initially the number density of the plasma is set to $2 \times 10^{20} m^{-3}$, although varying this will be the subject of a later study. The plasma is assumed to be a xenon plasma, with an atomic mass of $2.18 \times 10^{-25} kg$. The pressure of the MPD chamber is initially kept at $1Pa$. This was chosen since it is the lowest pressure the numerical method could handle.

Before reviewing the results of these studies, a brief note on the organization of the

figures is necessary. Each figure presents six snapshots of the plasma motion through the MPD chamber at a given time. The simulation was run on a time domain from $0s$ to $3.6 \times 10^{-7}s$. The upper left figure is the given plasma parameter at the initial time of $t = 0s$, the upper middle figure is the given plasma parameter at a time of $t = 1.2 \times 10^{-7}s$, the upper right figure is the given plasma parameter at a time of $t = 1.8 \times 10^{-7}s$, the bottom left figure is the given plasma parameter at a time of $t = 2.4 \times 10^{-7}s$, the middle left figure is the given plasma parameter at a time of $t = 3.0 \times 10^{-7}s$, and the bottom left figure is the given plasma parameter at a time of $t = 3.6 \times 10^{-7}s$. The significant results of these studies are summarized in the summary sections after each of the studies.

4.2.1 Vacuum Density Studies

As stated in Chapter 3, these studies were carried out using a Godunov based MHD solver. One of the most significant limitations of this method is that it cannot properly model a true vacuum. There must be a density of plasma present everywhere within the simulation domain. This is significant because laboratory vacuum systems produce vacuum densities within the vacuum chamber several orders of magnitude lower than this simulation can handle. Also, laboratory MPD vacuum chambers do not contain a density of plasma within the MPD chamber before the plasma is injected. As a result, it is necessary to analyze the effect that this vacuum plasma density has on the simulations. The results of this study are presented here.

The first density examined is a vacuum density set to 10^{-3} times that of the initial plasma density.

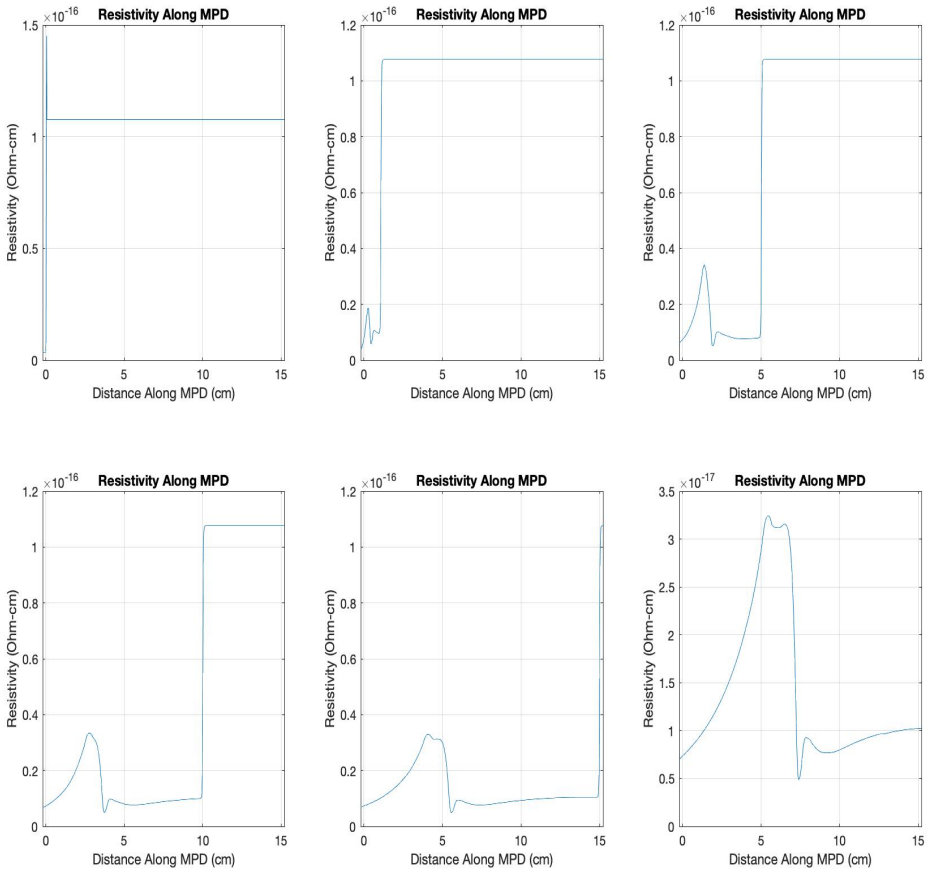

Figure 21: Evolution of the plasma resistivity along the MPD for a vacuum density 10^{-3} that of the plasma density. The upper left figure is at the initial time of $t = 0s$, the upper middle figure is at a time of $t = 1.2 \times 10^{-7}s$, the upper right figure is at a time of $t = 1.8 \times 10^{-7}s$, the bottom left figure is at a time of $t = 2.4 \times 10^{-7}s$, the middle left figure is at a time of $t = 3.0 \times 10^{-7}s$, and the bottom left figure is at a time of $t = 3.6 \times 10^{-7}s$.

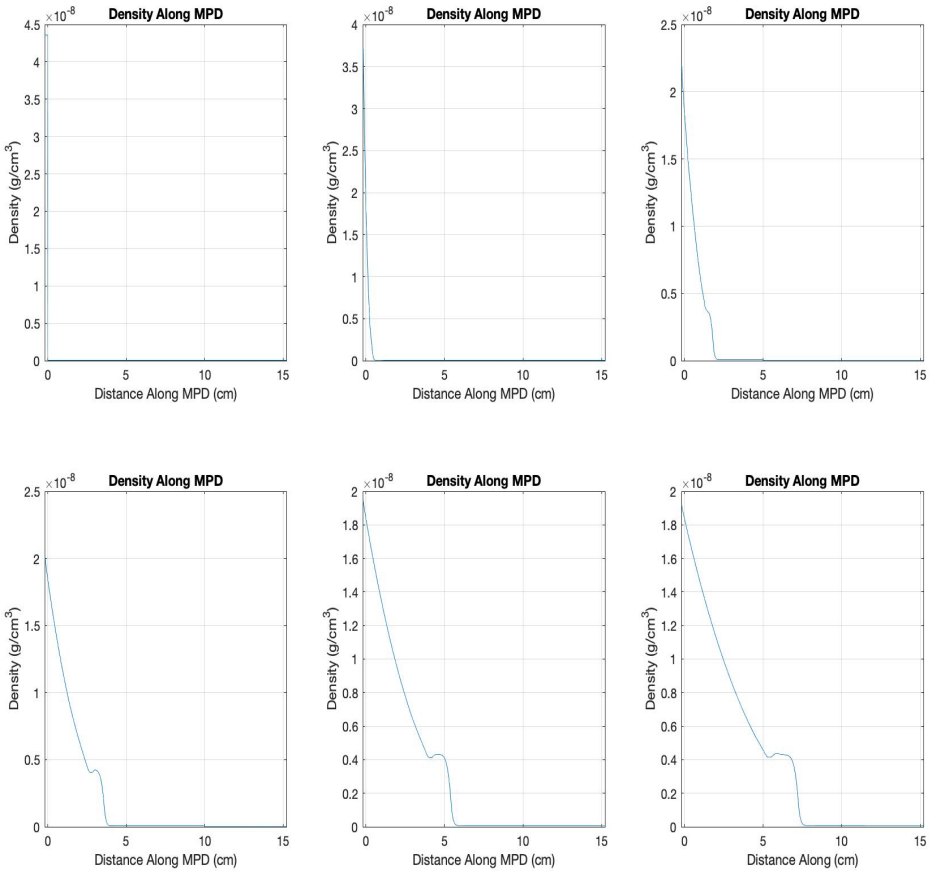

Figure 22: Evolution of the plasma density along the MPD for a vacuum density 10^{-3} that of the plasma density. The upper left figure is at the initial time of $t = 0s$, the upper middle figure is at a time of $t = 1.2 \times 10^{-7}s$, the upper right figure is at a time of $t = 1.8 \times 10^{-7}s$, the bottom left figure is at a time of $t = 2.4 \times 10^{-7}s$, the middle left figure is at a time of $t = 3.0 \times 10^{-7}s$, and the bottom left figure is at a time of $t = 3.6 \times 10^{-7}s$.

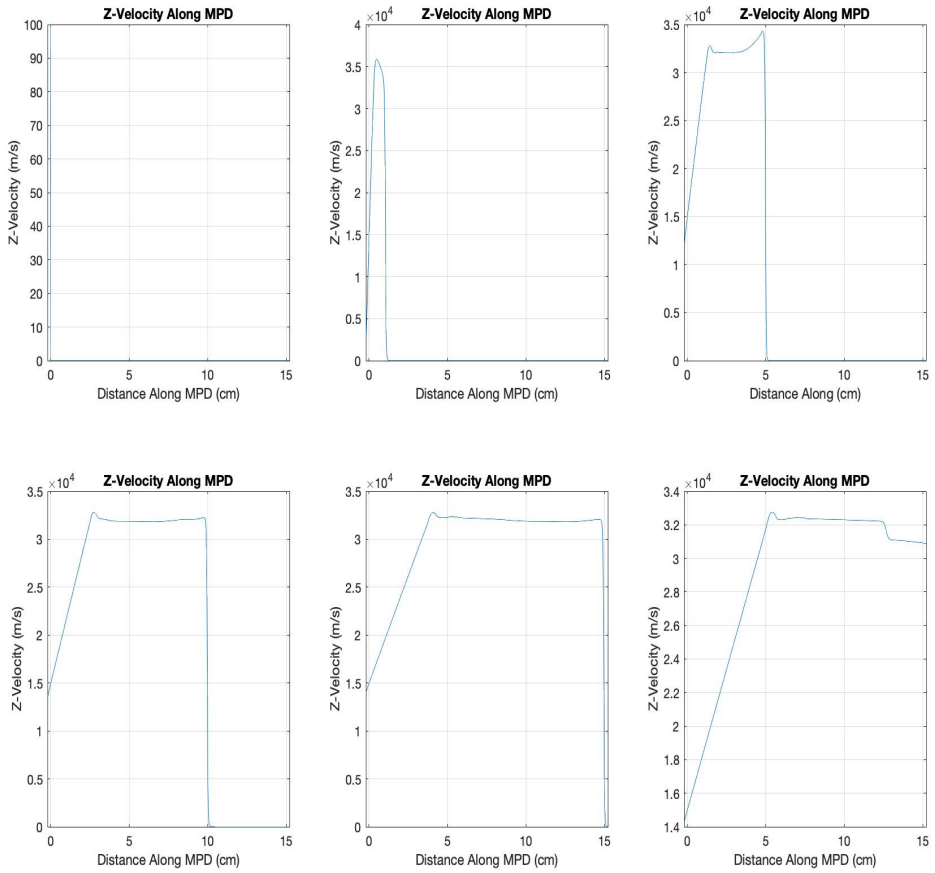

Figure 23: Evolution of the axial velocity for a vacuum density 10^{-3} that of the plasma density. The upper left figure is at the initial time of $t = 0s$, the upper middle figure is at a time of $t = 1.2 \times 10^{-7}s$, the upper right figure is at a time of $t = 1.8 \times 10^{-7}s$, the bottom left figure is at a time of $t = 2.4 \times 10^{-7}s$, the middle left figure is at a time of $t = 3.0 \times 10^{-7}s$, and the bottom left figure is at a time of $t = 3.6 \times 10^{-7}s$.

In Figure 21 the resistivity along the z-axis of the MPD is shown. Since the vacuum density is a noticeable fraction of the plasma density, there is a significant effect on the acceleration and flow of the plasma through the MPD channel. This is reflected in Figure 22, where a slow decay of the plasma is observed along the z-axis in the channel at the inlet region causing the plasma to accelerate more slowly.

Figure 23 shows the z velocity of the plasma column along the MPD channel. The instabilities in the z velocity show that the vacuum plasma density has a significant effect on the plasma injected into the MPD chamber. These instabilities are observed as the small oscillations in the z velocity along the thruster channel, as well as the shear drop in the z velocity in the last figure. The remainder of the studies can be found in Appendix A, Section A.2.1.

From these data sets, as well as those found in the appendix, it is observed that once the vacuum density reaches the level of 10^{-5} and/or 10^{-6} of the initial plasma density, the effect that the vacuum plasma density has on the motion of the injected plasma is minimal. The injected plasma experiences a very low amount of resistivity beyond the inlet region due to the rapid expansion of the plasma density away from the z axis of the MPD thruster. The oscillations in the z velocity along the MPD channel are seen to rapidly dissipate when the vacuum density is decreased to the level of 10^{-5} and/or 10^{-6} of the initial plasma density. Thus, affirming that at these vacuum plasma densities, the motion of the injected plasma is relatively unaffected by the vacuum plasma density. Therefore, in this thesis the vacuum shall be approximated as a plasma of a density 10^{-5} of the initial density of the injected plasma.

The trade off for a higher acceleration is faster expansion away from the the z-axis. For the beam to be effective in a PJMIF experiment, the beam must be tightly compressed. Future work into the simulation of MPD thrusters should focus on maximizing the acceleration while simultaneously minimizing the expansion of the plasma beam within the MPD channel and within the plume of plasma produced outside the MPD thruster. This work should be conducted with higher order codes such as particle in cell (PIC) or full kinetic theory methods in order to fully capture the particle motion within the thruster and plume.

4.2.2 Summary of the Vacuum Density Studies

Figure 24 shows the summary of the results for the vacuum plasma density resistivity study. In the figure, the x-axis is labeled as the vacuum density multiplication factor. This corresponds to the factor multiplied to the injected plasma density (10^{-3}, 10^{-4}, 10^{-5}, and 10^{-6}).

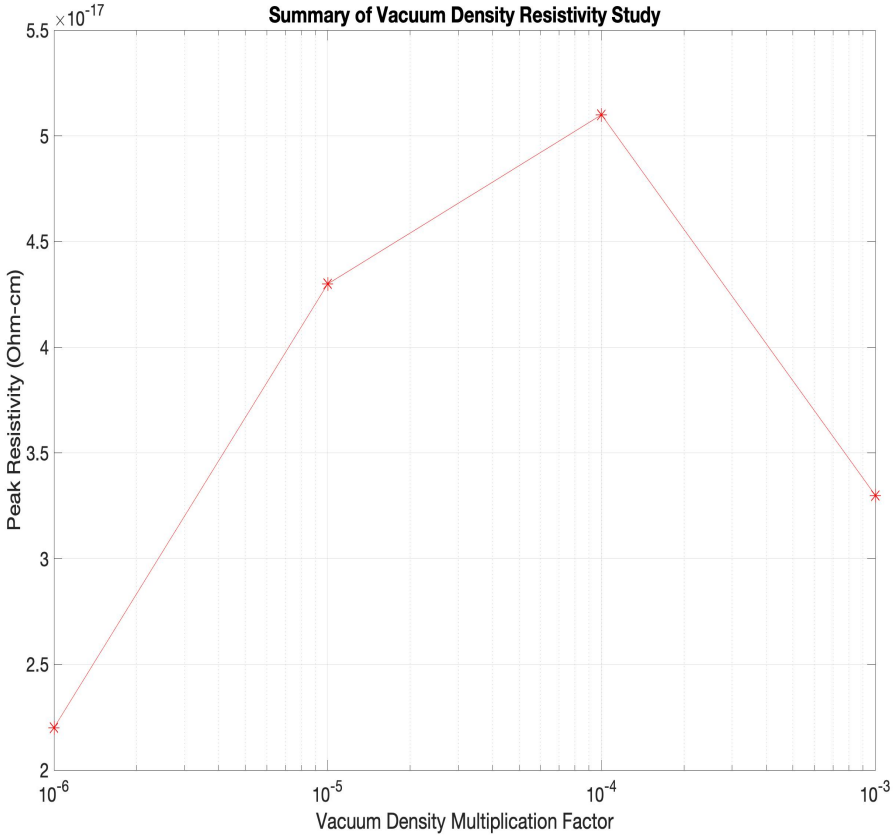

Figure 24: Summary of the Results for the Vacuum Plasma Density Resistivity Study

Figure 24 shows that the general trend of the reduced vacuum density is to reduce the plasma resistivity within the MPD chamber. It is worth noting that the plasma vacuum density of 10^{-3} times that of the injected plasma has a low final resistivty within the chamber in these studies. However, Figure 21 shows that the initial plasma

resitivity caused by this vacuum density is an order of magnitude greater than the other vacuum density resistivity studies, only decaying to this low value near the final simulation time. Although, all the vacuum density values show final values of the resistivity on the order of $10^{-17}\Omega - cm$, only the vacuum density of 10^{-3} times that of the injected plasma density reaches values on the order of $10^{-16}\Omega - cm$.

Figure 25 shows the summary of the results for the study of the plasma density expansion for varying vacuum plasma densities. The y-axis of this figure is labeled as the plasma density decay distance. This corresponds to the distance within the MPD chamber at which the plasma density reaches a minimized value. This can be identified from the plasma density figures as the point where the plasma density first reaches a value near zero on the plots.

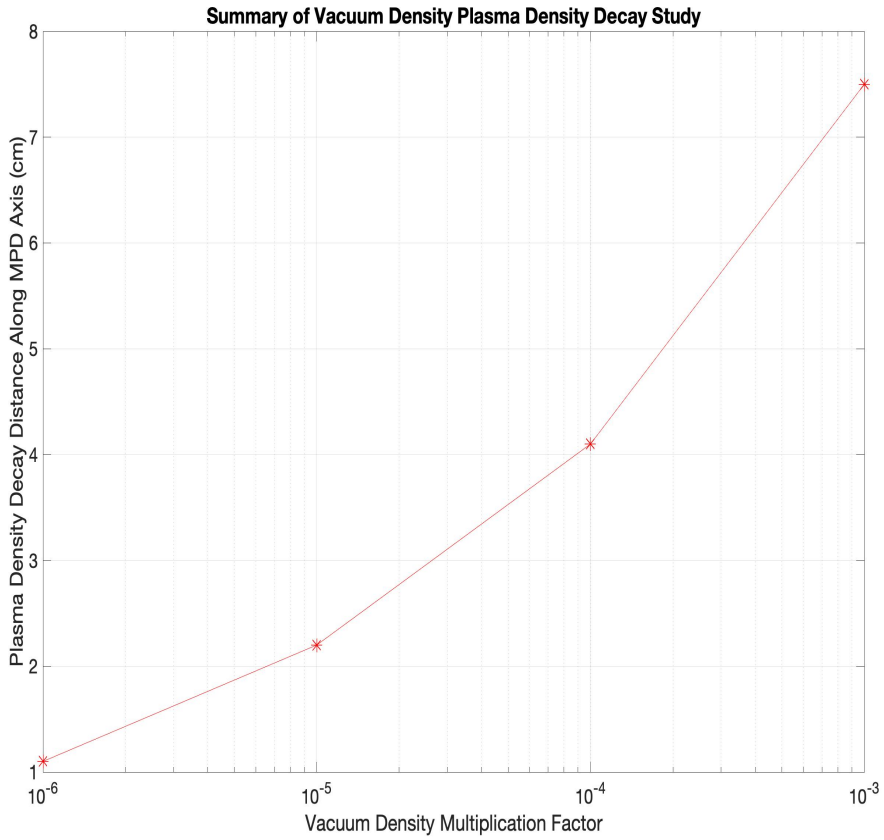

Figure 25: Summary of the results for the study of the plasma density expansion for the vacuum plasma densities.

Figure 25 shows that the result of the decrease in vacuum plasma density is the increase in the expansion of the plasma away from the z-axis. The lower the vacuum plasma density, the shorter the plasma density decay distance. Therefore, the trade off for the decrease in vacuum plasma density is the increase in plasma expansion. Since the plasma beams for heavy ion drivers must remain compact in order to effectively function as a spherical liner for target implosion, the results of this study show that the plasma accelerated within an MPD thruster may expand too rapidly within the chamber to be used in a heavy ion driver. 2D studies are required to make a final decision from these results as the effect of the reflective MPD thruster walls is not

included in 1D studies and this may play a major role in curbing the plasma expansion rate.

Figure 26 shows the summary of the results for the study of the final z-axis plasma velocity for varying vacuum plasma densities.

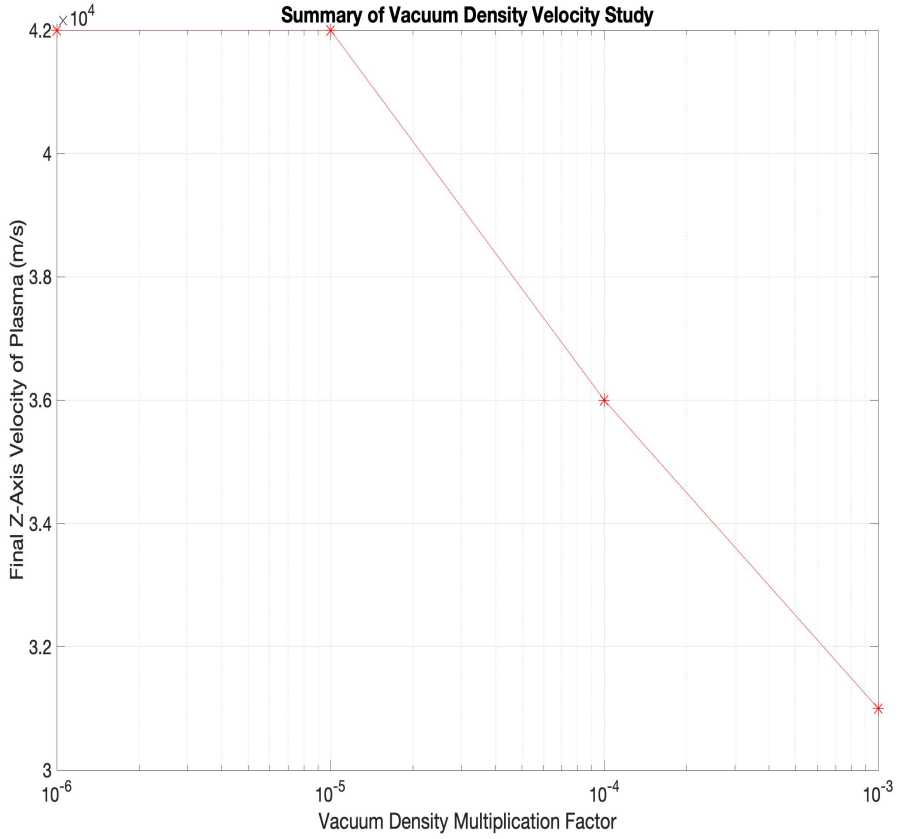

Figure 26: Summary of the results for the study of the plasma density expansion for the vacuum plasma densities.

Figure 26 shows that the decrease in vacuum plasma density results in the increase of the z-axis velocity attained by the plasma. Figure 25 also demonstrates that once the vacuum plasma density reaches a multiplication factor of 10^{-5} or 10^{-6}, the z-axis plasma velocity plateaus at a value of $4.2 \times 10^4 m/s$. Therefore a vacuum plasma density of 10^{-5} or 10^{-6} times that of the injected plasma density provides

a good simulation of the vacuum for this solver. However, when tested at applied currents of $3000A$ and $4000A$, the vacuum density of 10^{-6} times that of the injected plasma density induced numerical instabilities in the calculated plasma energy density. Therefore a vacuum plasma density of 10^{-5} times that of the injected plasma density was chosen for the following studies.

4.2.3 Applied Current Studies

This study will examine the effect of applied MPD currents. As stated in Chapter 2, the magnetic field of an MPD thruster is given by equation (5) for $r > r_c$. The expected result is that a higher applied current will results in higher acceleration. This has been both predicted and observed in previous studies, where the plasma has been initially kept at relatively low pressures. In this study however, the plasma is initially kept at a high pressure and this hypothesis will be tested.

Four currents will be tested: $1000A$, $2000A$, $3000A$, and $4000A$. These currents were chosen from the MPDs tested in [6]. The goal of a heavy ion plasma accelerator is to achieve the maximum velocity with the smallest amount of applied power as possible. Therefore, it is of interest to test MPD thrusters with as little applied current as possible. There will be no applied solenoidal magnetic field in the $\hat{z}$ direction. This will be examined in the Section 4.2.4.

For the first test a current of $1000A$ is applied to the MPD thruster with a vacuum density of 10^{-5} of the initial plasma density.

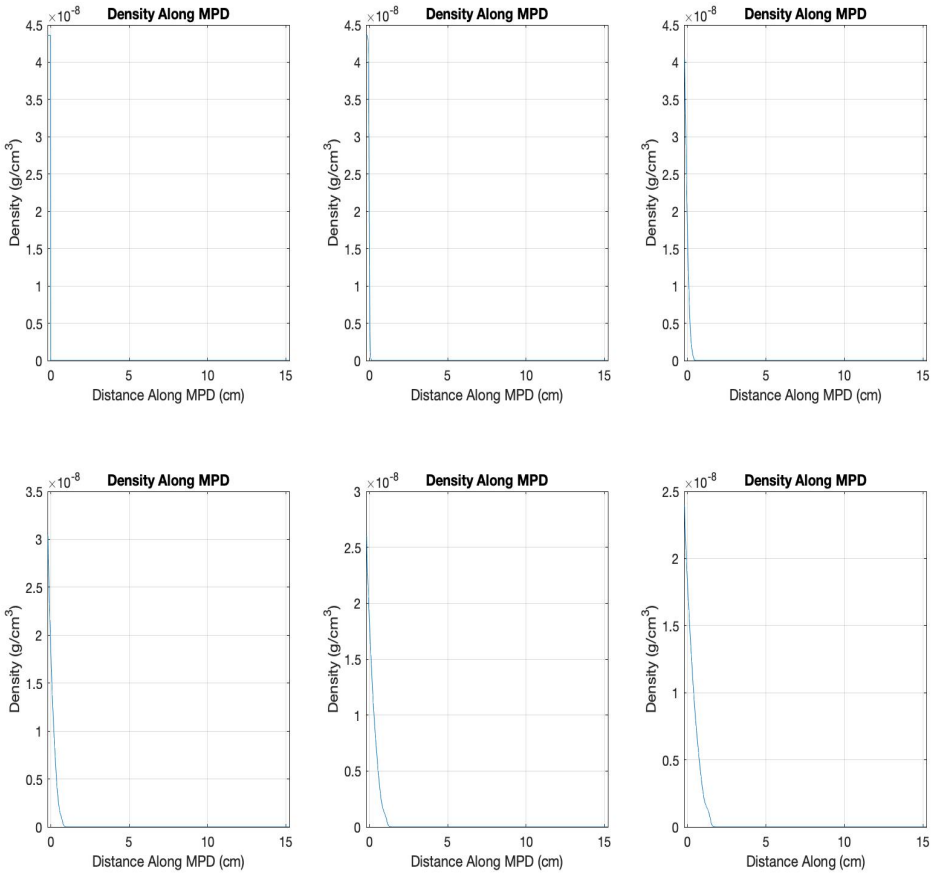

Figure 27: Evolution of the plasma density for J = $1000A$ and vacuum density 10^{-5} that of the plasma density. The upper left figure is at the initial time of $t = 0s$, the upper middle figure is at a time of $t = 1.2 \times 10^{-7}s$, the upper right figure is at a time of $t = 1.8 \times 10^{-7}s$, the bottom left figure is at a time of $t = 2.4 \times 10^{-7}s$, the middle left figure is at a time of $t = 3.0 \times 10^{-7}s$, and the bottom left figure is at a time of $t = 3.6 \times 10^{-7}s$.

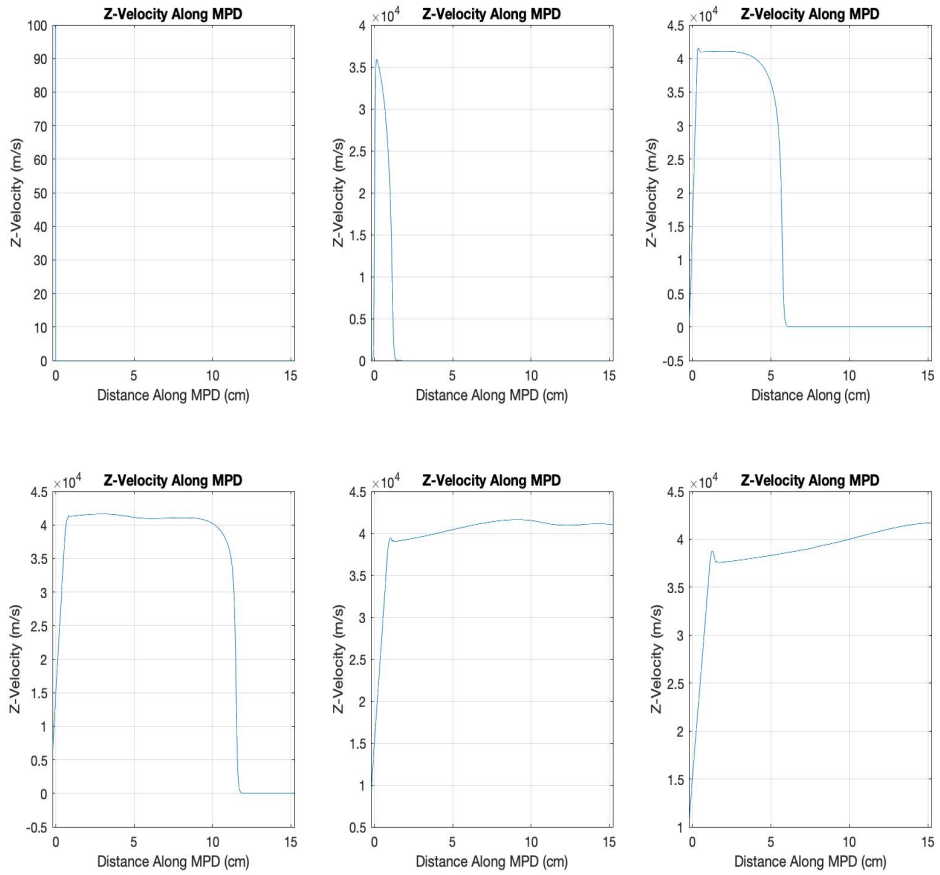

Figure 28: Evolution of the axial velocity for J = $1000A$ and vacuum density 10^{-5} that of the plasma density. The upper left figure is at the initial time of $t = 0s$, the upper middle figure is at a time of $t = 1.2 \times 10^{-7}s$, the upper right figure is at a time of $t = 1.8 \times 10^{-7}s$, the bottom left figure is at a time of $t = 2.4 \times 10^{-7}s$, the middle left figure is at a time of $t = 3.0 \times 10^{-7}s$, and the bottom left figure is at a time of $t = 3.6 \times 10^{-7}s$.

Figure 27 shows that the plasma expands rapidly away from the z-axis, as expected. Figure 28 shows that a final velocity of $4.2 * 10^4 m/s$ is achieved at the end of the MPD channel. This is an incredible acceleration of the plasma. From previous references, speeds on the order of $1 - 4km/s$ are predicted where here the velocity

reached is predicted to be $42km/s$. This increase in velocity is substantial, yet may be due in large part to hydrodynamic expansion and acceleration. The plasma that has just been injected into the MPD thruster experiences a force applied to it by the plasma being injected into the thruster behind it, like a piston driving the gas ahead of it. Since the gas being injected is kept at a pressure much greater than that of the vacuum pressure, the pressure gradient produces a high initial acceleration in the gas causing the piston affect to greatly increase the plasma acceleration within the MPD channel. Additional results are shown in Appendix A, Section A.2.2.

4.2.3.1 Summary of Applied Current Studies

Figure 29 shows the effect of the applied MPD current on the expansion of the plasma density.

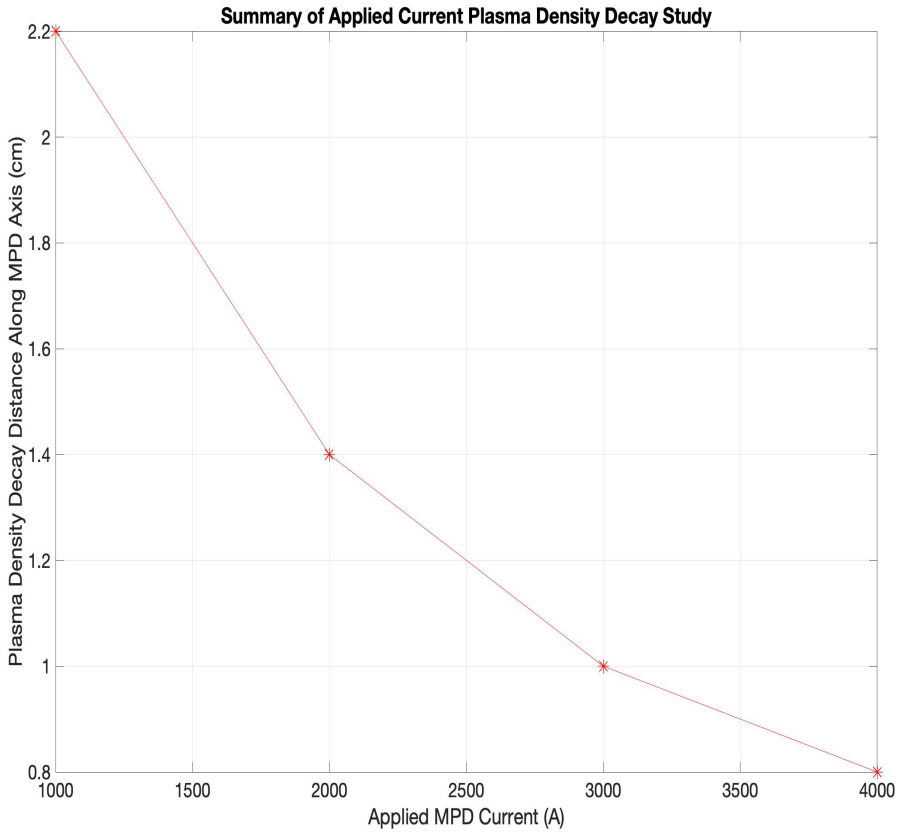

Figure 29: Summary of the effect of the applied MPD current on the expansion of the plasma density.

Figure 29 shows that the greater the current applied to the MPD thruster, the shorter the plasma density decay distance. Therefore, low-power MPD thrusters are more desirable for heavy ion drivers since the plasma density expands away from the z-axis over a greater distance within the MPD thruster. However, the plasma decay distances shown in Figure 29 are on the order of a few cm. This is not ideal since applying currents on the order of $1000A$ to a circuit only a few cm in distance can cause short circuit discharges that can ruin the acceleration effects; especially when the circuit is composed primarily of a fast moving ionized plasma, as is the case inside an MPD thruster. 2D studies are again required to make a final decision regarding

these results, as the effect of the reflective MPD thruster walls is not included in 1D studies.

Figure 30 shows the effect of the applied MPD current on the z-axis velocity of the plasma at the thruster outlet.

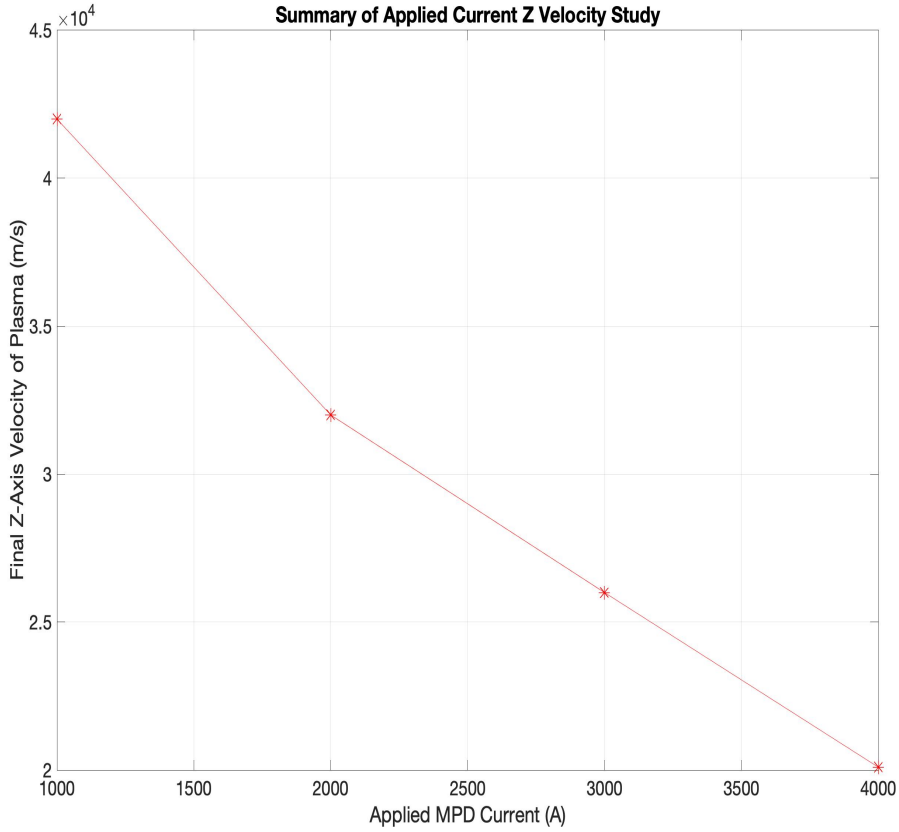

Figure 30: Summary of the effect of the applied MPD current on the axial velocity of the plasma at the thruster outlet.

Figure 30 shows the interesting result that the higher the applied MPD current, the lower the z-axis plasma velocity, at the thruster outlet. Since the plasma is initially maintained at a high pressure, the primary mechanism of the plasma's initial acceleration is not electromagnetic, but actually hydrodynamic. The initial expansion of the plasma into the vacuum chamber acts like a piston to the plasma injected in

front, driving the plasma forward though hydrodynamic expansion and acceleration. After the inlet region, however, the electromagnetic force exerted on the plasma becomes dominant; and, as was seen in the steady state analysis, the higher applied currents then accelerate the plasma out of the thruster before the plasma column can feel the full effects of the force from the hydrodynamic expansion. Therefore, for a high initial plasma pressure, low-power MPD thrusters appear to be more desirable. 2D studies are again required to make a final decision from these results, as the effect of the reflective MPD thruster walls are not included in 1D studies and these walls will most certainly effect the force from hydrodynamic expansion and acceleration. This observation could also be the result of numerical instabilities resulting from the limitations of the Godunov and HLLD solver.

4.2.4 Applied Magnetic Field Studies

As stated in Chapter 2, the effect of a constant solenoidal magnetic field in the $\hat{z}$ direction causes a swirling motion in the plasma. As a brief review, the solenoidal magnetic field causes a force in the $\hat{\theta}$ direction given by equation (13). If the plasma is assumed to rotate as a rigid body, this causes a rotation defined by the angular velocity in equation (16). From this expression, it is clear that a higher applied magnetic field (B_z) results in a larger angular velocity of the plasma and, therefore, a larger rotational effect. A lower mass flow rate increases the angular velocity. This effect is worth noting since this angular motion can be converted to axial motion by diverging magnetic fields, such as those in a magnetic nozzle. The study of magnetic nozzles is the subject of future work, but it is clear that swirling motion caused by the application of solenoidal magnetic fields is of paramount importance to heavy ion drivers and general plasma accelerators. For this study, four magnitudes of magnetic fields are studied: $10mT$, $20mT$, $30mT$, and $40mT$.

For the first test, a magnetic field of $10mT$ is applied to the MPD thruster.

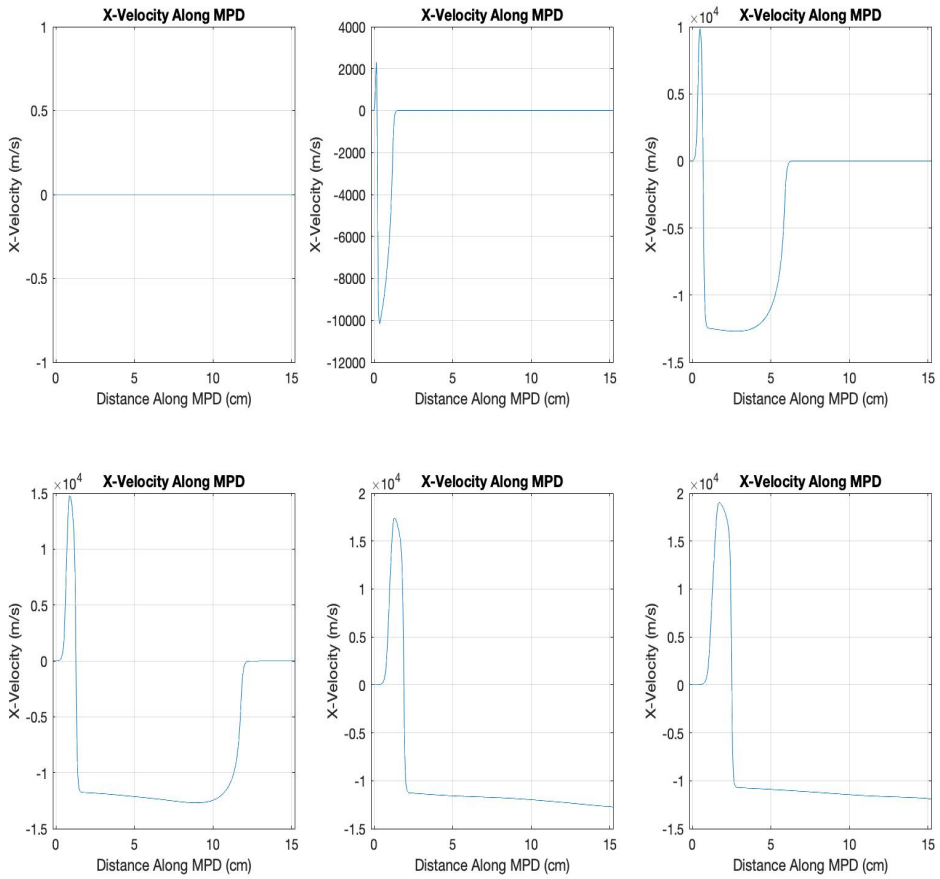

Figure 31: Evolution of the X velocity for J = $1000A$, $B_{app} = 10mT$, and vacuum density 10^{-5} that of the plasma density. The upper left figure is at the initial time of $t = 0s$, the upper middle figure is at a time of $t = 1.2 \times 10^{-7}s$, the upper right figure is at a time of $t = 1.8 \times 10^{-7}s$, the bottom left figure is at a time of $t = 2.4 \times 10^{-7}s$, the middle left figure is at a time of $t = 3.0 \times 10^{-7}s$, and the bottom left figure is at a time of $t = 3.6 \times 10^{-7}s$.

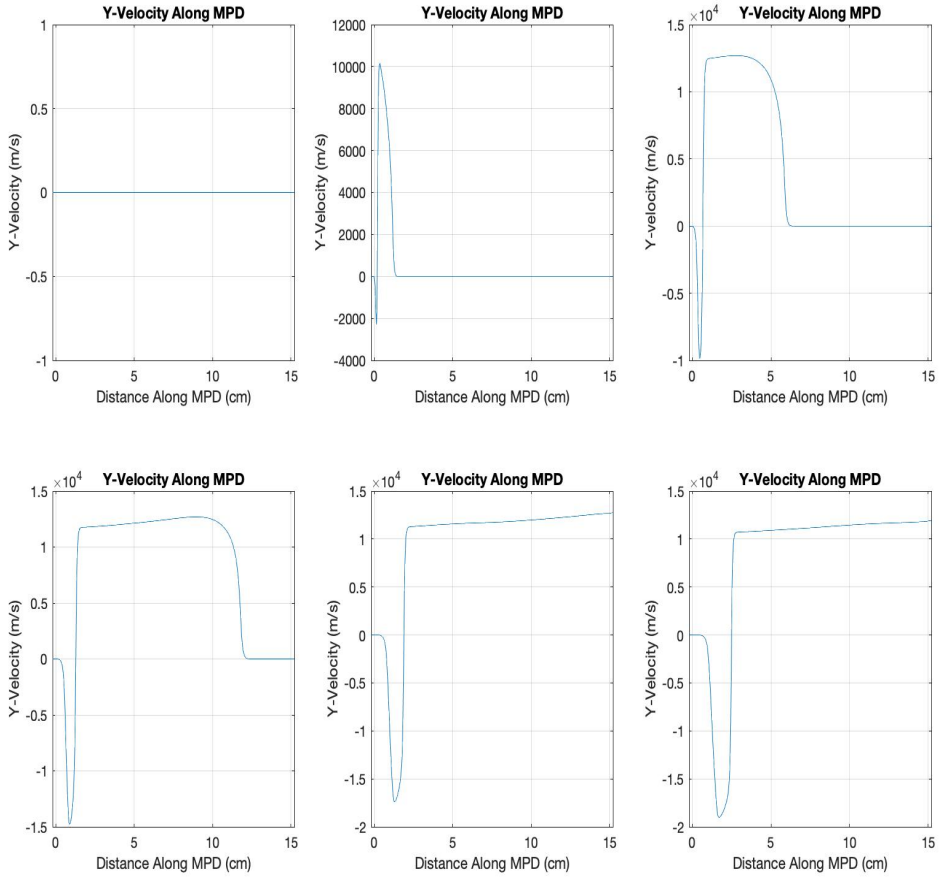

Figure 32: Evolution of the Y velocity for J = $1000A$, $B_{app} = 10mT$, and vacuum density 10^{-5} that of the plasma density. The upper left figure is at the initial time of $t = 0s$, the upper middle figure is at a time of $t = 1.2 \times 10^{-7}s$, the upper right figure is at a time of $t = 1.8 \times 10^{-7}s$, the bottom left figure is at a time of $t = 2.4 \times 10^{-7}s$, the middle left figure is at a time of $t = 3.0 \times 10^{-7}s$, and the bottom left figure is at a time of $t = 3.6 \times 10^{-7}s$.

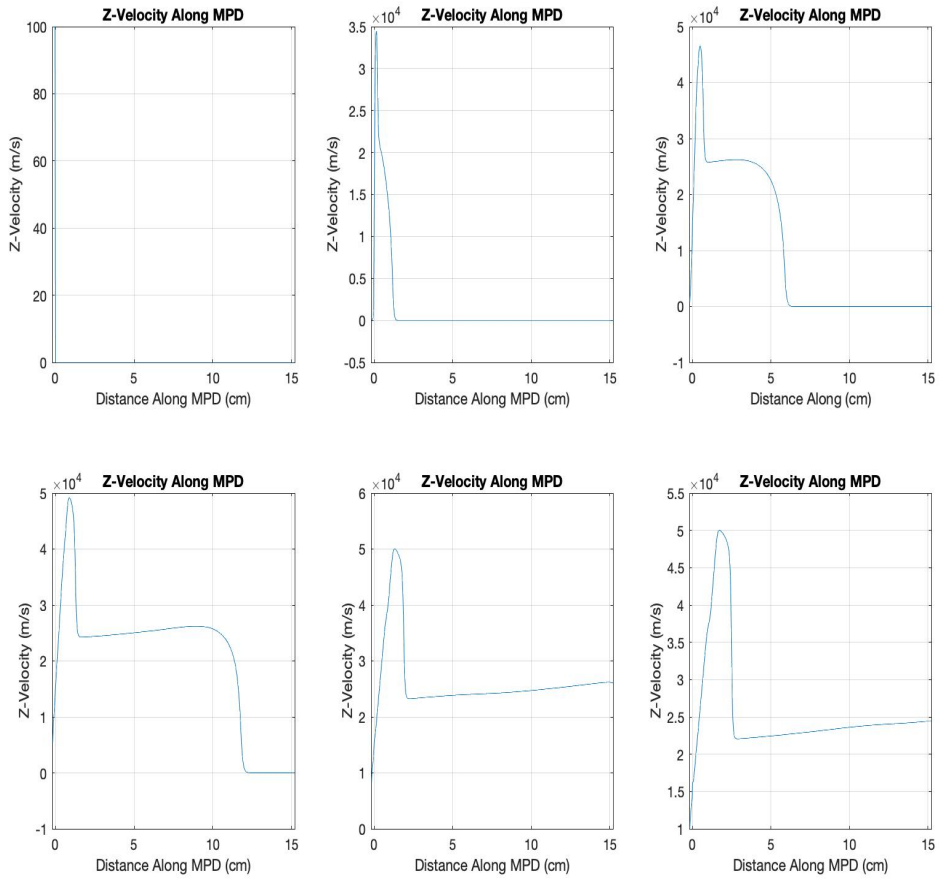

Figure 33: Evolution of the Z velocity for J = $1000A$, $B_{app} = 10mT$, and vacuum density 10^{-5} that of the plasma density. The upper left figure is at the initial time of $t = 0s$, the upper middle figure is at a time of $t = 1.2 \times 10^{-7}s$, the upper right figure is at a time of $t = 1.8 \times 10^{-7}s$, the bottom left figure is at a time of $t = 2.4 \times 10^{-7}s$, the middle left figure is at a time of $t = 3.0 \times 10^{-7}s$, and the bottom left figure is at a time of $t = 3.6 \times 10^{-7}s$.

Figures 31 and 32 reveal the X and Y axis velocity evolution of the plasma column along the thruster axis. From these figures the swirling effect is clearly demonstrated. The X and Y velocities mirror each other, indicating the swirling motion of the plasma along the thruster column. The magnitude of the acceleration in the X and Y

directions is very high, reaching nearly $20km/s$ at the final time. Figure 33 shows the Z velocity along the MPD thruster column. There is a decrease in the axial velocity caused by the transfer of energy to the swirling motion. It is important to note that if the applied magnetic field is too strong, too much energy will be taken from the axial motion and the plasma will become trapped in the thruster chamber. However, it is also worth noting that the plasma column gains a sizeable increase in the initial acceleration of the plasma caused by the application of the solenoidal magnetic field. This gives rise to the possibility of using a very short MPD thruster with an applied magnetic field to further increase the axial acceleration. This will be the subject of future work. Additional results are shown in Appendix A, Section A.2.3.

4.2.4.1 Summary of Applied Magnetic Field Studies

Figure 34 shows the summary of the effect of the applied solenoidal magnetic field on the velocity of the plasma at the thruster outlet and the peak plasma velocity within the MPD chamber for an applied MPD current of $1000A$. Figures 35, 36, and 37 show the summary for the same study done with applied MPD currents of $2000A$, $3000A$, and $4000A$, respectively. In the figures, the absolute value of the x-axis and y-axis velocities are plotted. Since the x and y-axis velocities mirror each other due to the swirling motion, they are plotted as one data set refered to as the x/y-axis velocity.

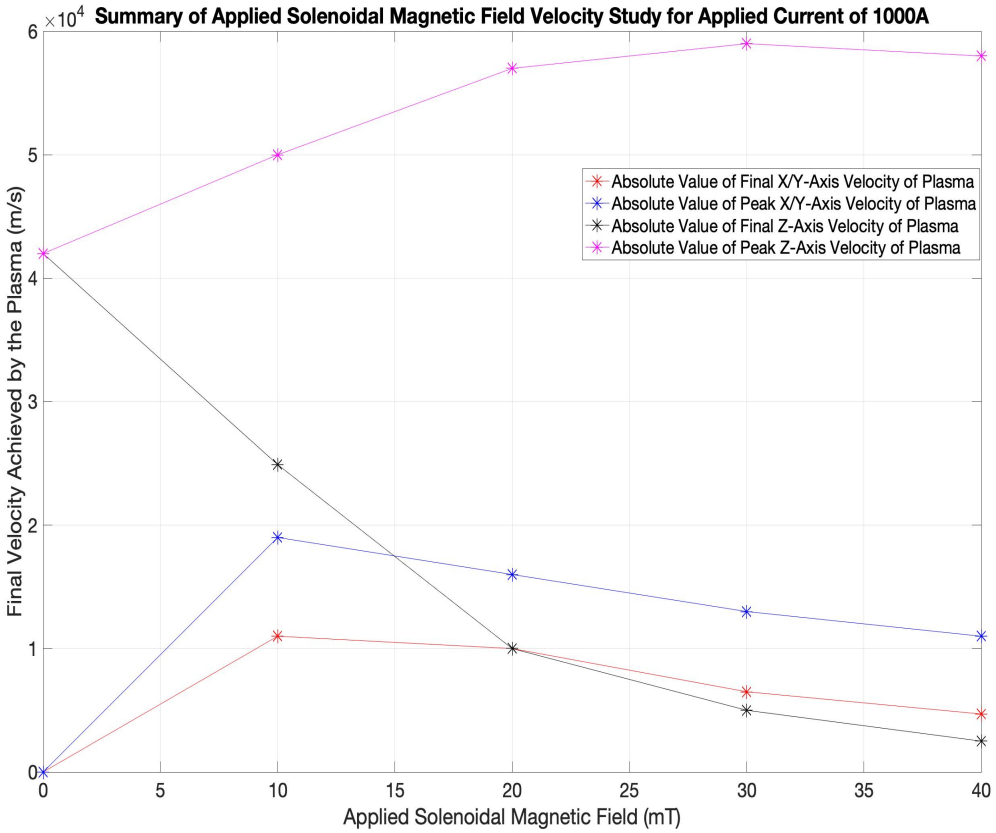

Figure 34: Summary of the effect of the applied solenoidal magnetic field on the velocity of the plasma at the thruster outlet and the peak plasma velocity within the MPD chamber for an applied MPD current of $1000A$.

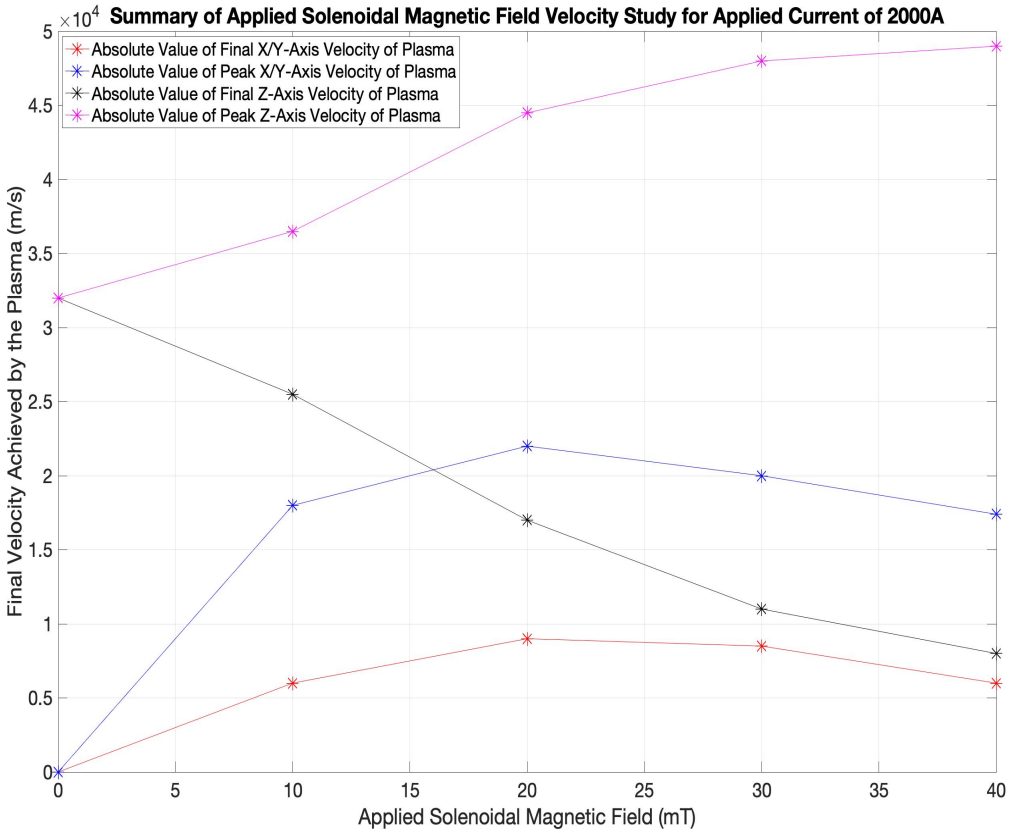

Figure 35: Summary of the effect of the applied solenoidal magnetic field on the velocity of the plasma at the thruster outlet and the peak plasma velocity within the MPD chamber for an applied MPD current of $2000A$.

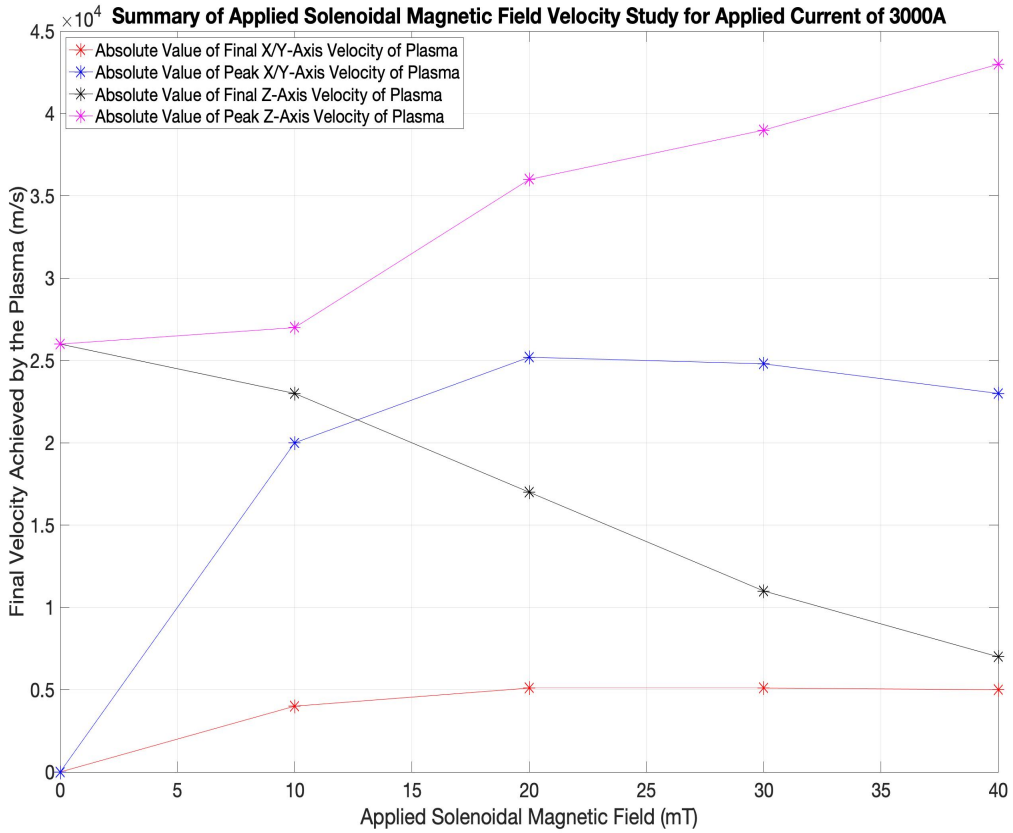

Figure 36: Summary of the effect of the applied solenoidal magnetic field on the velocity of the plasma at the thruster outlet and the peak plasma velocity within the MPD chamber for an applied MPD current of $3000A$.

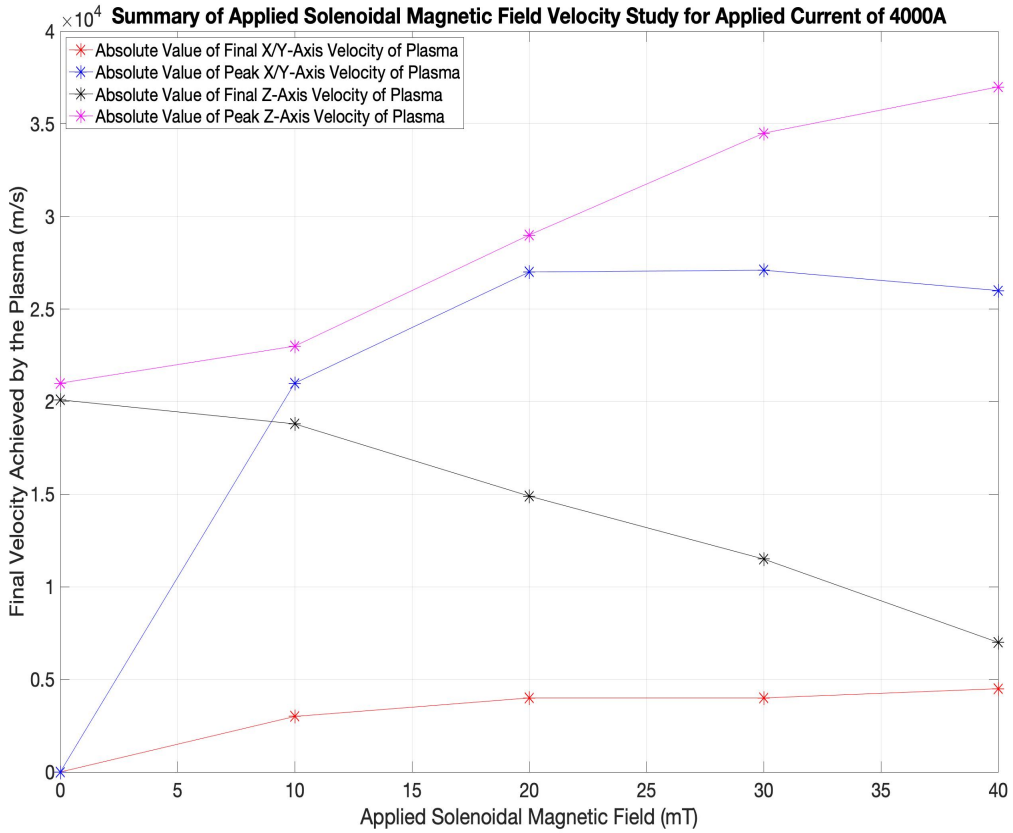

Figure 37: Summary of the effect of the applied solenoidal magnetic field on the velocity of the plasma at the thruster outlet and the peak plasma velocity within the MPD chamber for an applied MPD current of $4000A$.

From these figures several interesting observations can be made. First, the final z-axis plasma velocity decrease is positively correlated with the increase in the final x/y-axis velocity attained by the plasma. This is explained by the fact that in order for the swirling motion to be generated within the plasma, energy from the axial motion of the plasma must be transferred to the azimuthal motion of the plasma. This is seen in the relation between the final z-axis plasma velocity and final x/y-axis velocity attained by the plasma. Second, the peak z-axis velocity attained by the plasma within the MPD thruster increases with applied magnetic field. The peak z-axis velocity is obtained

near the inlet of the MPD thruster, implying that the applied solenoidal magnetic field induces an additional axial force at the thruster inlet. It is worth noting that the peak z-axis velocity obtained by the plasma decreases with increasing current. This can again be explained through the effect of hydrodynamic expansion and acceleration. Third, the peak x/y-axis velocity obtained by the plasma is shown to increase as well. However, it is observed that the x/y-axis peak velocity is maximized by the application of a solenoidal magnetic field in the range of $20mT - 30mT$. This could possibly be due to these magnetic fields being close to a harmonic generated within the swirling motion, therefore increasing the peak x/y-axis velocity. This result requires further testing by higher dimensional codes like PIC or full kinetic theory models in order to capture the full particle motion in the swirling motion. The final result is that the swirling motion is observed in the plasma motion as predicted in Chapter 2; the full effects of which require 2D simulations of magnetic nozzles in order to fully study since in 1D $\frac{\partial B_z}{\partial z} = 0$.

4.2.5 Number Density Studies

Table 1 shows a summary of the number densities required for PJMIF experiments. For the previous tests, the number density of xenon atoms was kept at $2 \times 10^{20} m^{-3}$ which is equal to $2 \times 10^{14} cm^{-3}$. This is one order of magnitude below that achieved by coaxial gun accelerators. This was done because MPD thrusters are normally operated at relatively low number densities. This study will investigate how the MPD thrusters operate with high pressure and higher number densities.

First, let us examine what happens when the number density is increased by one order of magnitude to $2 \times 10^{21} m^{-3}$ ($2 \times 10^{15} cm^{-3}$). We shall examine the effect on the MPD with $1000A$ of applied current and no applied magnetic field.

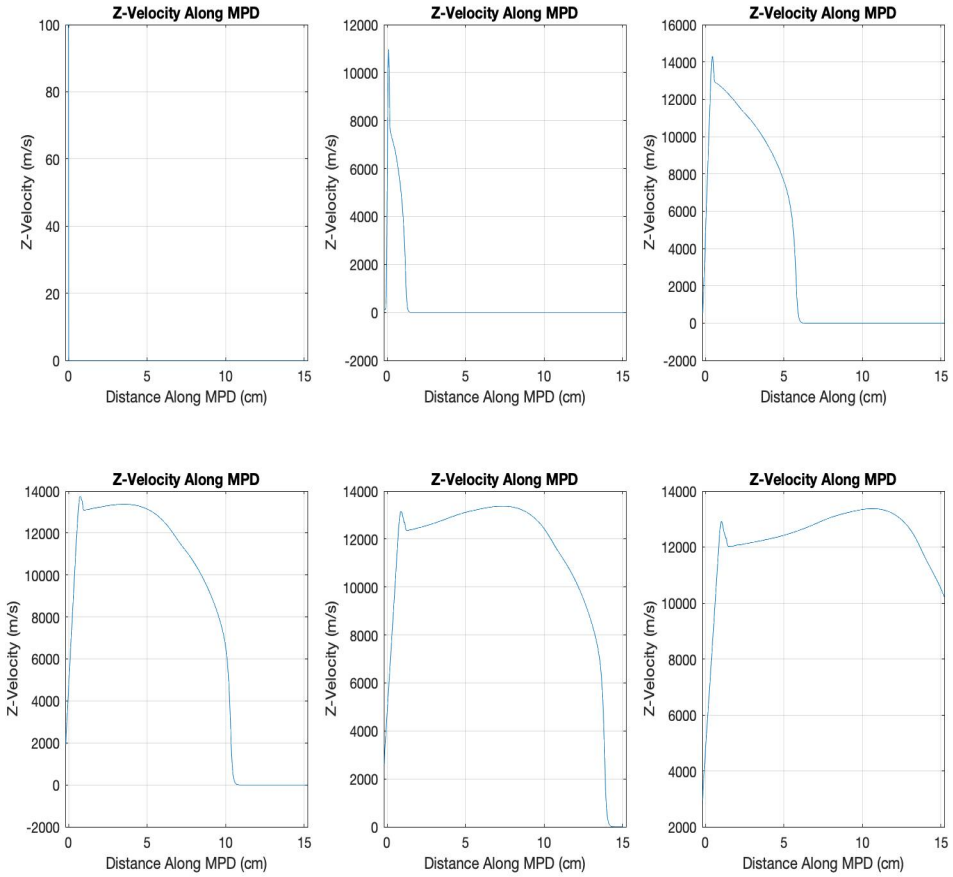

Figure 38: Evolution of the Z velocity for J = $1000A$ with $n = 2 \times 10^{21} m^{-3}$ and vacuum density 10^{-5} that of the plasma density. The upper left figure is at the initial time of $t = 0s$, the upper middle figure is at a time of $t = 1.2 \times 10^{-7}s$, the upper right figure is at a time of $t = 1.8 \times 10^{-7}s$, the bottom left figure is at a time of $t = 2.4 \times 10^{-7}s$, the middle left figure is at a time of $t = 3.0 \times 10^{-7}s$, and the bottom left figure is at a time of $t = 3.6 \times 10^{-7}s$.

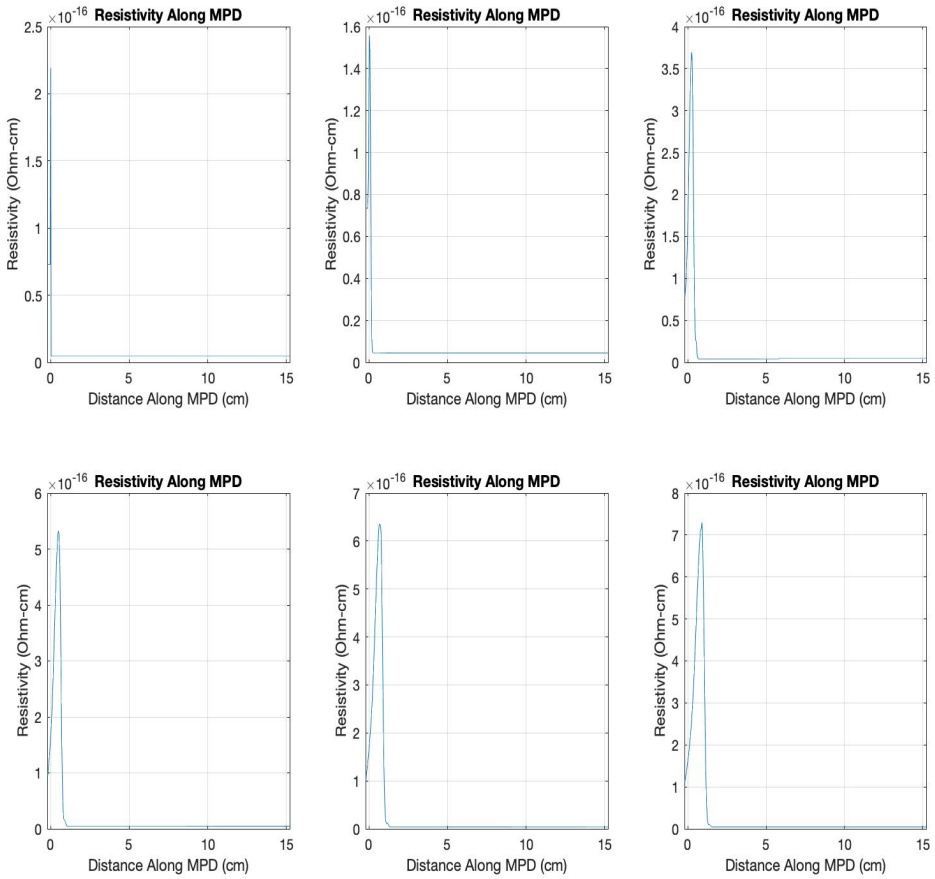

Figure 39: Evolution of the plasma resistivity for J = 1000A with $n = 2 \times 10^{21} m^{-3}$ and vacuum density 10^{-5} that of the plasma density. The upper left figure is at the initial time of $t = 0s$, the upper middle figure is at a time of $t = 1.2 \times 10^{-7}s$, the upper right figure is at a time of $t = 1.8 \times 10^{-7}s$, the bottom left figure is at a time of $t = 2.4 \times 10^{-7}s$, the middle left figure is at a time of $t = 3.0 \times 10^{-7}s$, and the bottom left figure is at a time of $t = 3.6 \times 10^{-7}s$.

Figure 39 shows the resistivity of the plasma column along the MPD axis. In comparison to Figure 56 in Appendix A, Section A.2.4 the resistivity is much higher, a full order of magnitude higher in fact. This is due to the increased number of self interactions within the plasma column from the higher number density. Figure 38

shows the evolution of the Z velocity along the MPD channel. The acceleration is still very high, but decreased significantly from the case with $n = 2 \times 10^{20} m^{-3}$. This is important since it is the goal of a heavy ion driver to accelerate a high density plasma as fast as possible. This alludes to the possibility of a limiting factor to the MPD's ability to accelerate dense plasmas.

From these studies, including those in the appendix, it is clear that for the low current MPD operation, a density of $n = 2 \times 10^{22} m^{-3}$ ($n = 2 \times 10^{16} cm^{-3}$) is too great for any meaningful acceleration to occur and therefore the plasma becomes trapped. The implication being for low current MPD thrusters, a density of $n = 2 \times 10^{22} m^{-3}$ can be considered the maximum critical operating density for high pressure operations. This is important since in Table 1 it was shown that the PLX experiment and fusion reactor design require a plasma number density of at least $10^{17} cm^{-3}$ and $10^{18} cm^{-3}$, much higher than the maximum critical operating density of low powered MPD thrusters. This implies that low power MPD thruster cannot function as a PJMIF heavy ion driver since their maximum critical operating density is far too low. Additional results are shown in Appendix A, Section A.2.4.

4.2.5.1 Summary of Number Density Studies

Figure 40 shows the summary of the effect of the plasma number density on the peak resistivity value for both no applied magnetic field and an applied magnetic field of $20mT$. The peak resistivity values are summarized for each of the applied currents used in this research.

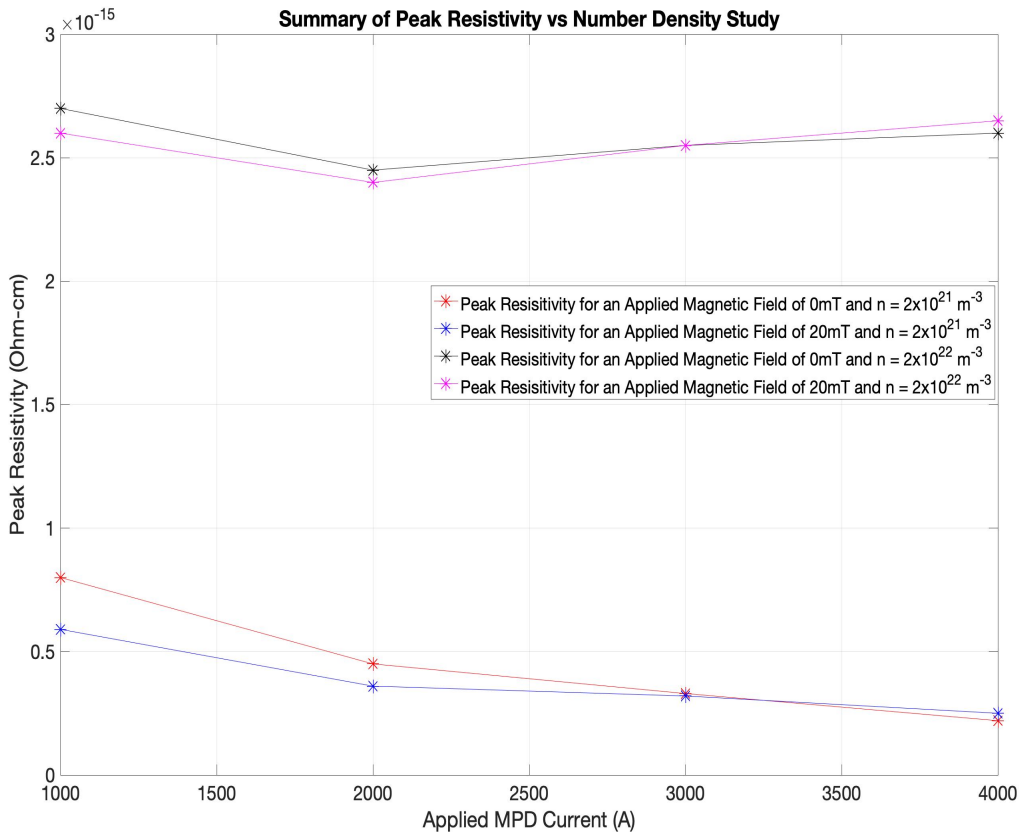

Figure 40: Summary of the effect of the plasma number density on the peak resistivity value for both no applied magnetic field and an applied magnetic field of $20mT$.

Figure 40 shows that the peak resistivity value for the number density of $2 \times 10^{21} m^{-3}$ obtain values on the order of $10^{-16}\Omega - cm$, a full order of magnitude above the peak resistivity values resulting from the plasma number density of $2 \times 10^{20} m^{-3}$. Figure 40 also shows that the peak values of the resistivity for a number density of $2 \times 10^{22} m^{-3}$ obtains values on the order of $10^{-15}\Omega - cm$, two full orders of magnitude above the values found in the studies using a plasma number density of $2 \times 10^{20} m^{-3}$. Therefore, Figure 40 demonstrates the expected result that increasing the number density of the injected plasma increases the peak resistivity felt by the injected plasma. It is worth mentioning that from the studies shown in the above sections,

the peak values of the resitivity are obtained at the thruster inlet before decaying rapidly. Therefore the increase in plasma number density increases the number of self-interactions at the thruster inlet. The effect of this is summarized next.

Figure 41 and Figure 42 shows the summary of the effect of the plasma number density on the final z-axis velocity at the thruster outlet for both no applied magnetic field and an applied magnetic field of $20mT$ at each applied MPD current studied in this thesis.

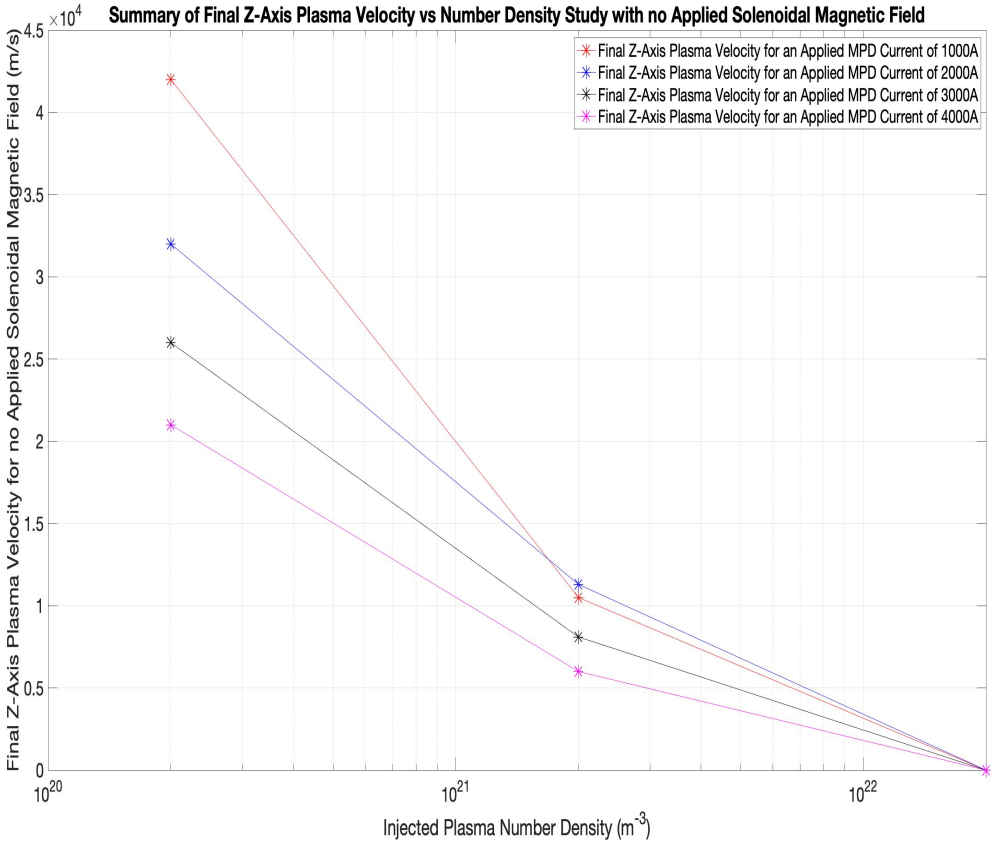

Figure 41: Summary of the effect of the plasma number density on the final z-axis velocity at the thruster outlet for no applied magnetic field.

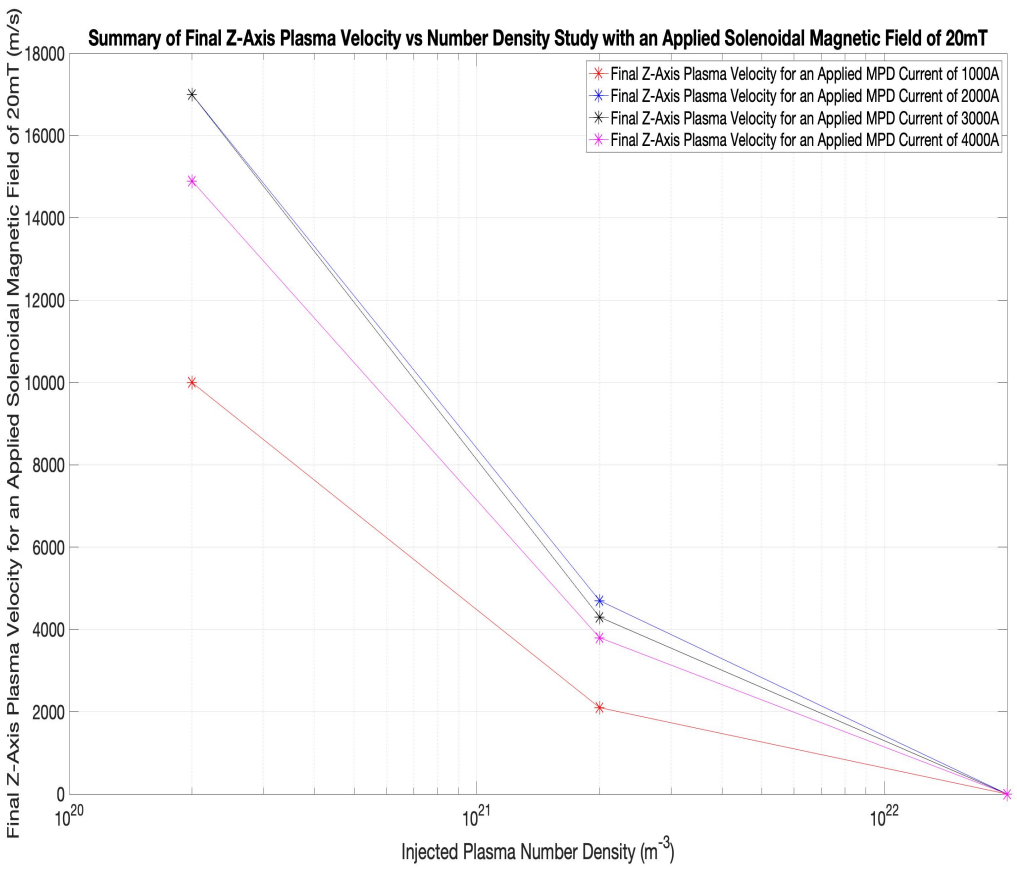

Figure 42: Summary of the effect of the plasma number density on the final z-axis velocity at the thruster outlet for an applied magnetic field of $20mT$.

Figure 41 shows that with the application of a higher plasma number density, the final z-axis velocity of the plasma at the thruster outlet decreases substantially. Figure 42 shows the same effect on the plasma with an applied magnetic field of $20mT$. It is worth noting the z-axis velocity is greater for the MPD with no applied magnetic field due to the transfer of axial energy to swirling motion in the plasma. Both figures show that for a plasma number density of $2 \times 10^{22} m^{-3}$, the final z-axis velocity is $0m/s$. Therefore, the plasma has become trapped in the MPD thruster. This is explained from Figure 40, in which it was demonstrated that the higher number density plasma induced a greater resistivity at the thruster inlet. The result of this is that a

plasma number density of $2 \times 10^{22} m^{-3} = 2 \times 10^{16} cm^{-3}$ is too great for a low-powered MPD thruster to effectively accelerate. Since the PLX experiment and PJMIF fusion schemes require plasma number densities on the order of $10^{17} cm^{-3}$ and $10^{18} cm^{-3}$ respectively, low-powered MPD thrusters are therefore not capable of functioning as heavy ion drivers for these devices. However, high-powered (applied currents on the order of $10,000A$ or higher) MPD thrusters could potentially accelerate plasmas of the required number densities to the required velocities and future work should be focused on the study of these MPD thrusters.

4.2.6 Summary of Long Run Time Studies

Figure 43 summarizes the final axial velocity achieved by the MPD for the currents of $1kA$, $2kA$, $3kA$, and $4kA$ with no applied magnetic field over a time range of $0s$ to $0.0011s$.

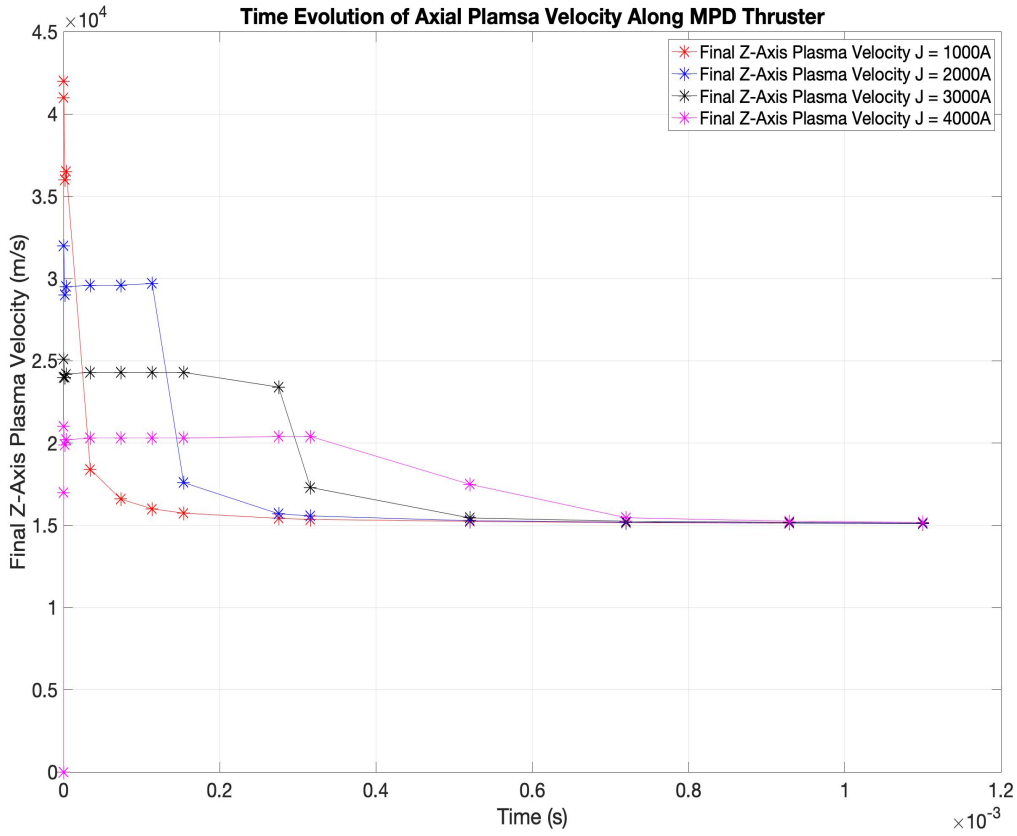

Figure 43: Summary of the evolution of the final axial velocity achieved by the MPD over a range of $0s$ to $0.0011s$ with no applied magnetic field.

Figure 43 shows that after only a few microseconds, the velocity achieved by the $1kA$ MPD drops below the higher currents. This is expected as the steady state simulations showed that a higher current should result in a greater achieved axial velocity. After a time of $0.1ms$, the axial velocity achieved by the $2kA$ MPD drops below the higher currents as well; and after a time of $0.32ms$ the axial velocity achieved by the $3kA$ MPD drops below that of the $4kA$ MPD. Therefore, after a time of $0.32ms$ the expected result of a higher applied current giving rise to a greater achieved axial velocity is observed. However, from Figure 43, it is also observed that the MPD thrusters appear to approach a steady state velocity on the order of $15km/s$.

This is much greater than the velocities observed in the steady state simulations given at the beginning of this chapter. There are several possible explanations for this. First, the steady state simulations were run using a vastly over-simplified model for the MPD thrusters where the currents were assumed to be entirely radial in direction and there were no induced magnetic fields in the plasma other than the magnetic field induced by the applied current density. This means that the velocities achieved in those models are smaller than would be expected in a real world MPD thruster, though they do give a lower bound on what should be expected from the MPD thrusters. Secondly, it is possible that the axial velocities on the order of $15km/s$ are quasi-steady state velocities, and that the thrusters have not yet reached their steady state operational values since it was observed that the final axial velocity was still decreasing at the time of $0.0011s$. Third, this observation could be the result of numerical instabilities within the code, as the final achieved axial velocities are known to be over estimates due to the simplified models used in this research. This is expanded on in the following section. It is clear, however, that these models do produce the expected result of a higher applied current giving rise to greater achieved axial velocity after a sufficient amount of time has elapsed.

4.2.7 Limitations of the Godunov Solver

As stated before there are several limitations of the Godunov solver. The first limitation is that the method cannot handle a true vacuum. There must be a plasma present everywhere in the solution domain. Therefore, there are interactions present between the plasma injected into the MPD chamber and the plasma used to model the vacuum density. This could potentially change the solution by a sizeable amount. As previously stated, the code used for these studies was taken from the open source Open-MHD code translated into Matlab. The translated code was extensively tested

against the results from the Open-MHD website and was able to successfully reproduce these results. However, these simulations were of plasma interactions between two different regions of plasma with similar densities and initial magnetic fields of much less magnitude. It is possible that the simulations in this thesis have pushed the code to or beyond the operational limits.

The second limitation is that this code uses the HLLD solver. This flux solver is more robust than the HLL and HLLC solvers, however it still has limitations. First, it does not consider the slow magnetosonic speeds in its solution of the Riemann problem. This indicates that there are instabilities in the plasma that are possibly not considered in the flux solver that could significantly affect the solution and plasma evolution. Second, in the approximate solution of the Riemann problem it is assumed that the normal velocity and total pressure are constant across the Riemann fan. This assumption works well for regions of plasma with similar densities, but the possibility exists in these simulations that since the two initial regions of plasma are very different with regards to mass density, pressure, magnitude of the magnetic field, and initial velocity that there are severe instabilities caused from the interactions of these two regions which significantly affect the solution. Future studies of this are required to test this solver for extreme conditions like those investigated in this thesis.

The third major limitation is that it only considers a single fluid MHD model; thus, restricting the solution region to one type of plasma. There are effects such as multi-fluid interactions that are necessary in the simulation of plasma drivers for PJMIF that are missed in this code base.

A fourth limitation of this code is that it uses the ideal gas law as its equation of state. Previous studies conducted on MPD thrusters were carried out with code bases that utilized more robust equations of state and collision capturing methods such as the viscous stress tensor. Numerous effects from the interactions of the plasma

particles with the current from the cathode to the anode and self interactions are missed by the assumption of an ideal gas law. Therefore, the final velocities achieved in these simulations are an over estimate of the plasma velocity as collisions (beyond that of basic resistivity) and viscous drag effects are ignored. It is also assumed that the plasma enters the MPD channel fully ionized, which is not true in most real world MPD thrusters. Since ionization effects are ignored in these simulations, this again gives rise to an over estimate of the plasma velocities. These limitations were accepted due to the fact that correcting for these limitations is a complicated process, requiring the use of higher order codes that are beyond the scope of this master's thesis.

V. Conclusions

5.1 Significant Results of this Research

The significant outcomes of these studies are as follows. First, in the steady state regime for initial velocities on the order of $1000m/s$, a plasma density of $n = 1\times10^{23}m^{-3}$ is the maximum critical operating density for low-powered MPD thrusters; at higher densities the resistivity becomes too great and the plasma is decelerated in the channel. Additionally, the time dependent simulations showed that when considering initial velocities on the order of $100m/s$, a plasma density of $2 \times 10^{22}m^{-3}$ is the maximum critical operating density for low powered MPD thrusters. At this density the plasma becomes trapped in the MPD chamber, rendering it useless for plasma acceleration. This is significant since PJMIF schemes require a dense plasma in order to function in the compression scheme.

The second significant outcome, resulting from the time dependent studies, is that the swirling motion caused by an applied solenoidal magnetic field was observed and found to be dependent on the strength of the applied magnetic field. As stated previously, this azimuthal motion can be converted into axial motion by the application of diverging magnetic fields. Therefore, an increase in the swirling motion of the plasma can lead to an increase in axial velocity of the plasma by application of a magnetic nozzle. It was also observed that the application of the solenoidal magnetic field increased the initial axial acceleration of the plasma column.

The third significant outcome was that the velocities achieved by the plasma column were very high, on the order of $10km/s$. These were much higher than in previous studies, due in large part to the increased initial pressure of the injected plasma. It was also observed that when a higher current was applied the plasma velocity was reduced since the plasma column was accelerated out of the chamber before

the plasma column could experience the full effect of the hydrodynamic expansion. It is worth noting that when the number density of the plasma column was increased, the achieved plasma velocity was severely reduced. This result shows that in order to achieve high plasma accelerations with a high number density plasma, high powered MPD thrusters must be used.

The conclusion of this thesis is that MPD thrusters show promise as a plasma accelerator for heavy ions; but low powered MPD thrusters cannot be used for PJMIF drivers, even with high initial plasma pressure, due to the maximum operational number density being below the required plasma density for PJMIF studies. It is however concerning that the plasma expands away from the z-axis at a very rapid rate. This could prove to be very detrimental to the efforts of the PJMIF scheme and should be limited as much as possible. It is the conclusion of the author that these results should be taken with some suspicion since the accepted limitations give an over estimate of the achieved plasma motion.

5.2 Future Work

Although this work has shown that MPD thrusters do show promise as heavy ion plasma accelerators, there is still much work to be done. As stated, this research uses simplified models in the analysis of the plasma physics. For future work it is imperative that these assumptions be removed and more physically realistic models be used, such as equations of state that include the effects of ionization. Several studies like this have already been conducted such as in [41]. In [41], a characteristics-based scheme was used to solve the solution of the ideal MHD equations for MPD thrusters and heavy ion accelerators. It was shown that this has the ability to capture time-dependent discontinuities and maintain force-free equilibrium. In [41] detailed models of classical transport were used as well as real equations of state and multi-

level ionization schemes. The code base used non-orthogonal meshes to better model the realistic flow-field geometries. This work also included multi-temperature effects for argon and lithium plasmas. With this code base, detailed models of gas-fed MPD thrusters were obtained as well as models of lithium Lorentz force accelerators [41]. This work work is considered to be one of the benchmark works for multi-dimensional modelling of MPD thrusters and is therefore the ideal place to start when building new multi-dimensional MPD models. One such avenue of new research could be extending this code base to handle the effects of both scalar and tensoral conductivity in the solution of the MHD equations, as well as modelling the multi-temperature effects and ionization schemes of xenon plasmas. It would also be of interest to replace the energy density equation with an equation concerning the entropy density. This should be done since the energy density equation is very inefficient at handling physical scenarios that have very high magnetic energy densities such as those found in high powered MPD thrusters or astrophysical models.

The steady state models should be investigated in the full 3D regime. This can be done as in [42] with the use of the variational form of the steady state MHD equations and flux surfaces with a finite element method. It is most important, however, that the time dependent MPD thrusters be investigated with higher order numerical methods; such as Particle in Cell (PIC) or full kinetic theory codes like Discontinuous Galerkin methods [24]. This should be the primary focus of future work on this topic as it is the belief of this author that the Godunov method used in this analysis cannot support the more detailed investigation that is required for future work. It is also the belief of the author that these efforts should focus on the investigation of advanced kinetic theory methods as it is imperative that these types of models be used to investigate the plasma compression at a detailed level. This should be done so as to engineer a method of plasma beam compression that can create

the necessary conditions for effective target compression. A steady state analysis of beam compression was attempted for this thesis, but the results were inconclusive and require a more detailed analysis before final results can be demonstrated.

Appendix A. Additional Results

A.1 Additional Steady State Results

A.1.1 Additional Current and Velocity Studies

A current of $2000A$ was applied to the MPD.

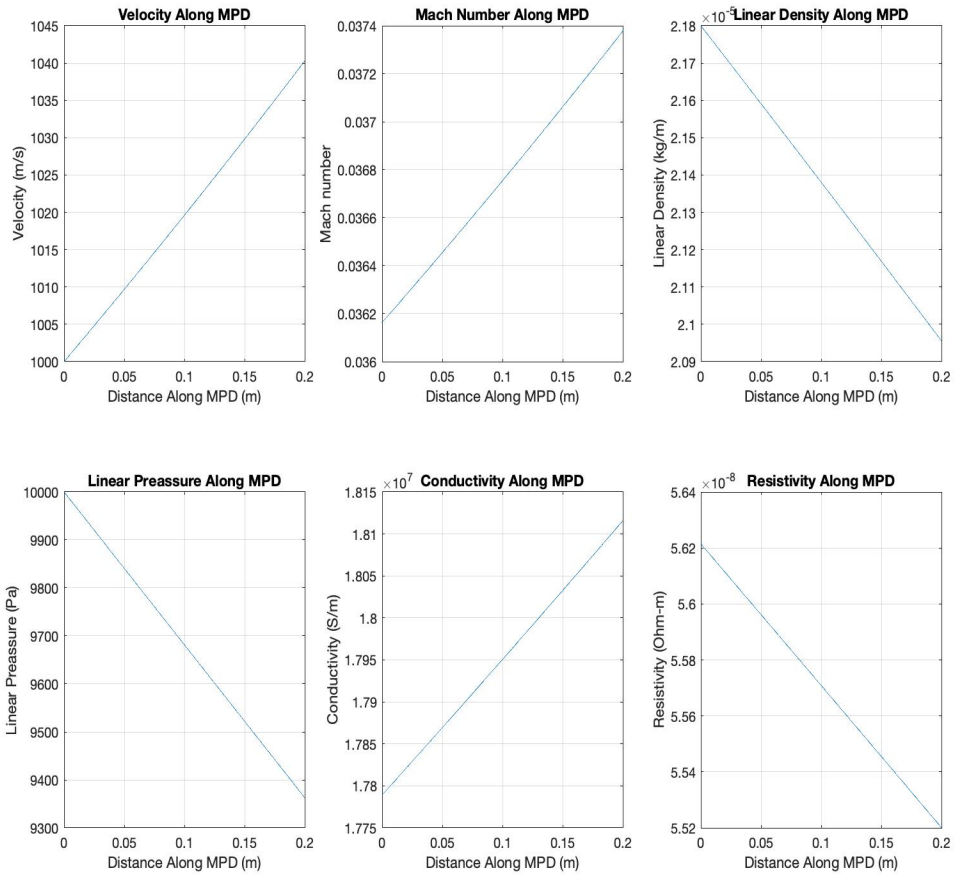

Figure 44: Steady State MPD Thruster with $J = 2000A$ and $u_0 = 1000m/s$

Figure 44 shows that the plasma achieves a higher acceleration, but the final velocity is still much too small to be of use for heavy ion drivers. It is also worth noting that the linear density expands away from the z-axis more rapidly, but the

expansion is still quite small. In order to achieve a high acceleration in the steady state limit, a high current must be applied to the MPD thruster; but, this will cause the plasma to expand away from the z-axis more rapidly. To test this theory, a current of $6000A$ is applied to the MPD.

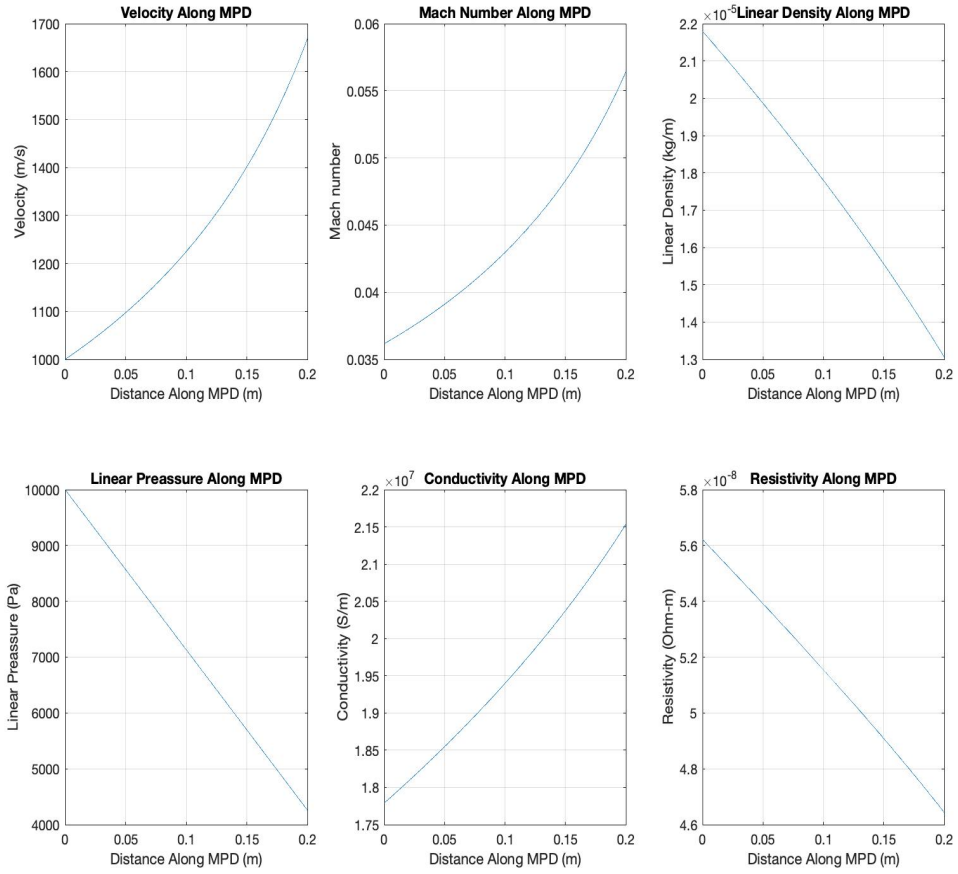

Figure 45: Steady State MPD Thruster with $J = 6000A$ and $u_0 = 1000m/s$

Figure 45 demonstrates that the plasma now achieves a much higher acceleration, with a final velocity $700m/s$ greater than the initial velocity. However, this is still a relatively small acceleration when compared to what is needed for a heavy ion driver. It also shows that the density now expands away from the z-axis more rapidly than in

the previous cases, but remains on the same order of magnitude as the initial plasma density. This affirms that in the lower power limit of the steady state regime, the plasma expansion remains minimal. An important property for heavy ion drivers, the expansion should remain at a minimal level to provide the force necessary to compress the target; but this acceleration is still too small for the initial stage of the driver for PJMIF experiments.

Next, the current will be returned to $1000A$, with the initial velocity set to $2000m/s$.

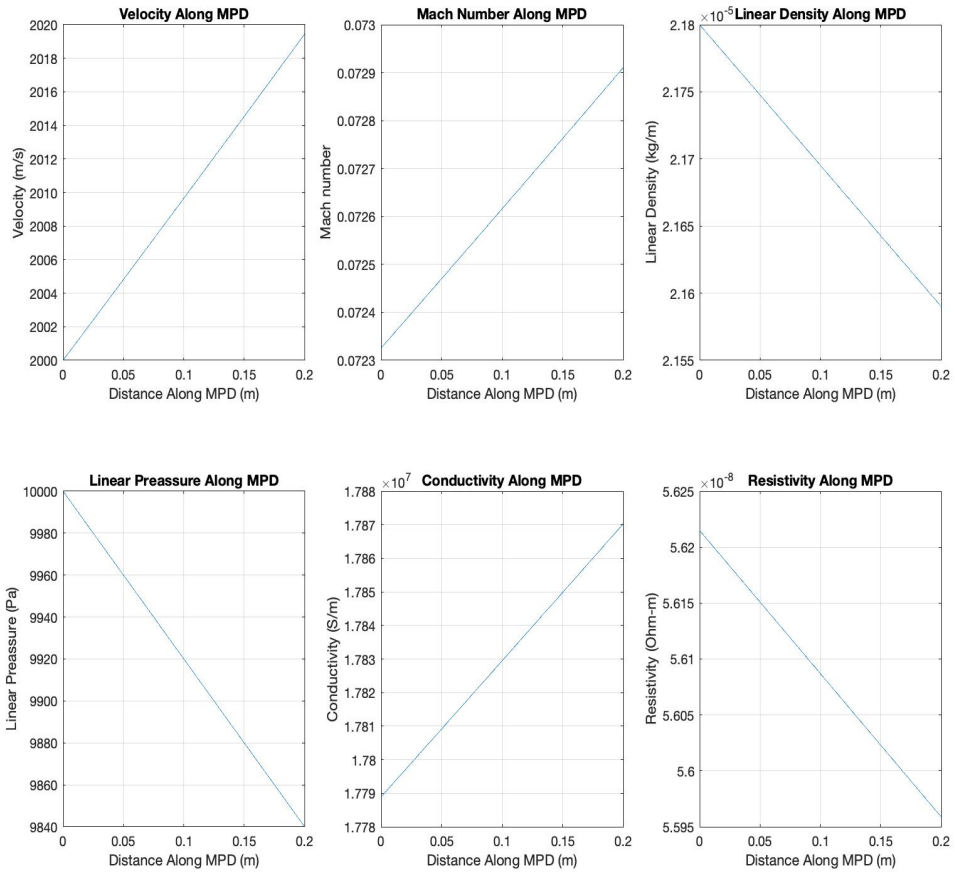

Figure 46: Steady State MPD Thruster with $J = 1000A$ and $u_0 = 2000m/s$

Figure 46 shows the acceleration achieved by the plasma is slightly greater than the previous case, but the acceleration is still much too small to be of use. The plasma expands away from the z-axis with little change from the previous case. It is worth noting that the resistivity is slightly smaller than in the previous case. This is important since the plasma will have a greater final velocity if the resistivity felt by the plasma is minimized.

Next, the current will be set to $6000A$ and the initial velocity will remain $2000m/s$.

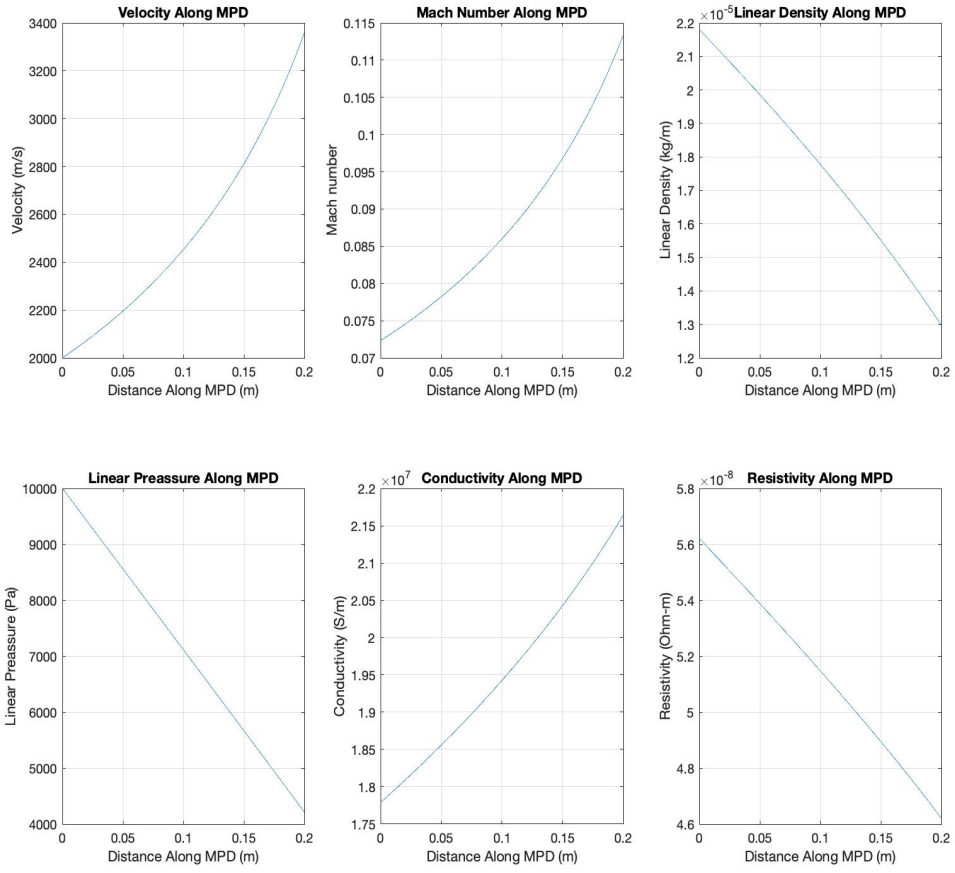

Figure 47: Steady State MPD Thruster with $J = 6000A$ and $u_0 = 2000m/s$

Figure 47 demonstrates that the current of $6000A$ has increased the acceleration of

the plasma, specifically it has accelerated the plasma resulting in a velocity increase of $1400m/s$. This is a great improvement over the previous cases with both lower current and the same applied current, but with an initial velocity of $1000m/s$. This predicts that in the steady state limit, higher currents give rise to higher accelerations. However, the acceleration shown here is still too small for a heavy ion plasma driver's initial stage. It is also worth noting that the plasma expands away from the z-axis at a higher rate, which is reflected in the resistivity reaching a lower value than in the previous cases.

A.1.2 Additional Pressure Studies

The current is raised to $2000A$ and the initial velocity is kept at $1000m/s$.

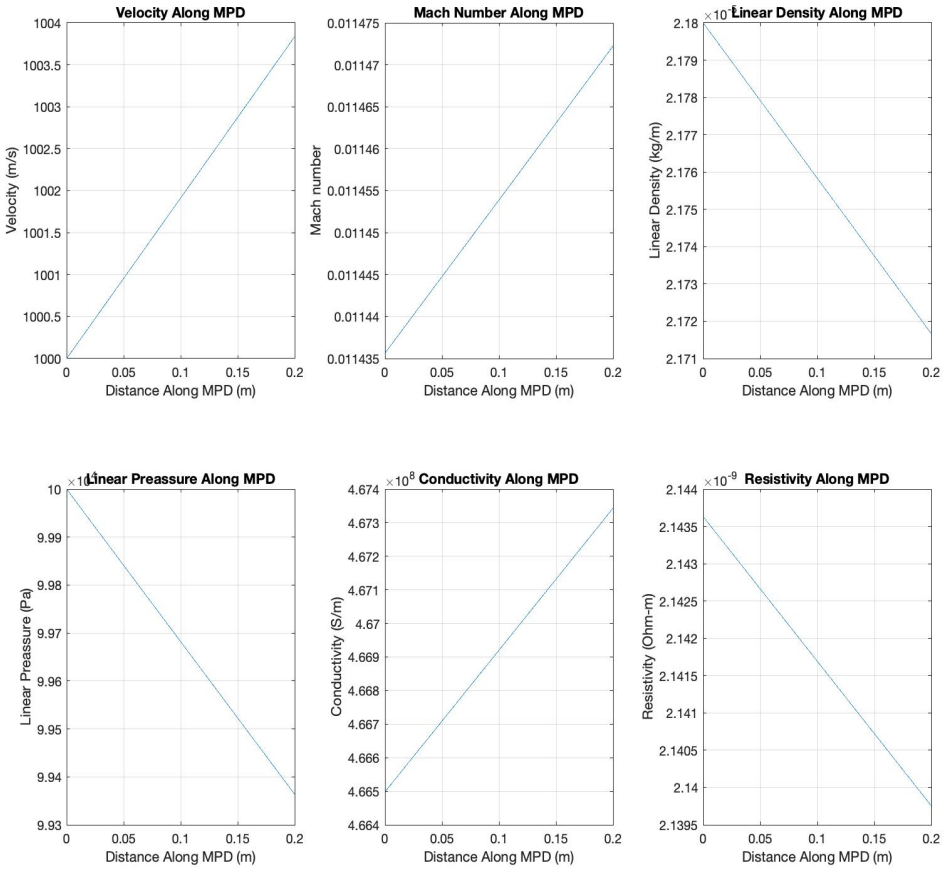

Figure 48: Steady State MPD Thruster with $J = 2000A$, $u_0 = 1000m/s$, and $p_0 = 10^5 Pa$

Figure 48 shows that the plasma acceleration is again slowed substantially; specifically, the plasma velocity is only increased by $4m/s$. This is again incredibly poor and of no use for a heavy ion driver. The plasma density also shows that the plasma expands away from the z-axis at approximately the same rate. It appears that at pressures beyond $10^4 Pa$ in the steady state limit. Even when the current is raised by $1000A$, the plasma velocity and expansion remain relatively constant. To test this the current is raised to $6000A$.

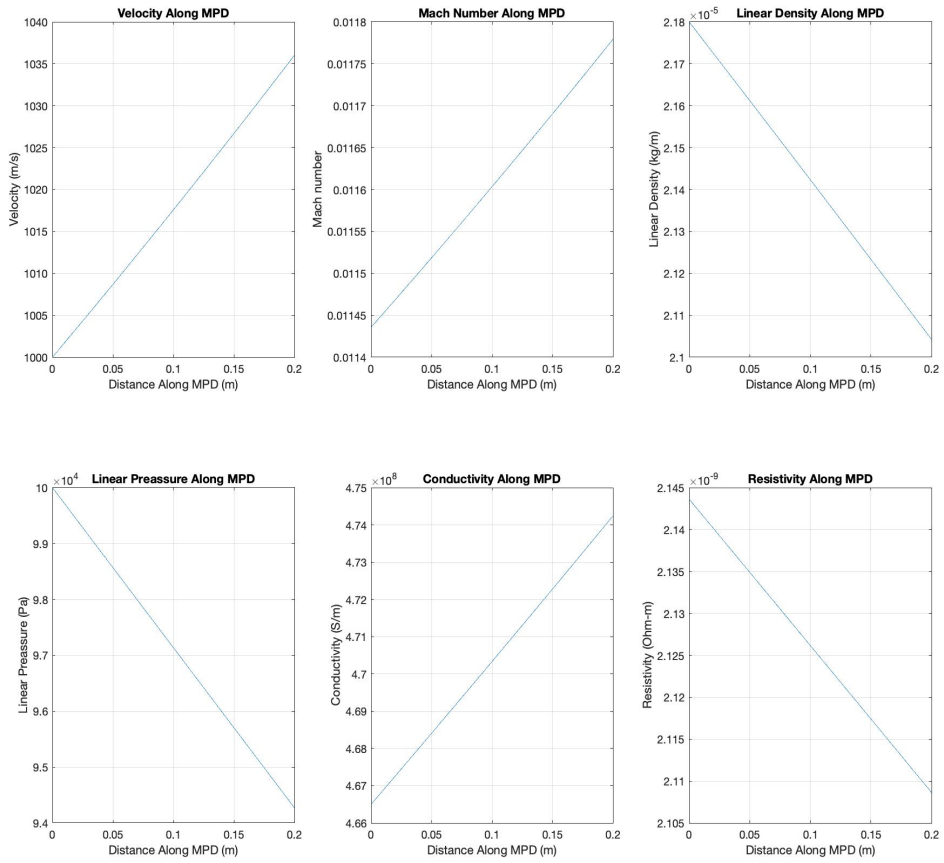

Figure 49: Steady State MPD Thruster with $J = 6000A$, $u_0 = 1000m/s$, and $p_0 = 10^5 Pa$

Figure 49 demonstrates that the plasma velocity is increased only by $40m/s$. This is again much too small for any plasma driver. The plasma density also shows that the plasma expands away from the z-axis at a rate nearly identical to the previous cases. This confirms that at pressures higher than $10^4 Pa$ and low initial velocity the plasma expansion rate and acceleration remain approximately constant when comparing differing applied currents.

A.1.3 Additional Number Density Studies

The plasma density of $10^{22}m^{-3}$ is studied.

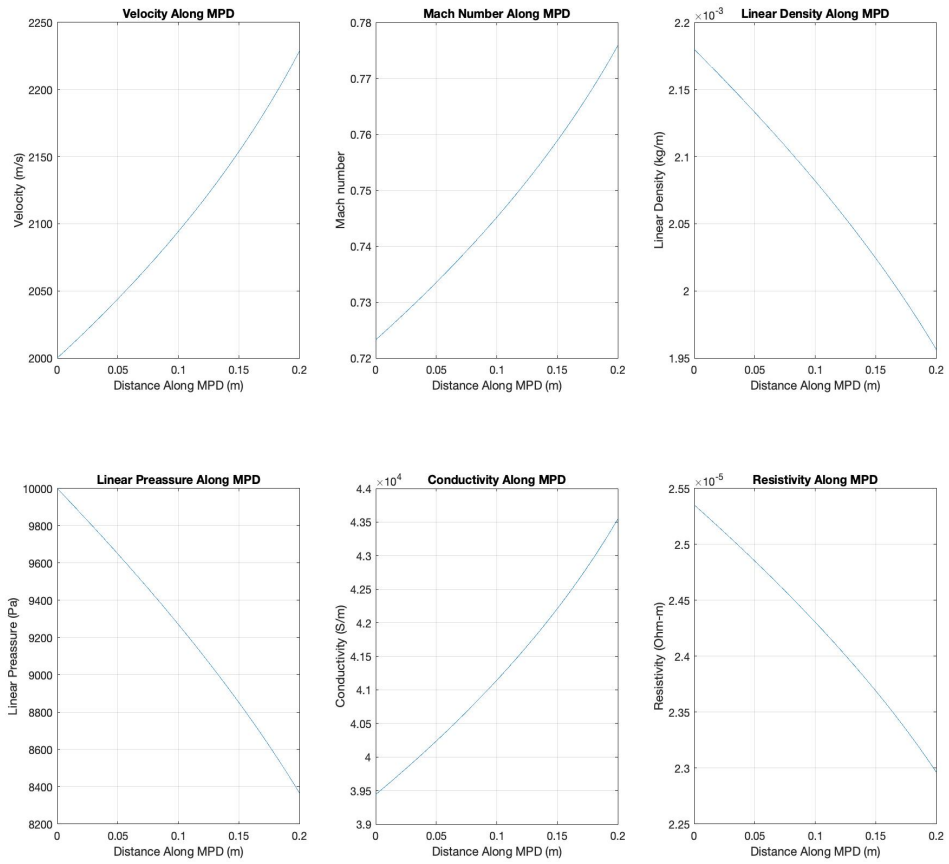

Figure 50: Steady State MPD Thruster with $J = 2000A$, $u_0 = 2000m/s$, and $n = 10^{22}m^{-3}$

Figure 50 shows that the plasma velocity receives a sizeable acceleration, where the final velocity is increased $225m/s$. This is a surprising result as the resistivity has increased by a full order of magnitude. From this it can be hypothesized that in the steady state limit, the increased number of interactions has actually amplified the acceleration mechanism along the MPD channel. This could potentially be utilized

in steady state scenarios to possibly provide for greater thrust. It is also possible that there are numerical instabilities causing this as well. These will be discussed in the following sub-section.

Next, the plasma density of $10^{23}m^{-3}$ is tested with the same MPD thruster.

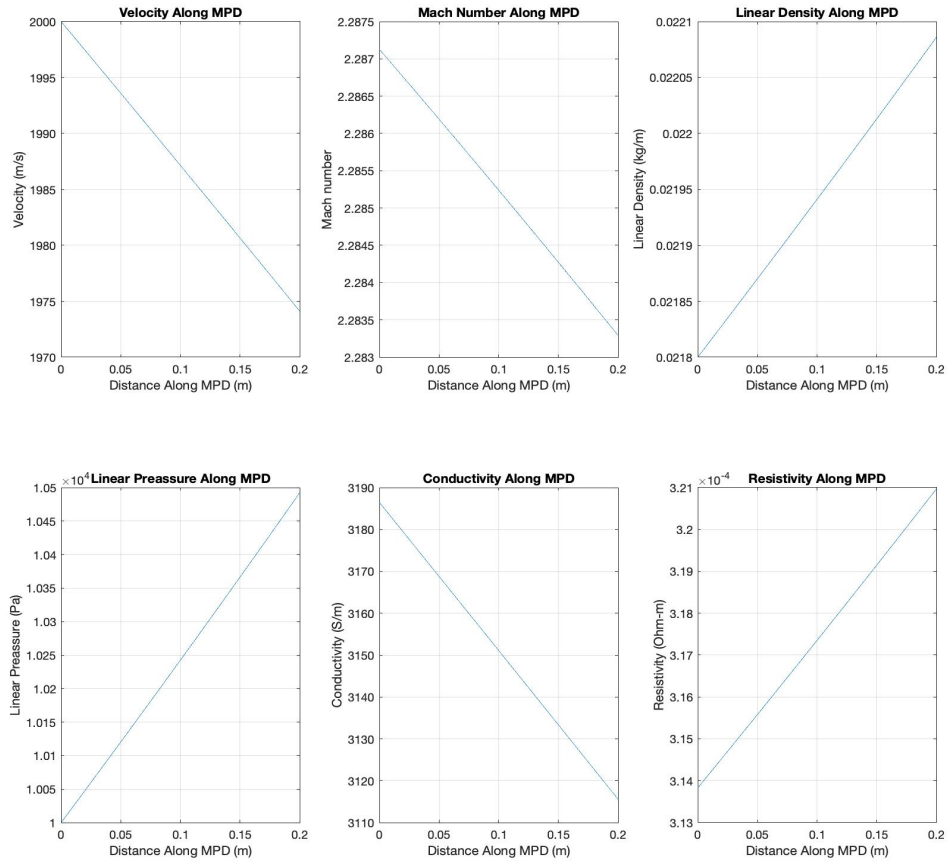

Figure 51: Steady State MPD Thruster with $J = 2000A$, $u_0 = 2000m/s$, and $n = 10^{23}m^{-3}$

Figure 51 shows that the plasma velocity has decreased along the MPD channel. This is related to the full order of magnitude increase in resistivity when compared to the previous case with a plasma density of $10^{22}m^{-3}$. Clearly this resistivity is too great for the initial plasma injection and causes the plasma to decelerate. This alludes

to the possibility of $n = 10^{23}m^{-3}$ being a critical number density in the steady state regime. To test this, a current of $6000A$ is applied to the MPD thruster along with the initial velocity being increased to $2000m/s$ in order to observe the MPD operating with both a higher applied current and initial velocity.

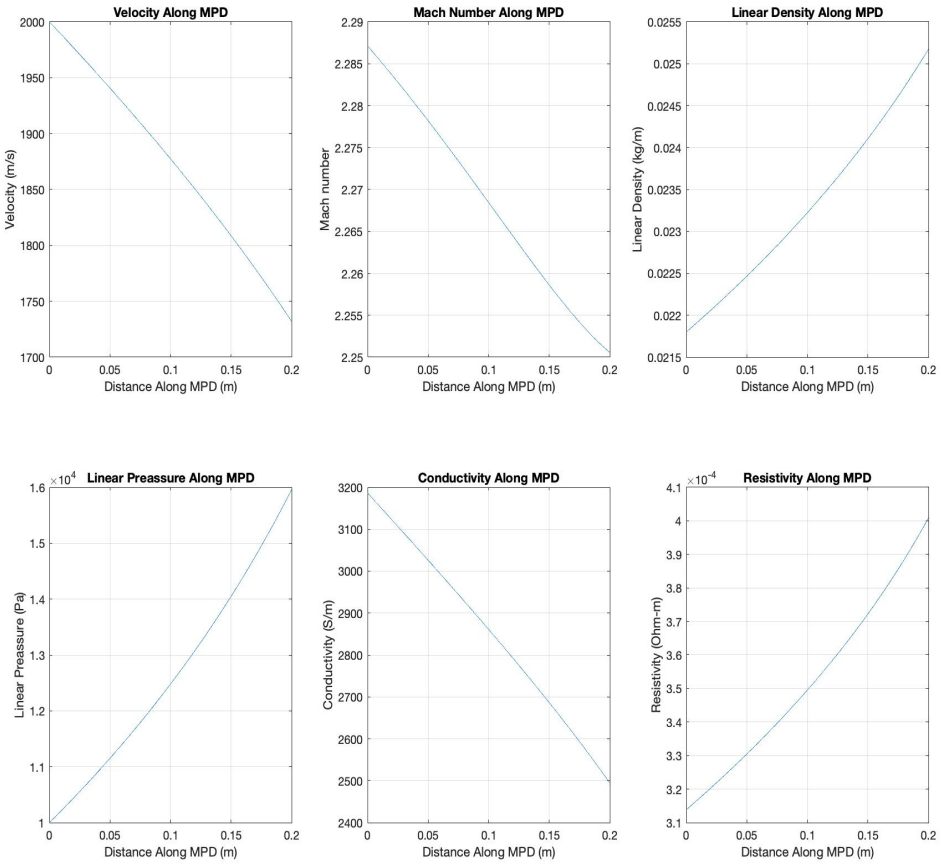

Figure 52: Steady State MPD Thruster with $J = 6000A$, $u_0 = 2000m/s$, and $n = 10^{23}m^{-3}$

Figure 52 shows the plasma velocity decreasing along the MPD channel for this scenario as well. From this it can be deduced that for low power, steady state MPD thrusters, $n = 10^{23}m^{-3}$ is the maximum critical operating number density; at which the resistivity becomes too great for the thruster to overcome and the plasma is

reduced in velocity. This proves that if the initial plasma velocity is too small, the plasma will become trapped in the MPD thruster. This will be investigated in the time dependent studies.

A.2 Additional Time-Dependent Results

A.2.1 Additional Vacuum Density Studies

A vacuum density of 10^{-4} that of the initial plasma density is examined.

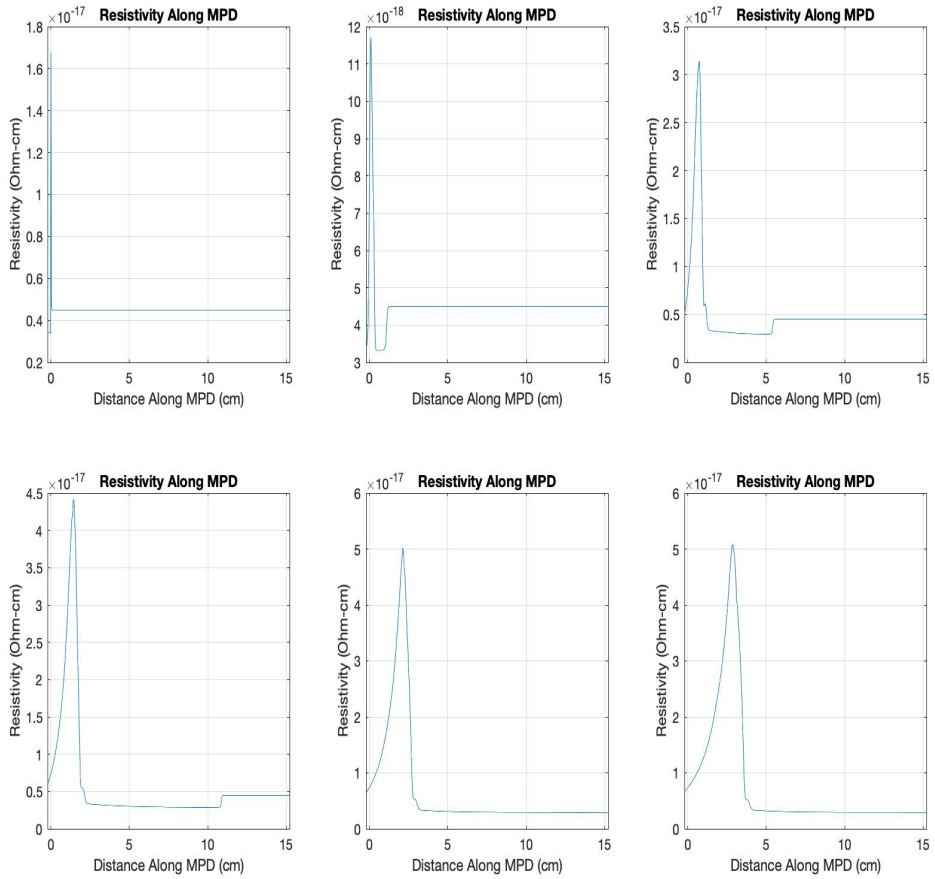

Figure 53: Evolution of the plasma resistivity for a vacuum density 10^{-4} that of the plasma density. The upper left figure is at the initial time of $t = 0s$, the upper middle figure is at a time of $t = 1.2 \times 10^{-7}s$, the upper right figure is at a time of $t = 1.8 \times 10^{-7}s$, the bottom left figure is at a time of $t = 2.4 \times 10^{-7}s$, the middle left figure is at a time of $t = 3.0 \times 10^{-7}s$, and the bottom left figure is at a time of $t = 3.6 \times 10^{-7}s$.

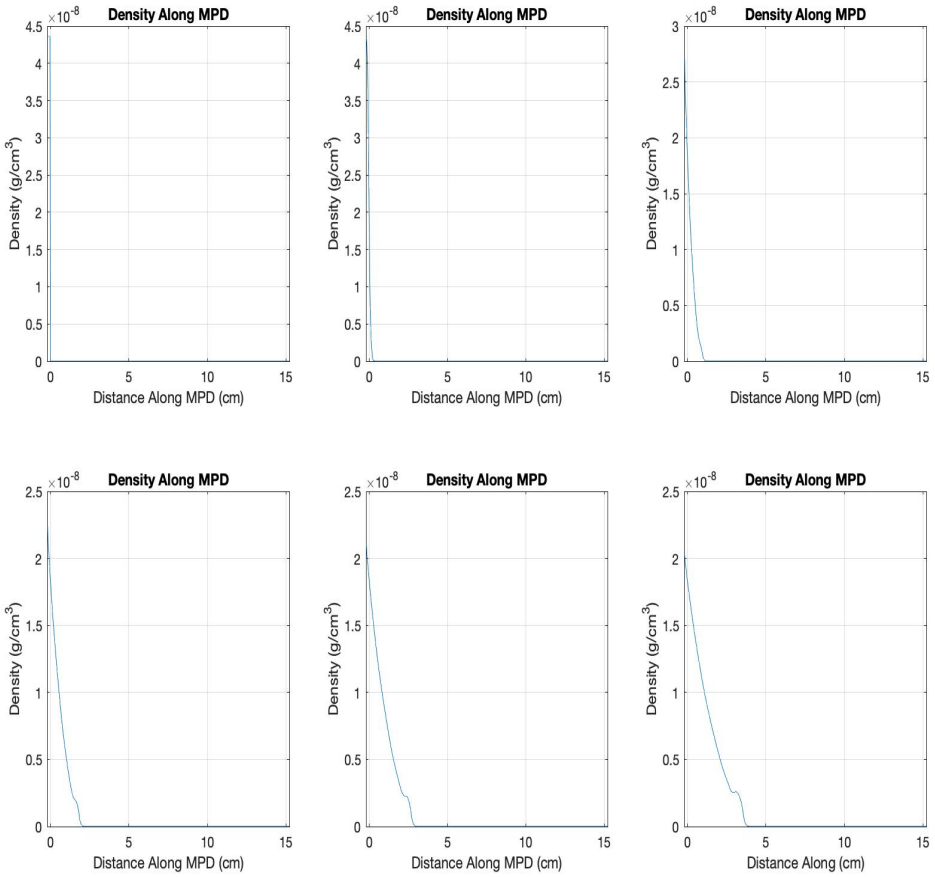

Figure 54: Evolution of the plasma density for a vacuum density 10^{-4} that of the plasma density. The upper left figure is at the initial time of $t = 0s$, the upper middle figure is at a time of $t = 1.2 \times 10^{-7}s$, the upper right figure is at a time of $t = 1.8 \times 10^{-7}s$, the bottom left figure is at a time of $t = 2.4 \times 10^{-7}s$, the middle left figure is at a time of $t = 3.0 \times 10^{-7}s$, and the bottom left figure is at a time of $t = 3.6 \times 10^{-7}s$.

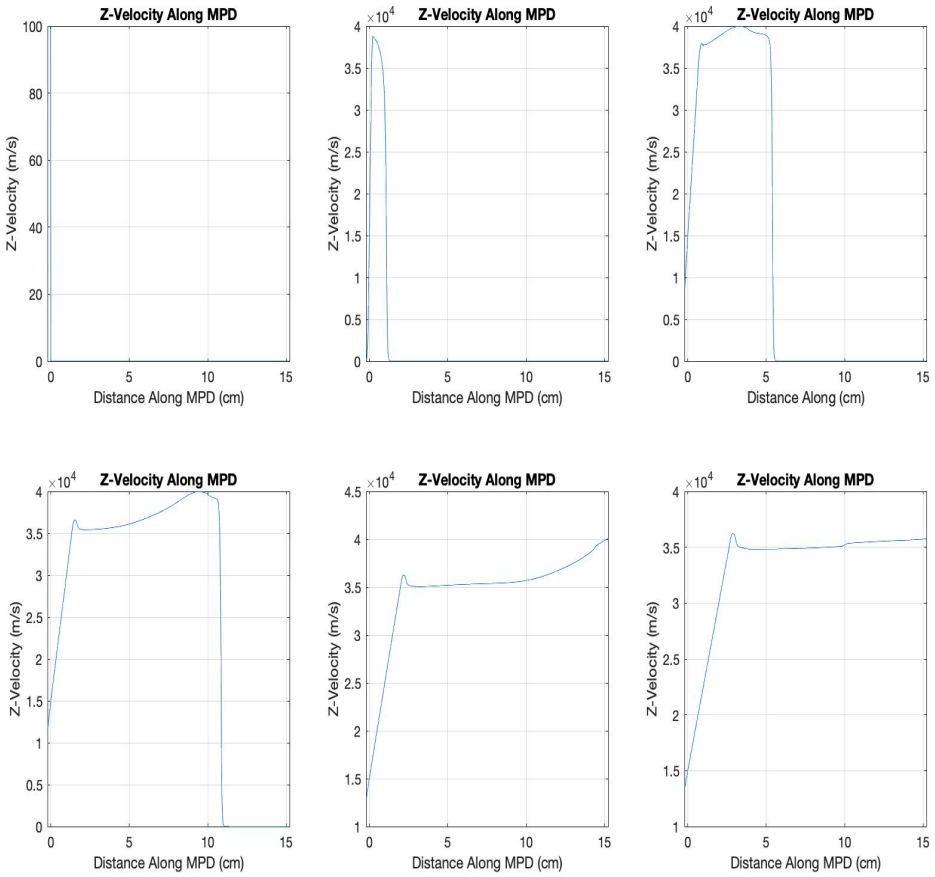

Figure 55: Evolution of the axial velocity for a vacuum density 10^{-4} that of the plasma density. The upper left figure is at the initial time of $t = 0s$, the upper middle figure is at a time of $t = 1.2 \times 10^{-7}s$, the upper right figure is at a time of $t = 1.8 \times 10^{-7}s$, the bottom left figure is at a time of $t = 2.4 \times 10^{-7}s$, the middle left figure is at a time of $t = 3.0 \times 10^{-7}s$, and the bottom left figure is at a time of $t = 3.6 \times 10^{-7}s$.

In Figure 53 the resistivity along the z-axis of the MPD is shown. In comparison with Figure 21, it shows that the resistivity is confined to the inlet region where the initial plasma expansion is most extreme. This is reflected in Figure 54, where the the plasma density declines more smoothly and more rapidly along the z-axis of the channel. In comparing Figure 55 and Figure 23 the effect that the vacuum plasma

density has on the injected plasma is shown to be that a larger velocity is obtained with the smaller vacuum density. It is also observed that the plasma exhibits fewer oscillations in the z velocity along the MPD channel, affirming that the lower vacuum plasma density has a smaller effect on the injected plasma motion.

Next, a vacuum density of 10^{-5} that of the initial plasma density is examined.

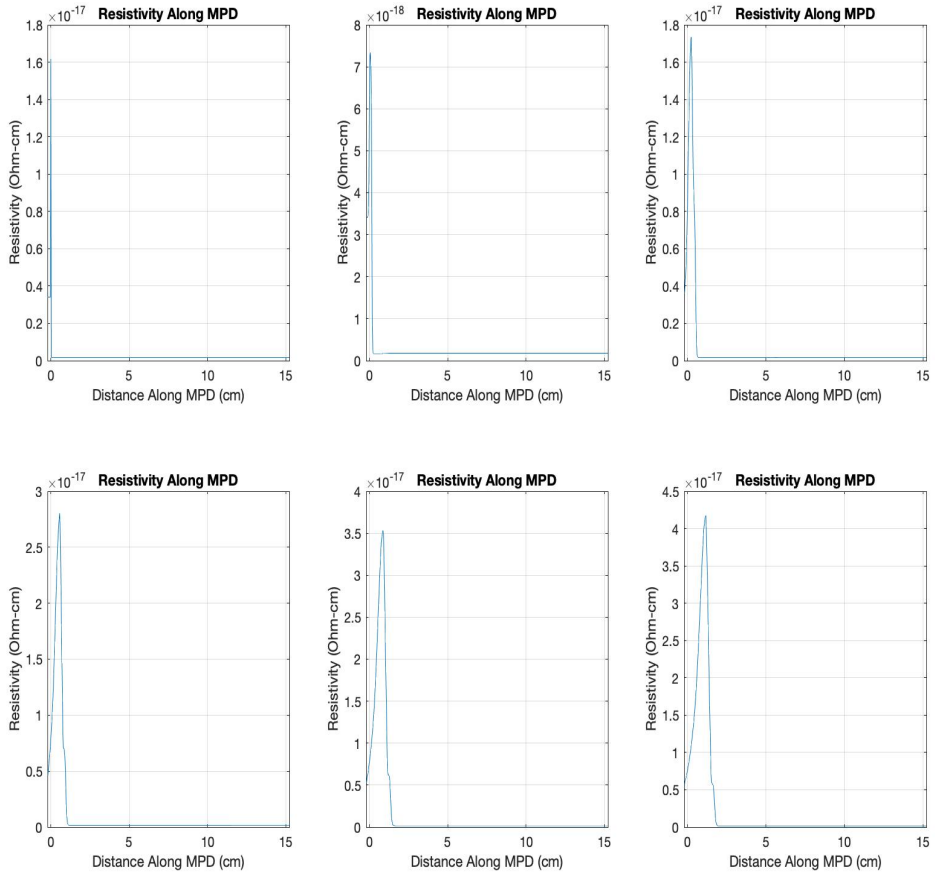

Figure 56: Evolution of the plasma resistivity for a vacuum density 10^{-5} that of the plasma density. The upper left figure is at the initial time of $t = 0s$, the upper middle figure is at a time of $t = 1.2 \times 10^{-7}s$, the upper right figure is at a time of $t = 1.8 \times 10^{-7}s$, the bottom left figure is at a time of $t = 2.4 \times 10^{-7}s$, the middle left figure is at a time of $t = 3.0 \times 10^{-7}s$, and the bottom left figure is at a time of $t = 3.6 \times 10^{-7}s$.

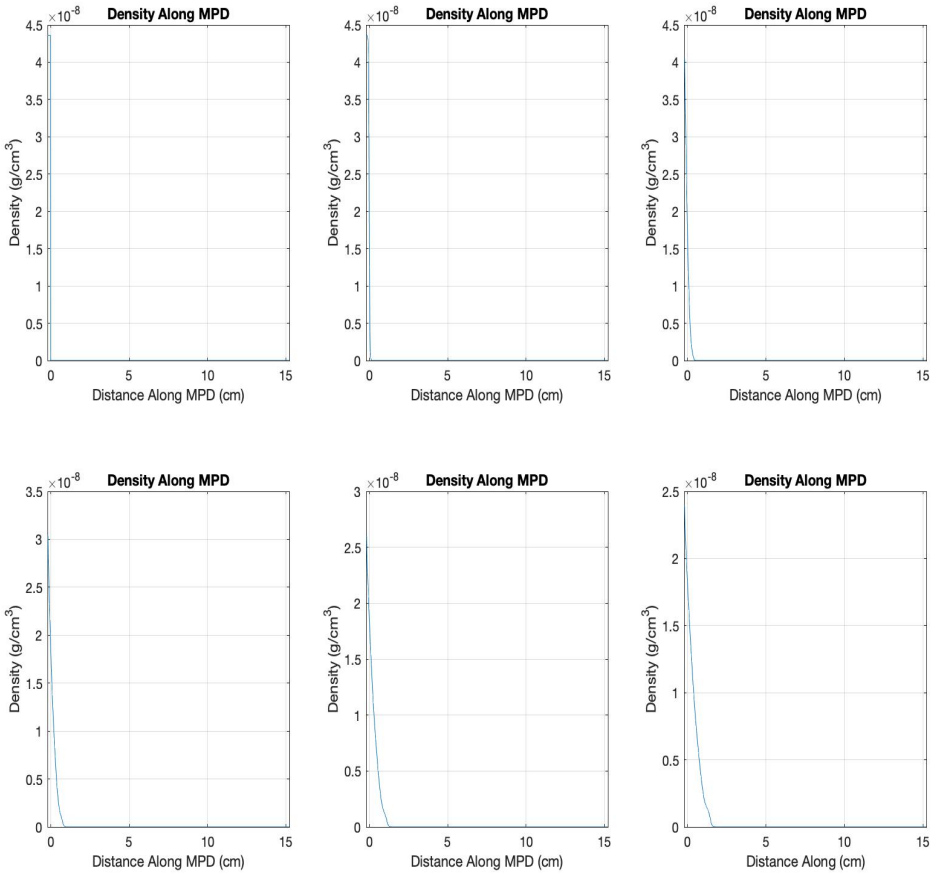

Figure 57: Evolution of the plasma density for a vacuum density 10^{-5} that of the plasma density. The upper left figure is at the initial time of $t = 0s$, the upper middle figure is at a time of $t = 1.2 \times 10^{-7}s$, the upper right figure is at a time of $t = 1.8 \times 10^{-7}s$, the bottom left figure is at a time of $t = 2.4 \times 10^{-7}s$, the middle left figure is at a time of $t = 3.0 \times 10^{-7}s$, and the bottom left figure is at a time of $t = 3.6 \times 10^{-7}s$.

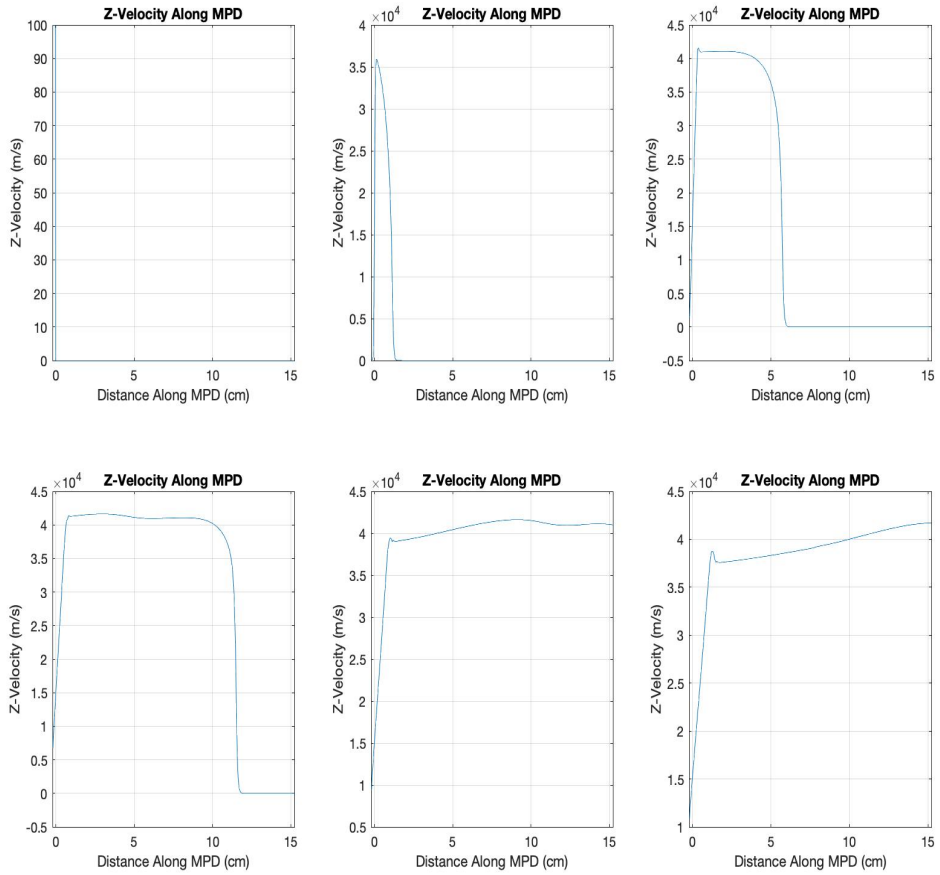

Figure 58: Evolution of the axial velocity for a vacuum density 10^{-5} that of the plasma density. The upper left figure is at the initial time of $t = 0s$, the upper middle figure is at a time of $t = 1.2 \times 10^{-7}s$, the upper right figure is at a time of $t = 1.8 \times 10^{-7}s$, the bottom left figure is at a time of $t = 2.4 \times 10^{-7}s$, the middle left figure is at a time of $t = 3.0 \times 10^{-7}s$, and the bottom left figure is at a time of $t = 3.6 \times 10^{-7}s$.

In Figure 56 the resistivity along the z-axis of the MPD is shown. The resistivity reaches a smaller value with a vacuum density of 10^{-5} times the initial density of injected plasma when compared to the other vacuum densities. This is reflected in Figure 57 which shows that the plasma expands away from the z-axis much more rapidly with the decrease in the vacuum density. Figure 58, however, shows that the

velocity along the z-axis of the channel reaches a value similar to Figure 55. Figure 58 also demonstrates that with a lower vacuum density, almost no oscillations are seen in the z velocity of the plasma along the MPD channel.

Next, a vacuum density of 10^{-6} that of the initial plasma density is examined.

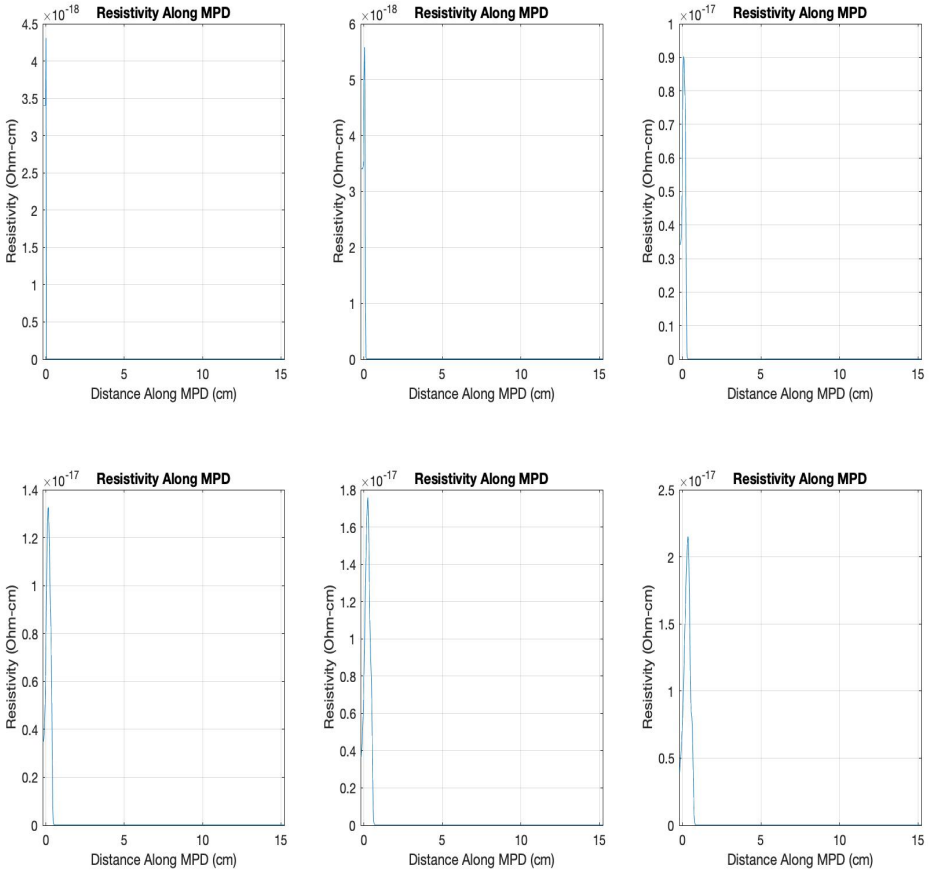

Figure 59: Evolution of the plasma resistivity for a vacuum density 10^{-6} that of the plasma density. The upper left figure is at the initial time of $t = 0s$, the upper middle figure is at a time of $t = 1.2 \times 10^{-7}s$, the upper right figure is at a time of $t = 1.8 \times 10^{-7}s$, the bottom left figure is at a time of $t = 2.4 \times 10^{-7}s$, the middle left figure is at a time of $t = 3.0 \times 10^{-7}s$, and the bottom left figure is at a time of $t = 3.6 \times 10^{-7}s$.

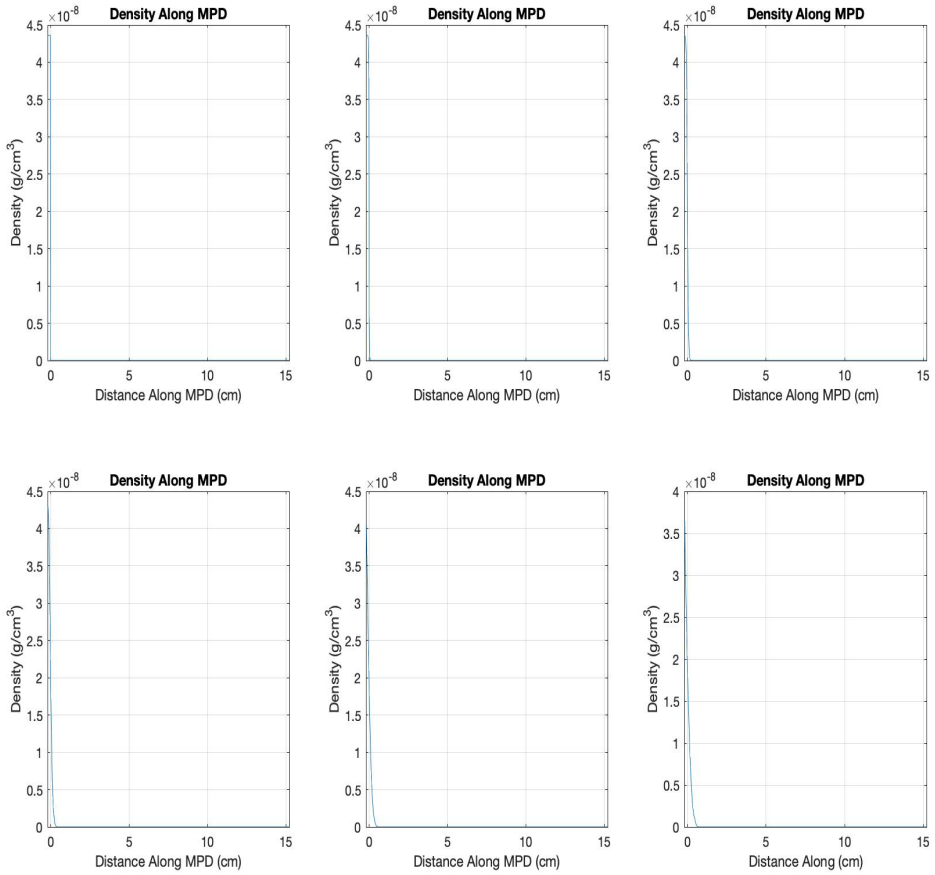

Figure 60: Evolution of the plasma density for a vacuum density 10^{-6} that of the plasma density. The upper left figure is at the initial time of $t = 0s$, the upper middle figure is at a time of $t = 1.2 \times 10^{-7}s$, the upper right figure is at a time of $t = 1.8 \times 10^{-7}s$, the bottom left figure is at a time of $t = 2.4 \times 10^{-7}s$, the middle left figure is at a time of $t = 3.0 \times 10^{-7}s$, and the bottom left figure is at a time of $t = 3.6 \times 10^{-7}s$.

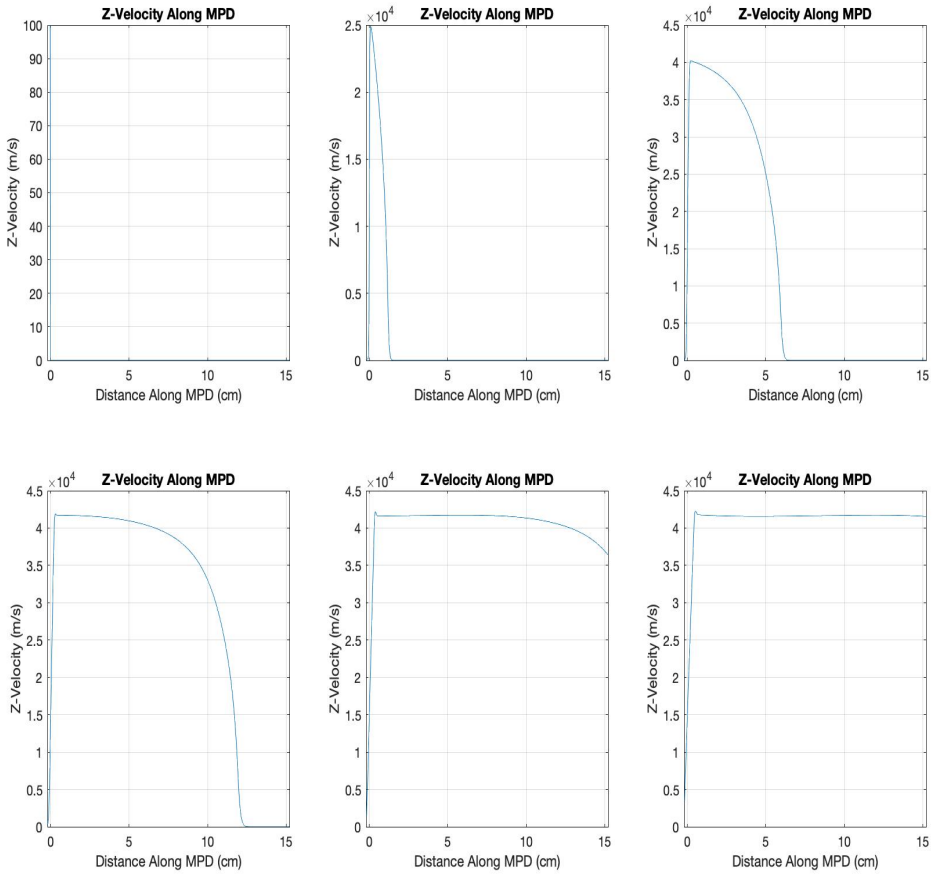

Figure 61: Evolution of the axial velocity for a vacuum density 10^{-6} that of the plasma density. The upper left figure is at the initial time of $t = 0s$, the upper middle figure is at a time of $t = 1.2 \times 10^{-7}s$, the upper right figure is at a time of $t = 1.8 \times 10^{-7}s$, the bottom left figure is at a time of $t = 2.4 \times 10^{-7}s$, the middle left figure is at a time of $t = 3.0 \times 10^{-7}s$, and the bottom left figure is at a time of $t = 3.6 \times 10^{-7}s$.

In Figure 59 the resistivity along the z-axis of the MPD is shown, where the resistivity reaches a smaller value. This is reflected in Figure 60 where the plasma expansion is shown to be more rapid with the decreased vacuum density. However, Figure 61 shows the velocity along the z-axis reaches the same value as the vacuum density of the previous case. Figure 61 also shows that the z velocity experiences

almost no oscillations along the MPD channel, just as observed in the 10^{-5} case as well.

A.2.2 Additional Applied Current Studies

A current of $2000A$ is applied to the MPD thruster with a vacuum density of 10^{-5} that of the initial plasma density.

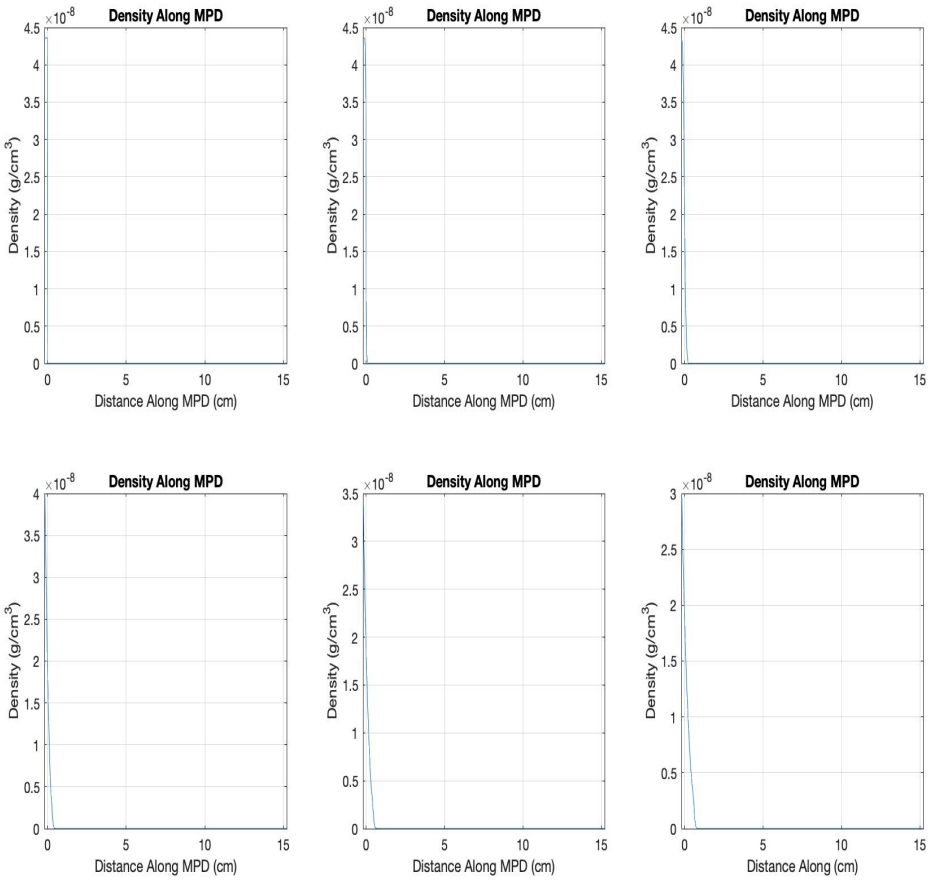

Figure 62: Evolution of the plasma density for J = 2000A and vacuum density 10^{-5} that of the plasma density. The upper left figure is at the initial time of $t = 0s$, the upper middle figure is at a time of $t = 1.2 \times 10^{-7}s$, the upper right figure is at a time of $t = 1.8 \times 10^{-7}s$, the bottom left figure is at a time of $t = 2.4 \times 10^{-7}s$, the middle left figure is at a time of $t = 3.0 \times 10^{-7}s$, and the bottom left figure is at a time of $t = 3.6 \times 10^{-7}s$.

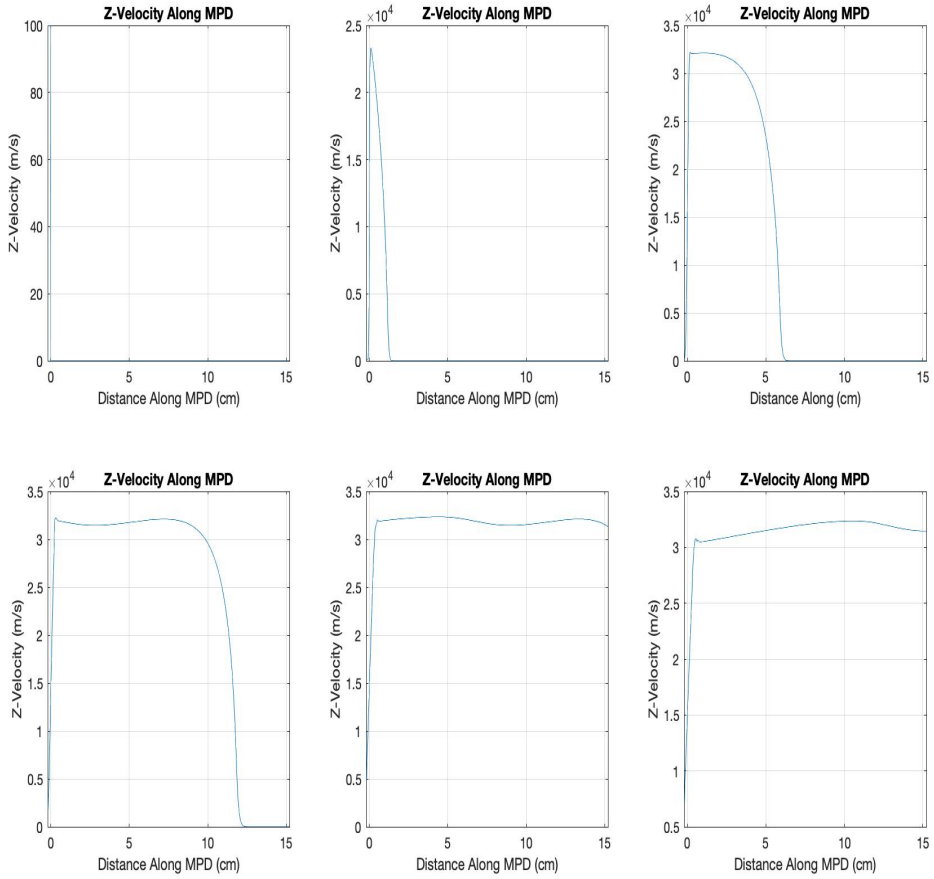

Figure 63: Evolution of the axial velocity for J = $2000A$ and vacuum density 10^{-5} that of the plasma density. The upper left figure is at the initial time of $t = 0s$, the upper middle figure is at a time of $t = 1.2 \times 10^{-7}s$, the upper right figure is at a time of $t = 1.8 \times 10^{-7}s$, the bottom left figure is at a time of $t = 2.4 \times 10^{-7}s$, the middle left figure is at a time of $t = 3.0 \times 10^{-7}s$, and the bottom left figure is at a time of $t = 3.6 \times 10^{-7}s$.

Figure 62 shows that the plasma expands rapidly away from the z-axis, as expected. Figure 63 shows that a final velocity of $3.2 * 10^4 m/s$ is achieved at the end of the MPD channel. This acceleration is still substantial, but has decreased by $10km/s$ from the $1000A$ case. This is a peculiar result, because as previously stated it is

expected that a higher current should translate to higher final velocity. It is the belief of the author that there are two main contributing factors to this outcome. First, the density decreases at a slightly slower rate than the $1000A$ case. This would cause an increase in the number of self interactions at the inlet surface, which causes extraneous acceleration effects. Second, and much more substantial, we could in fact be seeing an increase in acceleration of the plasma, but this decreases the effect of the hydrodynamic expansion and acceleration. Since a lower current implies a lower initial acceleration, the plasma has a longer time to spend inside the plasma chamber where it is further accelerated by the plasma column with a large number density moving from a very high pressure environment to a low pressure environment. The higher current would give the plasma column a higher initial acceleration, thus it would have less time to experience the effects of the hydrodynamic expansion and acceleration. This possibly implies a method of creating very high powered MPD thrusters with very low applied current. It is also possible that these substantial accelerations are caused by numerical instabilities. This will be discussed in a later section. It is also possible that there are effects that are not being captured in 1D that would be captured in 2D or 3D simulations, which are the subject of future work.

Next, a current of $3000A$ is applied to the MPD thruster with a vacuum density of 10^{-5} that of the initial plasma density.

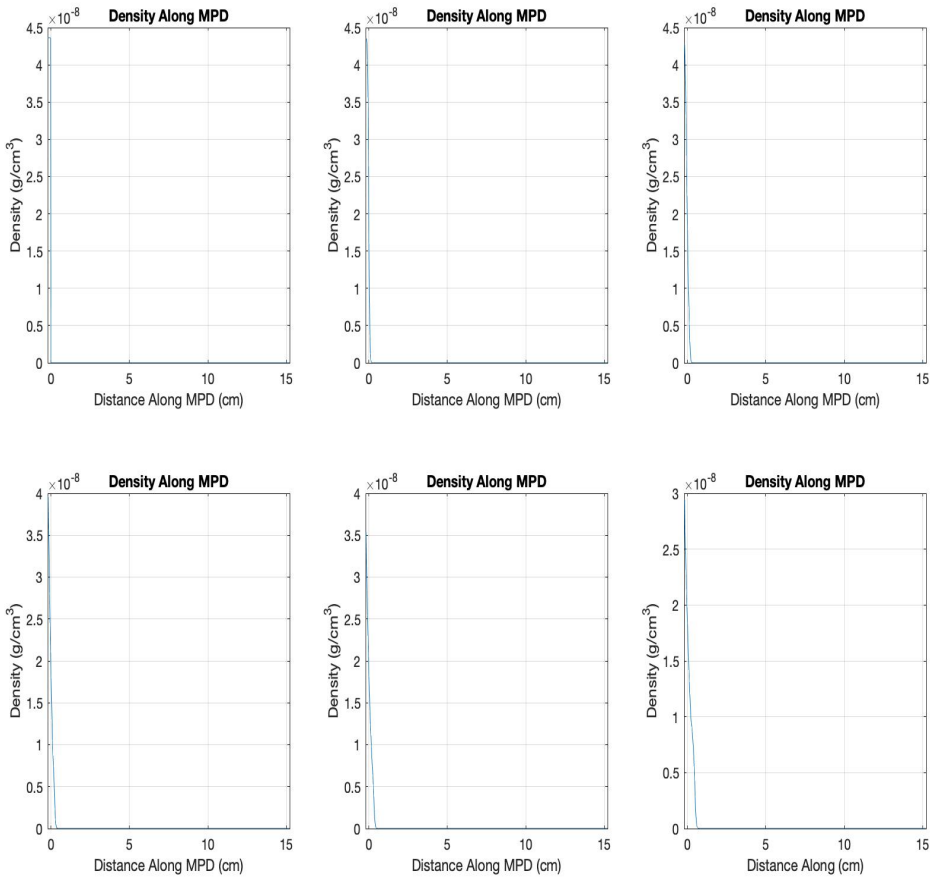

Figure 64: Evolution of the plasma density for J = 3000A and vacuum density 10^{-5} that of the plasma density. The upper left figure is at the initial time of $t = 0s$, the upper middle figure is at a time of $t = 1.2 \times 10^{-7}s$, the upper right figure is at a time of $t = 1.8 \times 10^{-7}s$, the bottom left figure is at a time of $t = 2.4 \times 10^{-7}s$, the middle left figure is at a time of $t = 3.0 \times 10^{-7}s$, and the bottom left figure is at a time of $t = 3.6 \times 10^{-7}s$.

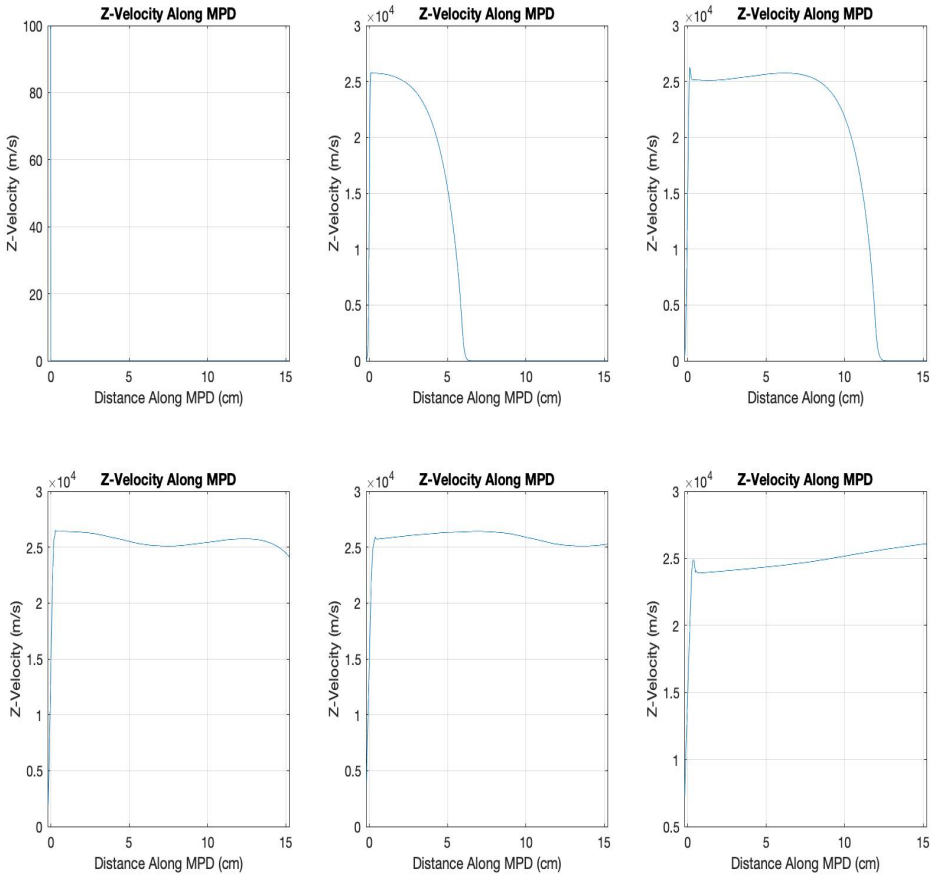

Figure 65: Evolution of the axial velocity for J = 3000A and vacuum density 10^{-5} that of the plasma density. The upper left figure is at the initial time of $t = 0s$, the upper middle figure is at a time of $t = 1.2 \times 10^{-7}s$, the upper right figure is at a time of $t = 1.8 \times 10^{-7}s$, the bottom left figure is at a time of $t = 2.4 \times 10^{-7}s$, the middle left figure is at a time of $t = 3.0 \times 10^{-7}s$, and the bottom left figure is at a time of $t = 3.6 \times 10^{-7}s$.

Figure 64 shows that the plasma expands rapidly away from the z-axis, as expected. From Figure 65 it is seen that a final velocity of $2.6 * 10^4 m/s$ is achieved at the end of the MPD channel. Once again there is a substantial acceleration, yet the final velocity is decreased when compared to the lower current cases.

Next, a current of $4000A$ is applied to the MPD thruster with a vacuum density of 10^{-5} that of the initial plasma density.

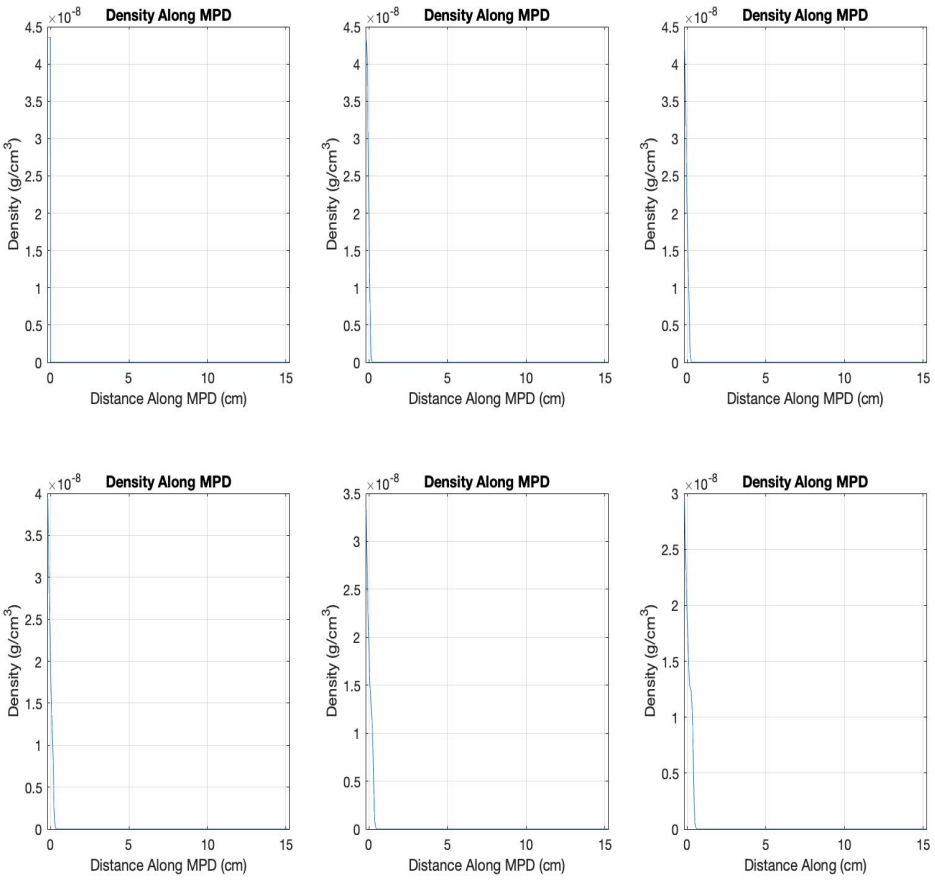

Figure 66: Evolution of the plasma density for J = $4000A$ and vacuum density 10^{-5} that of the plasma density. The upper left figure is at the initial time of $t = 0s$, the upper middle figure is at a time of $t = 1.2 \times 10^{-7}s$, the upper right figure is at a time of $t = 1.8 \times 10^{-7}s$, the bottom left figure is at a time of $t = 2.4 \times 10^{-7}s$, the middle left figure is at a time of $t = 3.0 \times 10^{-7}s$, and the bottom left figure is at a time of $t = 3.6 \times 10^{-7}s$.

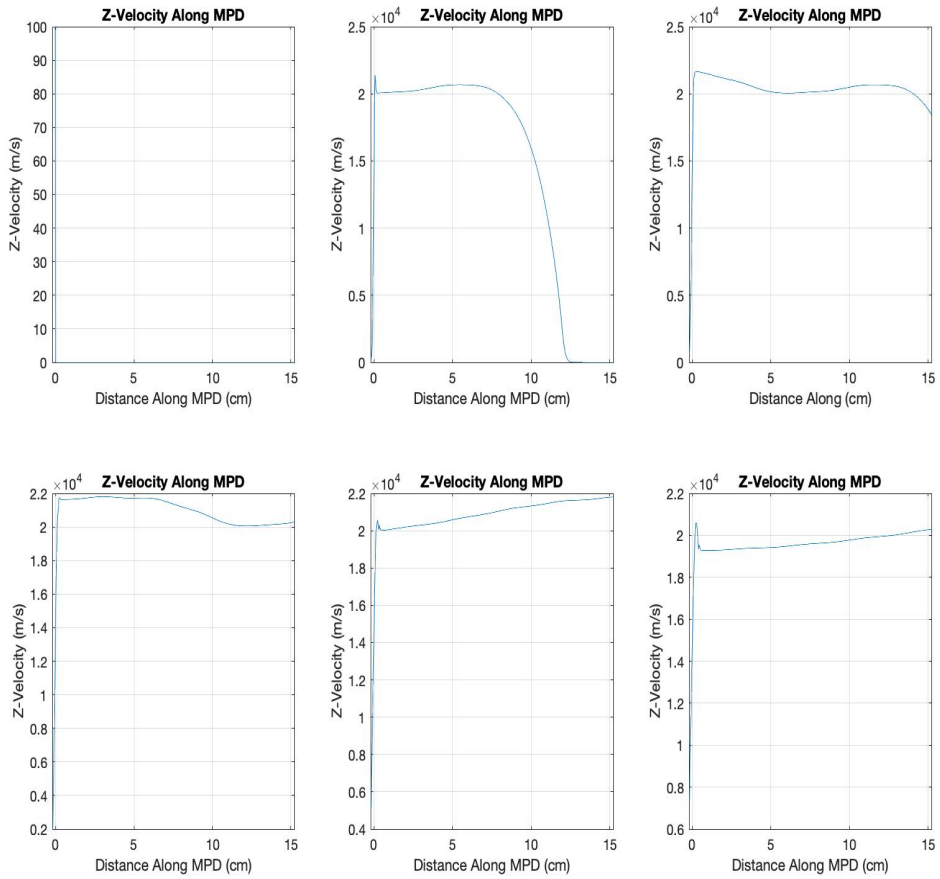

Figure 67: Evolution of the axial velocity for J = $4000A$ and vacuum density 10^{-5} that of the plasma density. The upper left figure is at the initial time of $t = 0s$, the upper middle figure is at a time of $t = 1.2 \times 10^{-7}s$, the upper right figure is at a time of $t = 1.8 \times 10^{-7}s$, the bottom left figure is at a time of $t = 2.4 \times 10^{-7}s$, the middle left figure is at a time of $t = 3.0 \times 10^{-7}s$, and the bottom left figure is at a time of $t = 3.6 \times 10^{-7}s$.

Figure 66 shows the plasma expands rapidly away from the z-axis at a similar rate to that of the $3000A$ case. In Figure 67 a final velocity of $2.01 * 10^4 m/s$ is achieved at the end of the MPD channel. Once again there is a substantial acceleration, yet the final velocity is decreased from the lower current cases. This observation is predicted

if the dominant acceleration mechanism is hydrodynamic expansion and acceleration, as previously described.

A.2.3 Additional Applied Magnetic Field Studies

We will examine the effect of an applied $10mT$ field on the MPD with a $2000A$ current.

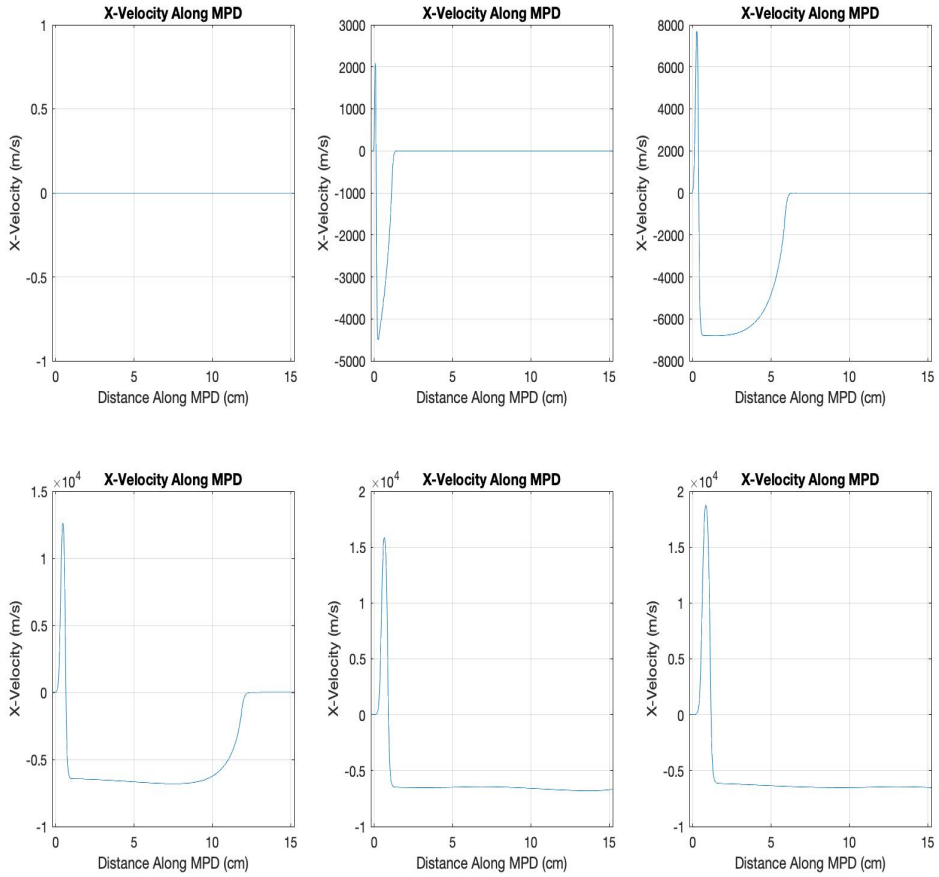

Figure 68: Evolution of the X velocity for J = $2000A$, $B_{app} = 10mT$, and vacuum density 10^{-5} that of the plasma density. The upper left figure is at the initial time of $t = 0s$, the upper middle figure is at a time of $t = 1.2 \times 10^{-7}s$, the upper right figure is at a time of $t = 1.8 \times 10^{-7}s$, the bottom left figure is at a time of $t = 2.4 \times 10^{-7}s$, the middle left figure is at a time of $t = 3.0 \times 10^{-7}s$, and the bottom left figure is at a time of $t = 3.6 \times 10^{-7}s$.

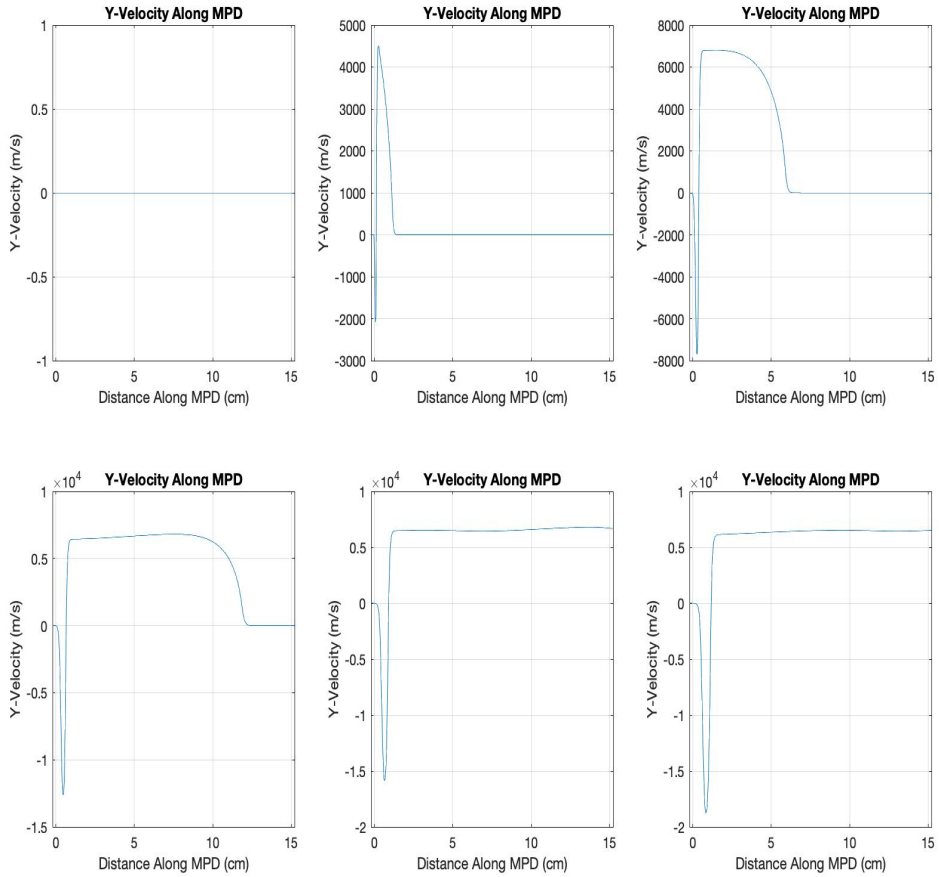

Figure 69: Evolution of the Y velocity for J = $2000A$, $B_{app} = 10mT$, and vacuum density 10^{-5} that of the plasma density. The upper left figure is at the initial time of $t = 0s$, the upper middle figure is at a time of $t = 1.2 \times 10^{-7}s$, the upper right figure is at a time of $t = 1.8 \times 10^{-7}s$, the bottom left figure is at a time of $t = 2.4 \times 10^{-7}s$, the middle left figure is at a time of $t = 3.0 \times 10^{-7}s$, and the bottom left figure is at a time of $t = 3.6 \times 10^{-7}s$.

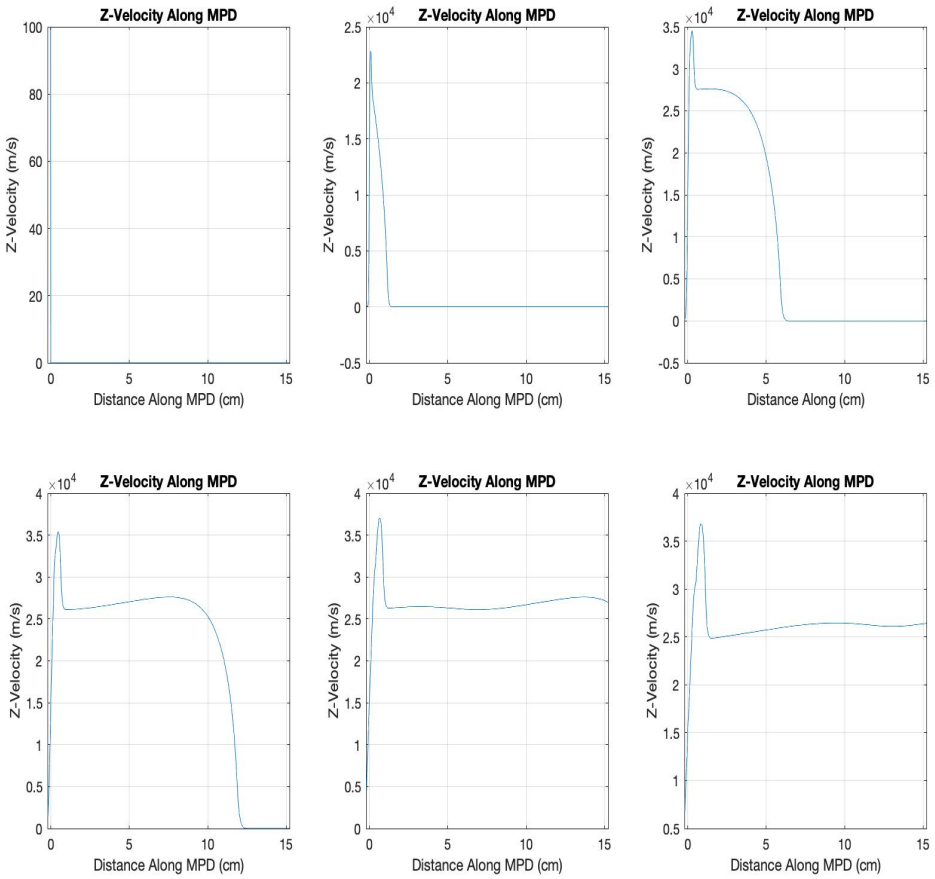

Figure 70: Evolution of the Z velocity for J = $2000A$, $B_{app} = 10mT$, and vacuum density 10^{-5} that of the plasma density. The upper left figure is at the initial time of $t = 0s$, the upper middle figure is at a time of $t = 1.2 \times 10^{-7}s$, the upper right figure is at a time of $t = 1.8 \times 10^{-7}s$, the bottom left figure is at a time of $t = 2.4 \times 10^{-7}s$, the middle left figure is at a time of $t = 3.0 \times 10^{-7}s$, and the bottom left figure is at a time of $t = 3.6 \times 10^{-7}s$.

Figures 68 and 69 show the X and Y axis velocity evolution of the plasma column along the thruster axis. Just as in the previous case, the swirling motion is observed in the mirrored X and Y velocities. Here the magnitude of the X and Y velocities is still high, but lower than previously. This is reflected in Figure 70 which shows the Z

velocity along the MPD column. The Z velocity still exhibits a high final velocity of $26km/s$, but since the plasma column was accelerated out of the thruster in a shorter amount of time than in the $1000A$ case without an applied field, there was less time within the plasma column to transfer energy to the swirling motion.

Now, let's examine the effect of an applied field of $20mT$ on the MPD with a current of $1000A$.

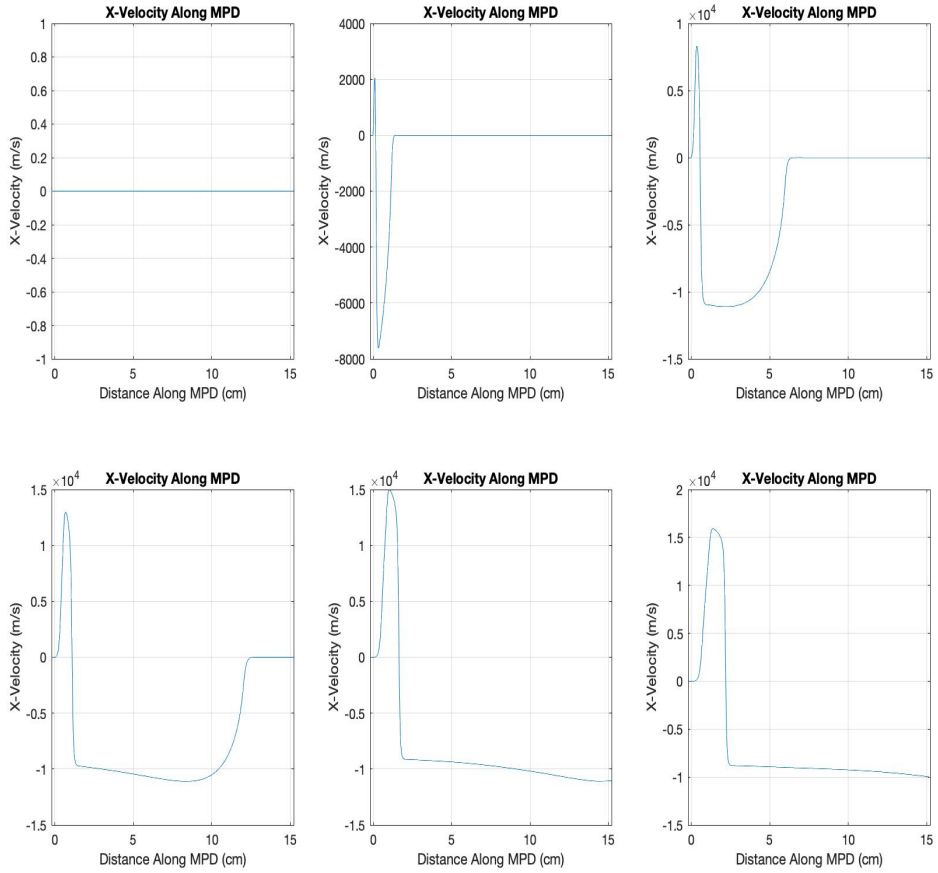

Figure 71: Evolution of the X velocity for J = $1000A$, $B_{app} = 20mT$, and vacuum density 10^{-5} that of the plasma density. The upper left figure is at the initial time of $t = 0s$, the upper middle figure is at a time of $t = 1.2 \times 10^{-7}s$, the upper right figure is at a time of $t = 1.8 \times 10^{-7}s$, the bottom left figure is at a time of $t = 2.4 \times 10^{-7}s$, the middle left figure is at a time of $t = 3.0 \times 10^{-7}s$, and the bottom left figure is at a time of $t = 3.6 \times 10^{-7}s$.

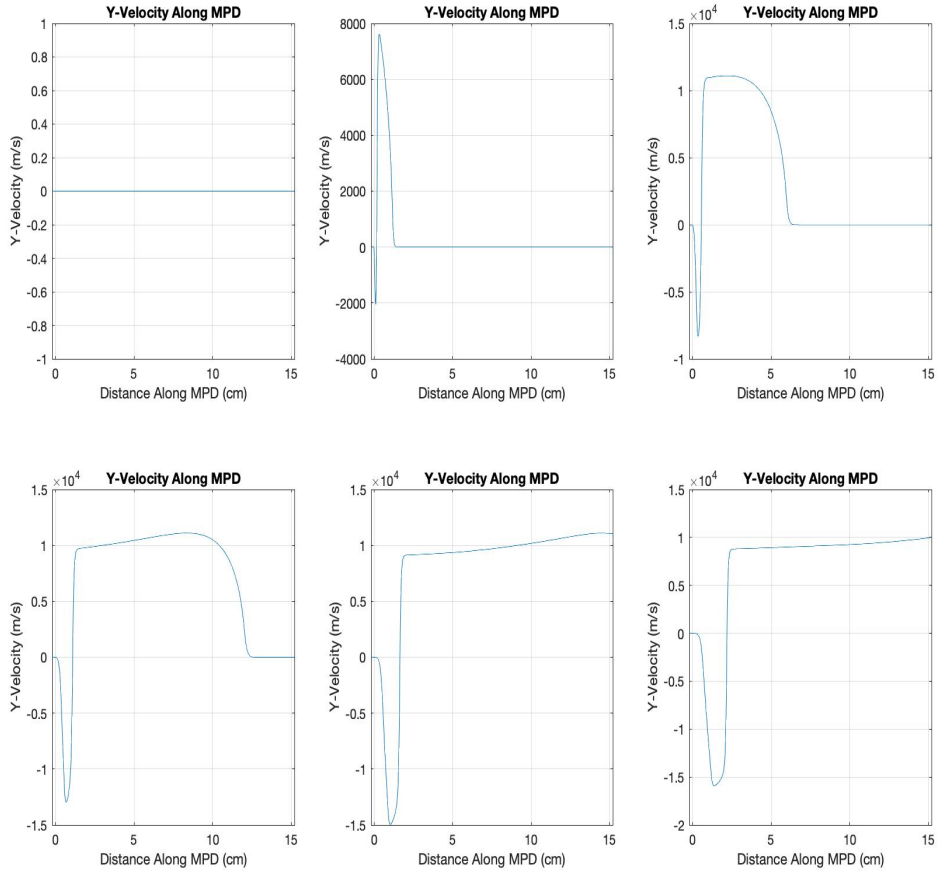

Figure 72: Evolution of the Y Velocity for J = $1000A$, $B_{app} = 20mT$, and vacuum density 10^{-5} that of the plasma density. The upper left figure is at the initial time of $t = 0s$, the upper middle figure is at a time of $t = 1.2 \times 10^{-7}s$, the upper right figure is at a time of $t = 1.8 \times 10^{-7}s$, the bottom left figure is at a time of $t = 2.4 \times 10^{-7}s$, the middle left figure is at a time of $t = 3.0 \times 10^{-7}s$, and the bottom left figure is at a time of $t = 3.6 \times 10^{-7}s$.

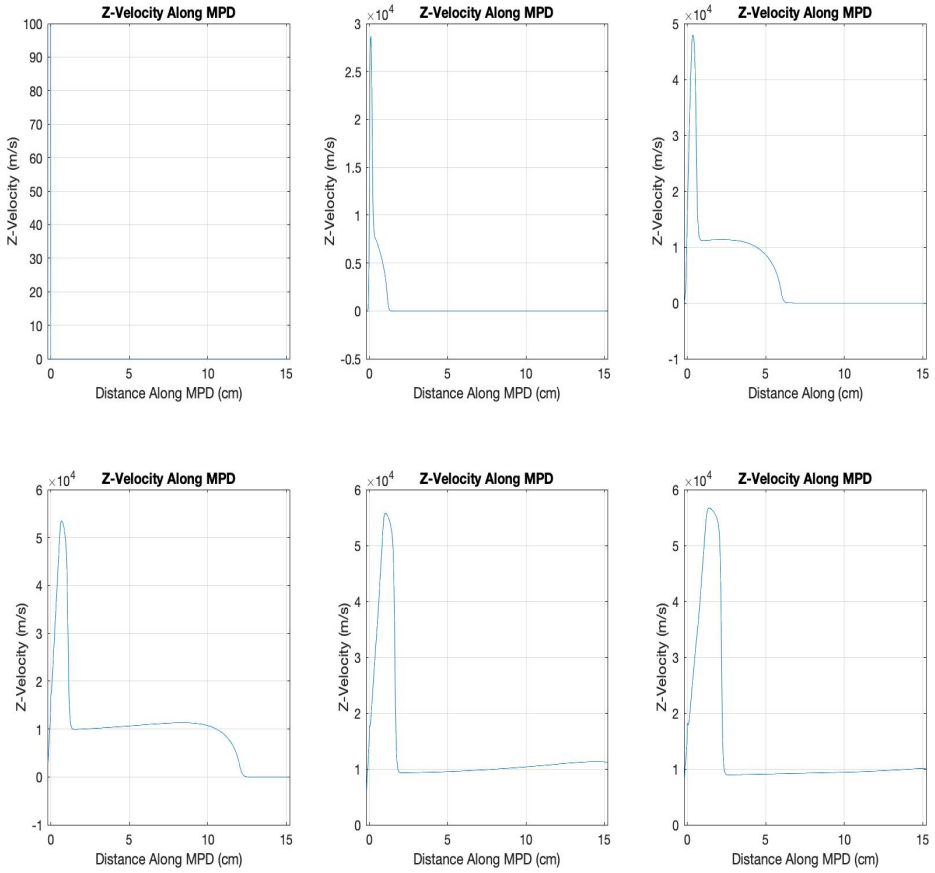

Figure 73: Evolution of the Z velocity for J = $1000A$, $B_{app} = 20mT$, and vacuum density 10^{-5} that of the plasma density. The upper left figure is at the initial time of $t = 0s$, the upper middle figure is at a time of $t = 1.2 \times 10^{-7}s$, the upper right figure is at a time of $t = 1.8 \times 10^{-7}s$, the bottom left figure is at a time of $t = 2.4 \times 10^{-7}s$, the middle left figure is at a time of $t = 3.0 \times 10^{-7}s$, and the bottom left figure is at a time of $t = 3.6 \times 10^{-7}s$.

Figures 71 and 72 show the X and Y axis velocity evolution of the plasma column along the thruster axis. As expected they mirror one another, indicating a swirling motion. Figure 73 shows the evolution of the Z velocity along the thruster chamber. The initial acceleration gained by the plasma is high, however the final velocity is lower

than in the previous case. This is caused by the increase in the applied magnetic field. As demonstrated in equation (16), the angular velocity of the swirling plasma column is directly proportional to the applied magnetic field strength; therefore increasing the applied magnetic field, will increase the swirling motion and take more energy away from the axial motion.

It is important to note that if the applied magnetic field is too strong, too much energy will be taken from the axial motion and the plasma will become trapped in the thruster chamber. This demonstrated by comparing the MPD thrusters with $1000A$ and $4000A$, both with applied magnetic field of $30mT$.

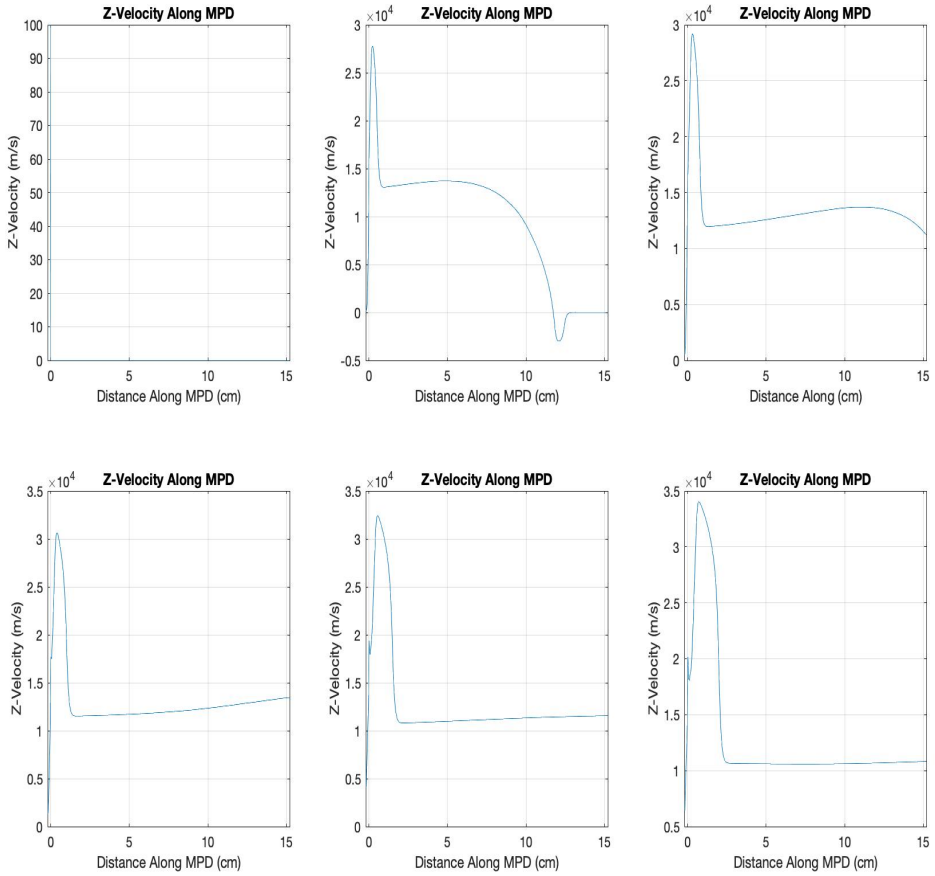

Figure 74: Evolution of the Z velocity for J = 4000A with $B_{app} = 30mT$ and vacuum density 10^{-5} that of the plasma density. The upper left figure is at the initial time of $t = 0s$, the upper middle figure is at a time of $t = 1.2 \times 10^{-7}s$, the upper right figure is at a time of $t = 1.8 \times 10^{-7}s$, the bottom left figure is at a time of $t = 2.4 \times 10^{-7}s$, the middle left figure is at a time of $t = 3.0 \times 10^{-7}s$, and the bottom left figure is at a time of $t = 3.6 \times 10^{-7}s$.

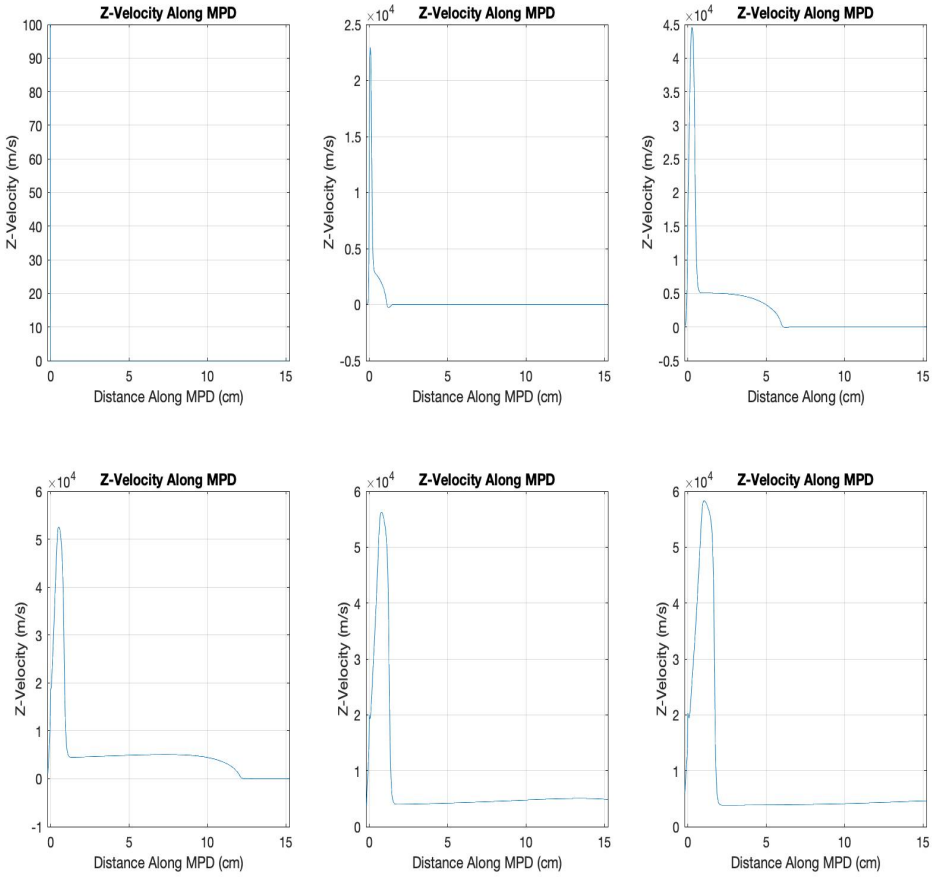

Figure 75: Evolution of the Z velocity for J = $1000A$ with $B_{app} = 30mT$ and vacuum density 10^{-5} that of the plasma density. The upper left figure is at the initial time of $t = 0s$, the upper middle figure is at a time of $t = 1.2 \times 10^{-7}s$, the upper right figure is at a time of $t = 1.8 \times 10^{-7}s$, the bottom left figure is at a time of $t = 2.4 \times 10^{-7}s$, the middle left figure is at a time of $t = 3.0 \times 10^{-7}s$, and the bottom left figure is at a time of $t = 3.6 \times 10^{-7}s$.

By comparing Figures 74 and 75, the $4000A$ MPD achieves a higher velocity at the end of the MPD thrust chamber when contrasted with the $1000A$ MPD. This can be explained by the previously described effect of hydrodynamic expansion and acceleration. Since the $4000A$ MPD applies a higher energy to the plasma particles,

with no magnetic field, the plasma is accelerated out of the chamber before it could experience the full hydrodynamic effects. Since the applied magnetic field transfers energy from the axial motion to azimuthal motion, the plasma now has more time to spend in the chamber. This results in the $4000A$ current applying a greater force to the plasma over the chamber length, giving the plasma a greater final velocity. The final velocity of the $1000A$ MPD is lower and therefore the plasma is closer to being trapped inside the chamber. When a solenoidal magnetic field is applied to the MPD thruster, it must be balanced with the current in order to prevent trapping. If the applied magnetic field is too great, there will be too much axial energy transferred to the swirling motion and the plasma column will begin to travel back into the MPD chamber and become trapped inside the thruster.

A.2.4 Additional Number Density Studies

Let us examine the same MPD but with an applied magnetic field of $20mT$.

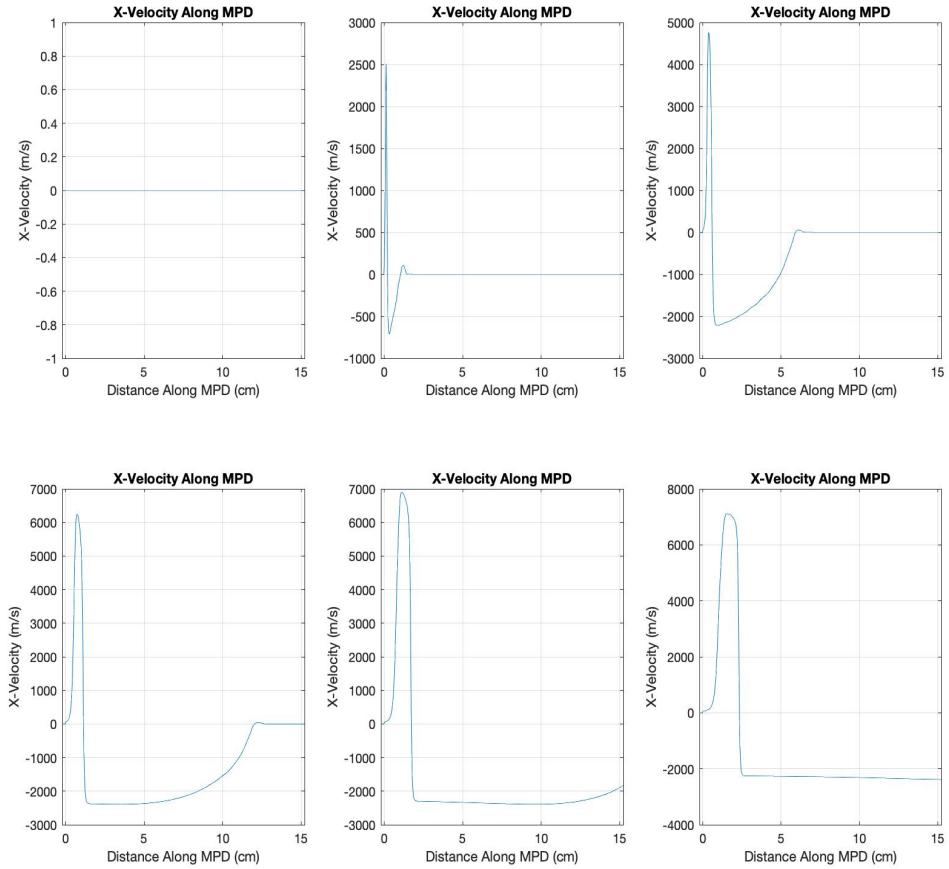

Figure 76: Evolution of the X velocity for J = $1000A$ with $n = 2 \times 10^{21} m^{-3}$, $B_{app} = 20mT$, and vacuum density 10^{-5} that of the plasma density. The upper left figure is at the initial time of $t = 0s$, the upper middle figure is at a time of $t = 1.2 \times 10^{-7}s$, the upper right figure is at a time of $t = 1.8 \times 10^{-7}s$, the bottom left figure is at a time of $t = 2.4 \times 10^{-7}s$, the middle left figure is at a time of $t = 3.0 \times 10^{-7}s$, and the bottom left figure is at a time of $t = 3.6 \times 10^{-7}s$.

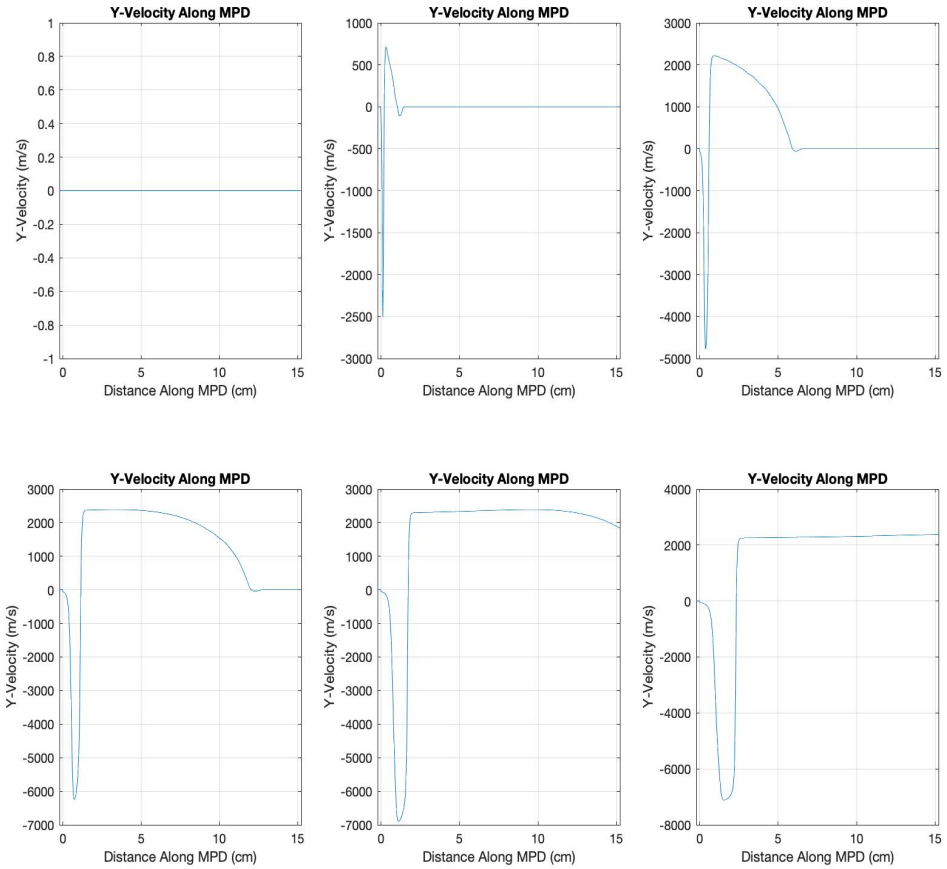

Figure 77: Evolution of the Y velocity for J = $1000A$ with $n = 2 \times 10^{21} m^{-3}$, $B_{app} = 20mT$, and vacuum density 10^{-5} that of the plasma density. The upper left figure is at the initial time of $t = 0s$, the upper middle figure is at a time of $t = 1.2 \times 10^{-7}s$, the upper right figure is at a time of $t = 1.8 \times 10^{-7}s$, the bottom left figure is at a time of $t = 2.4 \times 10^{-7}s$, the middle left figure is at a time of $t = 3.0 \times 10^{-7}s$, and the bottom left figure is at a time of $t = 3.6 \times 10^{-7}s$.

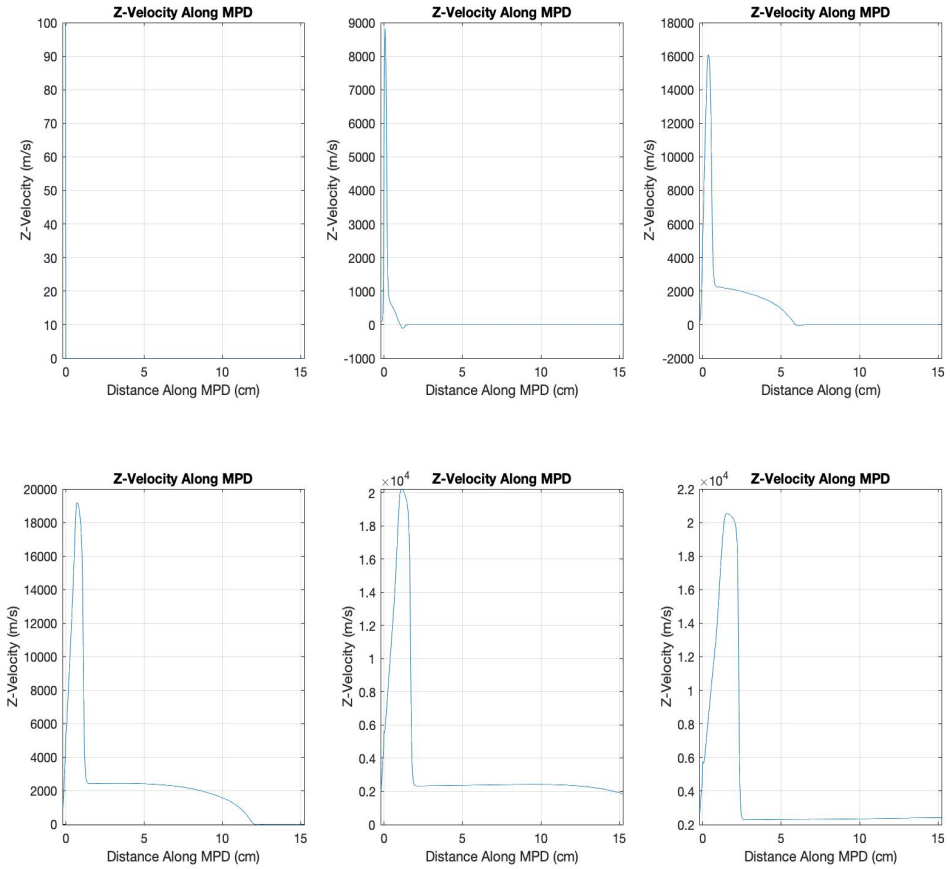

Figure 78: Evolution of the Z velocity for J = $1000A$ with $n = 2 \times 10^{21} m^{-3}$, $B_{app} = 20mT$, and vacuum density 10^{-5} that of the plasma density. The upper left figure is at the initial time of $t = 0s$, the upper middle figure is at a time of $t = 1.2 \times 10^{-7}s$, the upper right figure is at a time of $t = 1.8 \times 10^{-7}s$, the bottom left figure is at a time of $t = 2.4 \times 10^{-7}s$, the middle left figure is at a time of $t = 3.0 \times 10^{-7}s$, and the bottom left figure is at a time of $t = 3.6 \times 10^{-7}s$.

Figures 76 and 77 show the evolution of the X and Y velocities along the MPD channel. The swirling effect is observed from the mirroring of the X and Y velocities, but the velocities achieved are much smaller in comparison with the $n = 2 \times 10^{20} m^{-3}$ case. This is explained from examination of Figure 78 which demonstrates the evo-

lution of the Z velocity along the MPD channel. Figure 78 shows that the Z velocity achieves a much smaller initial acceleration along the channel giving the plasma more time to spend in the chamber and therefore more energy is transferred to the swirling motion. It also shows that the final velocity along the Z axis is much smaller than when compared with the $n = 2 \times 10^{20} m^{-3}$ case. With a higher number density the plasma comes closer to becoming trapped in the chamber with a lower applied current. Again this can be investigated from analyzing the MPD with an applied current of $4000A$ and the same applied magnetic field.

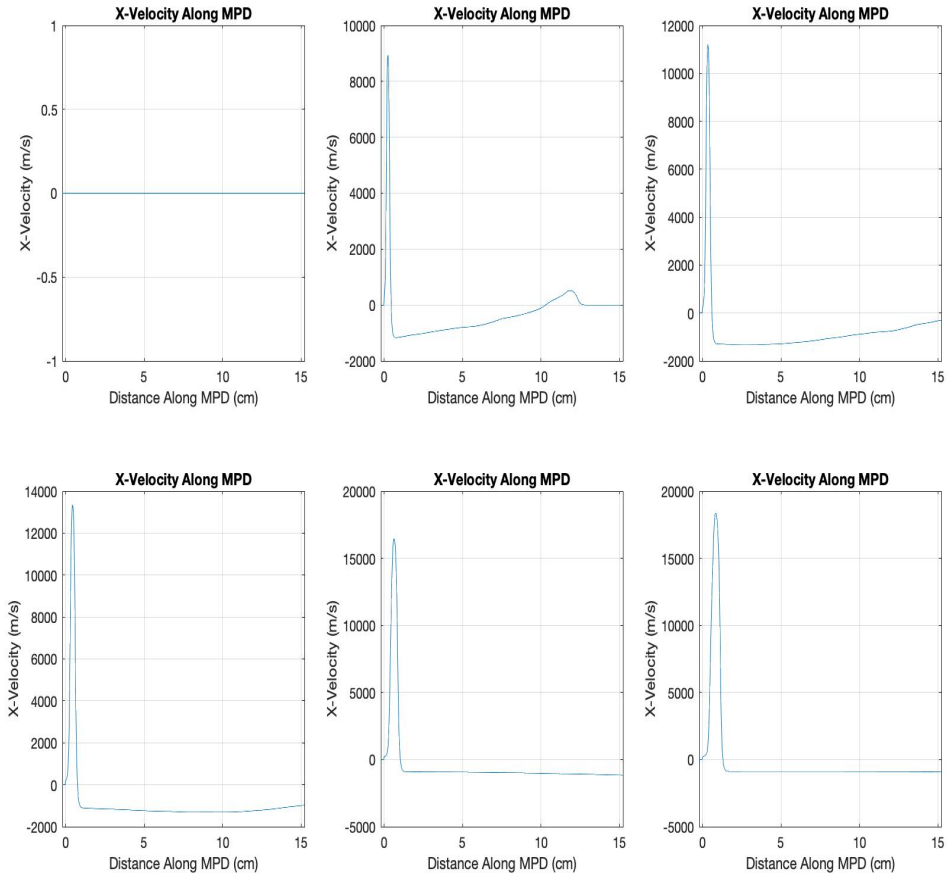

Figure 79: Evolution of the X velocity for J = 4000A with $n = 2 \times 10^{21} m^{-3}$, $B_{app} = 20mT$, and vacuum density 10^{-5} that of the plasma density. The upper left figure is at the initial time of $t = 0s$, the upper middle figure is at a time of $t = 1.2 \times 10^{-7}s$, the upper right figure is at a time of $t = 1.8 \times 10^{-7}s$, the bottom left figure is at a time of $t = 2.4 \times 10^{-7}s$, the middle left figure is at a time of $t = 3.0 \times 10^{-7}s$, and the bottom left figure is at a time of $t = 3.6 \times 10^{-7}s$.

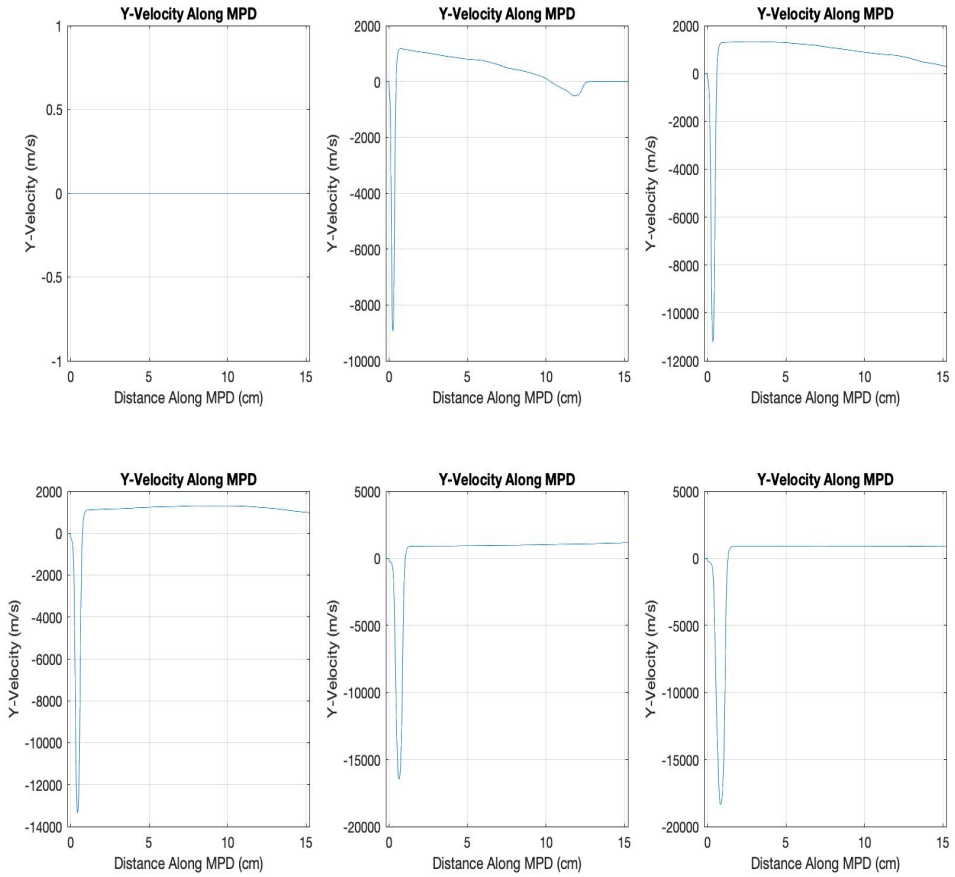

Figure 80: Evolution of the Y velocity for J = $4000A$ with $n = 2 \times 10^{21} m^{-3}$, $B_{app} = 20mT$, and vacuum density 10^{-5} that of the plasma density. The upper left figure is at the initial time of $t = 0s$, the upper middle figure is at a time of $t = 1.2 \times 10^{-7}s$, the upper right figure is at a time of $t = 1.8 \times 10^{-7}s$, the bottom left figure is at a time of $t = 2.4 \times 10^{-7}s$, the middle left figure is at a time of $t = 3.0 \times 10^{-7}s$, and the bottom left figure is at a time of $t = 3.6 \times 10^{-7}s$.

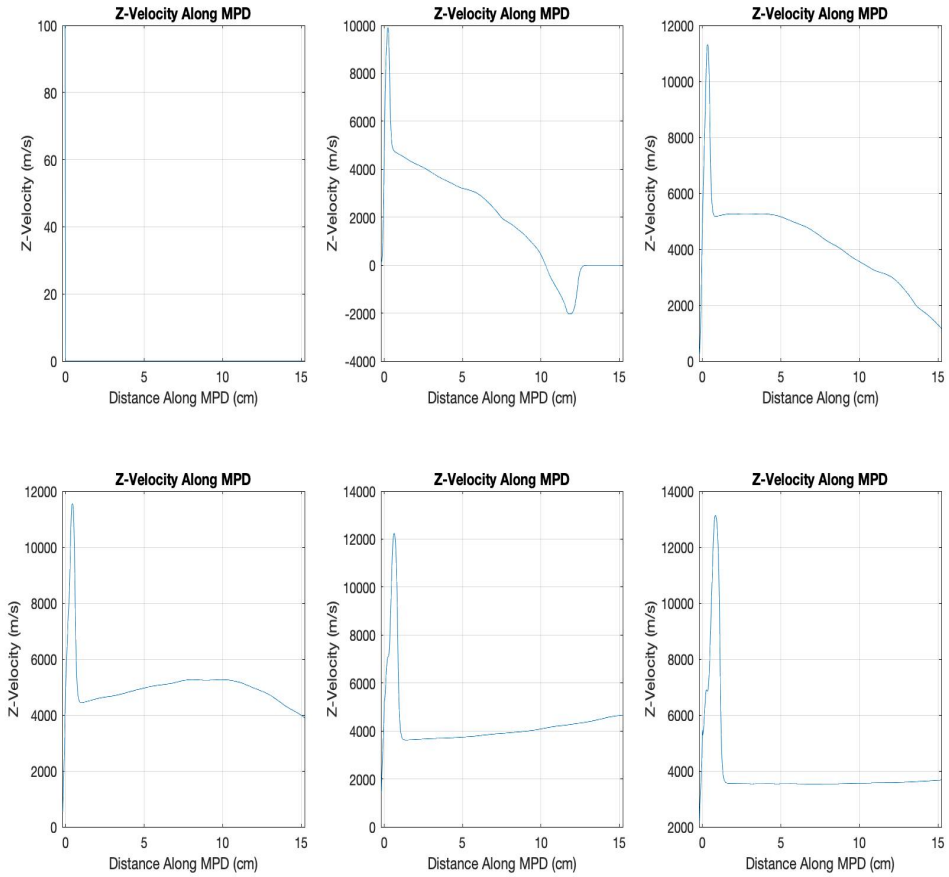

Figure 81: Evolution of the Z Velocity for J = $4000A$ with $n = 2 \times 10^{21} m^{-3}$, $B_{app} = 20mT$, and vacuum density 10^{-5} that of the plasma density. The upper left figure is at the initial time of $t = 0s$, the upper middle figure is at a time of $t = 1.2 \times 10^{-7}s$, the upper right figure is at a time of $t = 1.8 \times 10^{-7}s$, the bottom left figure is at a time of $t = 2.4 \times 10^{-7}s$, the middle left figure is at a time of $t = 3.0 \times 10^{-7}s$, and the bottom left figure is at a time of $t = 3.6 \times 10^{-7}s$.

Figures 79 and 80 again show the evolution of the X and Y velocities along the MPD channel and exhibit the swirling motion. The final velocity achieved in these directions is lower than in the case with $n = 2 * 10^{20} m^{-3}$. Figure 81 shows that the Z velocity along the MPD channel is larger than in the $1000A$ case. This is again

due to the fact that the higher current imparts more energy into the plasma column, giving it a higher final Z velocity. It is worth noting that the decrease in the X and Y velocity can be explained by the fact that the more energy the plasma column obtains from the applied current, the faster it is accelerated out of the MPD channel giving it less time to impart energy to the swirling motion. These velocities are much lower than the $n = 2 \times 10^{20} m^{-3}$ case due to the increased self interaction and therefore increased resistivity in the chamber.

Next let us examine what happens when the number density is increased to $n = 2 \times 10^{22} m^{-3}$ ($n = 2 \times 10^{16} cm^{-3}$).

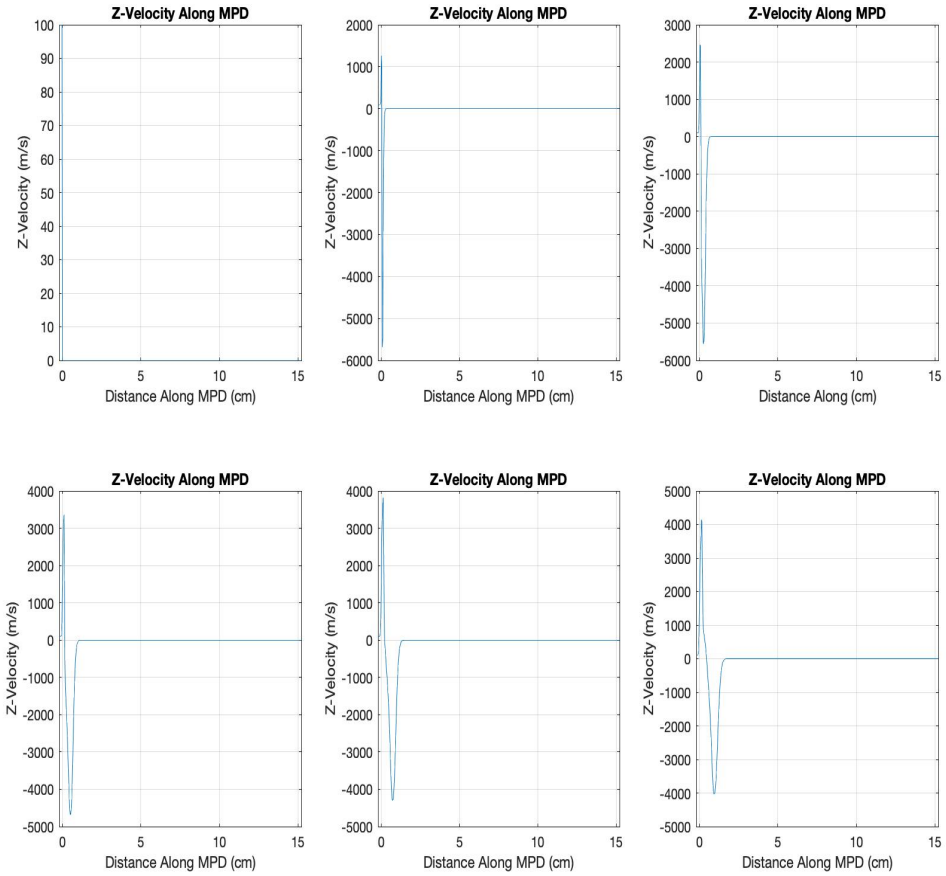

Figure 82: Evolution of the Z Velocity for J = $1000A$ with $n = 2 * 10^{22} m^{-3}$ and vacuum density 10^{-5} that of the plasma density. The upper left figure is at the initial time of $t = 0s$, the upper middle figure is at a time of $t = 1.2 \times 10^{-7} s$, the upper right figure is at a time of $t = 1.8 \times 10^{-7} s$, the bottom left figure is at a time of $t = 2.4 \times 10^{-7} s$, the middle left figure is at a time of $t = 3.0 \times 10^{-7} s$, and the bottom left figure is at a time of $t = 3.6 \times 10^{-7} s$.

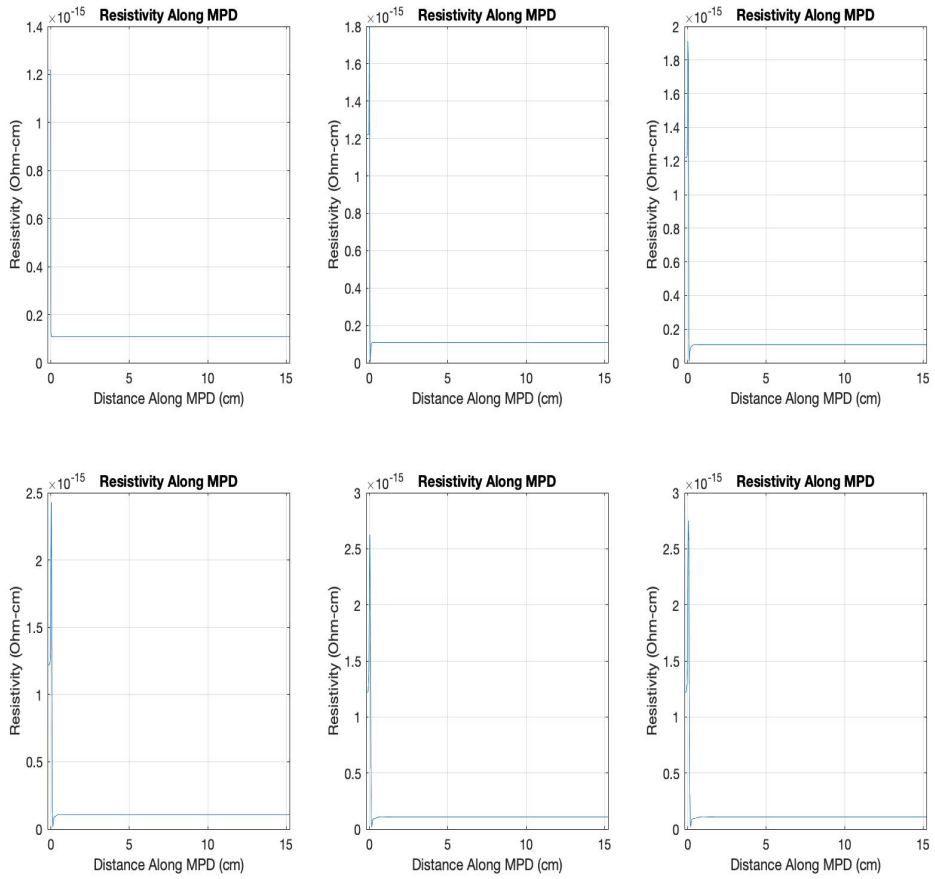

Figure 83: Evolution of the plasma resistivity for J = $1000A$ with $n = 2 * 10^{22} m^{-3}$ and vacuum density 10^{-5} that of the plasma density. The upper left figure is at the initial time of $t = 0s$, the upper middle figure is at a time of $t = 1.2 \times 10^{-7} s$, the upper right figure is at a time of $t = 1.8 \times 10^{-7} s$, the bottom left figure is at a time of $t = 2.4 \times 10^{-7} s$, the middle left figure is at a time of $t = 3.0 \times 10^{-7} s$, and the bottom left figure is at a time of $t = 3.6 \times 10^{-7} s$.

Figure 83 shows the evolution of the resistivity along the MPD channel. The resistivity reaches another order of magnitude higher than in the previous case. The effect of this is shown in Figure 82 where the higher resistivity causes the plasma column to become trapped in the MPD chamber. This is seen in Figure 82 as the z

velocity initially reaches a high value, but quickly accelerates backward in the channel; thus, creating a trapping scenario and increasing the resistivity and self interactions at the channel inlet, further increasing the trapping effect.

Next, let us examine the same MPD but with an applied magnetic field of $20mT$.

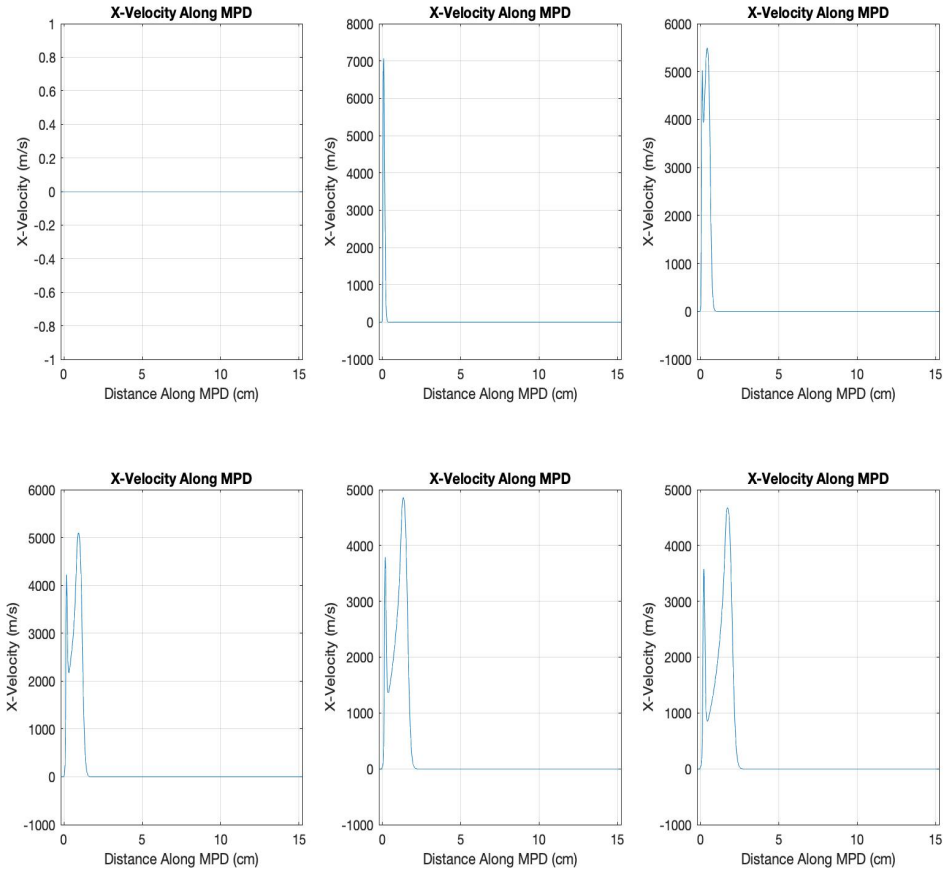

Figure 84: Evolution of the X velocity for J = $1000A$ with $n = 2 \times 10^{22} m^{-3}$, $B_{app} = 20mT$, and vacuum density 10^{-5} that of the plasma density. The upper left figure is at the initial time of $t = 0s$, the upper middle figure is at a time of $t = 1.2 \times 10^{-7}s$, the upper right figure is at a time of $t = 1.8 \times 10^{-7}s$, the bottom left figure is at a time of $t = 2.4 \times 10^{-7}s$, the middle left figure is at a time of $t = 3.0 \times 10^{-7}s$, and the bottom left figure is at a time of $t = 3.6 \times 10^{-7}s$.

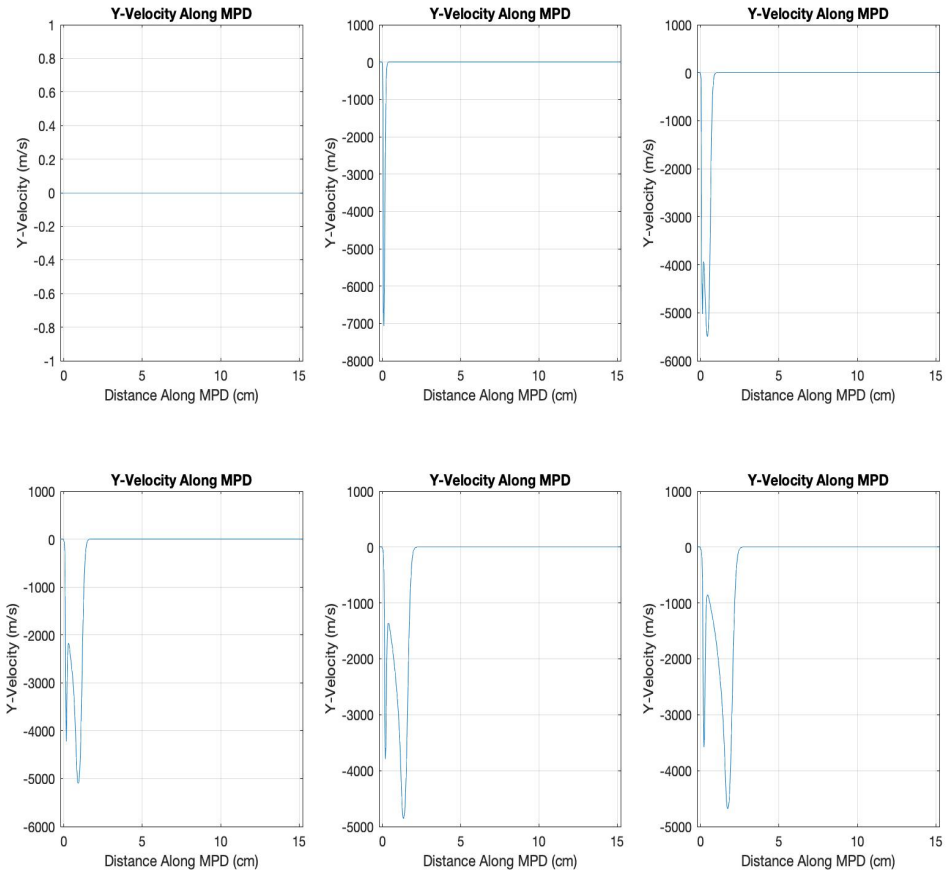

Figure 85: Evolution of the Y velocity for J = $1000A$ with $n = 2 \times 10^{22} m^{-3}$, $B_{app} = 20mT$, and vacuum density 10^{-5} that of the plasma density. The upper left figure is at the initial time of $t = 0s$, the upper middle figure is at a time of $t = 1.2 \times 10^{-7}s$, the upper right figure is at a time of $t = 1.8 \times 10^{-7}s$, the bottom left figure is at a time of $t = 2.4 \times 10^{-7}s$, the middle left figure is at a time of $t = 3.0 \times 10^{-7}s$, and the bottom left figure is at a time of $t = 3.6 \times 10^{-7}s$.

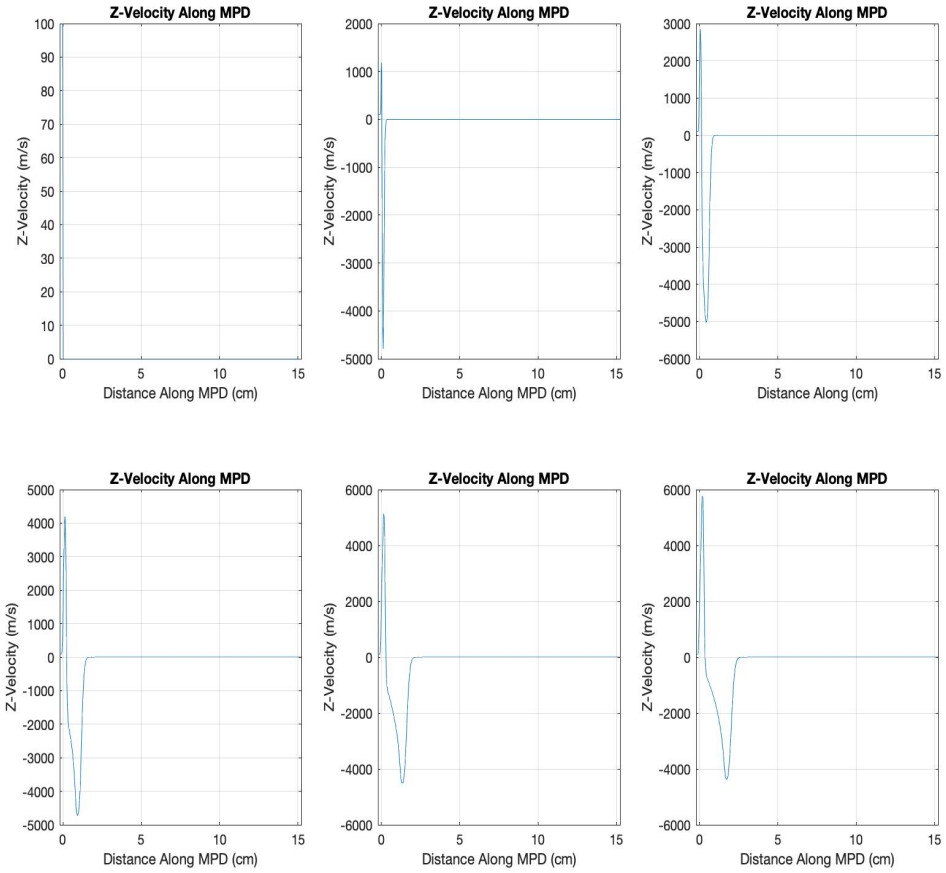

Figure 86: Evolution of the Z velocity for J = $1000A$ with $n = 2 \times 10^{22} m^{-3}$, $B_{app} = 20mT$, and vacuum density 10^{-5} that of the plasma density. The upper left figure is at the initial time of $t = 0s$, the upper middle figure is at a time of $t = 1.2 \times 10^{-7}s$, the upper right figure is at a time of $t = 1.8 \times 10^{-7}s$, the bottom left figure is at a time of $t = 2.4 \times 10^{-7}s$, the middle left figure is at a time of $t = 3.0 \times 10^{-7}s$, and the bottom left figure is at a time of $t = 3.6 \times 10^{-7}s$.

Figures 84 and 85 show the evolution of X and Y velocities along the MPD channel. Again the swirling motion is shown by the mirroring of the X and Y velocities, but it is worth noting the formation of the double humped curve in the X and Y velocities. This is caused by the trapping of the plasma in the chamber as shown in Figure

86. The trapping causes the plasma to reverse back into the MPD chamber resulting in more energy being transfered to the swirling motion forming the double humped curve. This further increases the number of self interactions which traps the plasma. This trapping is also observed in the $4000A$ case with no applied magnetic field and the $20mT$ applied magnetic field.

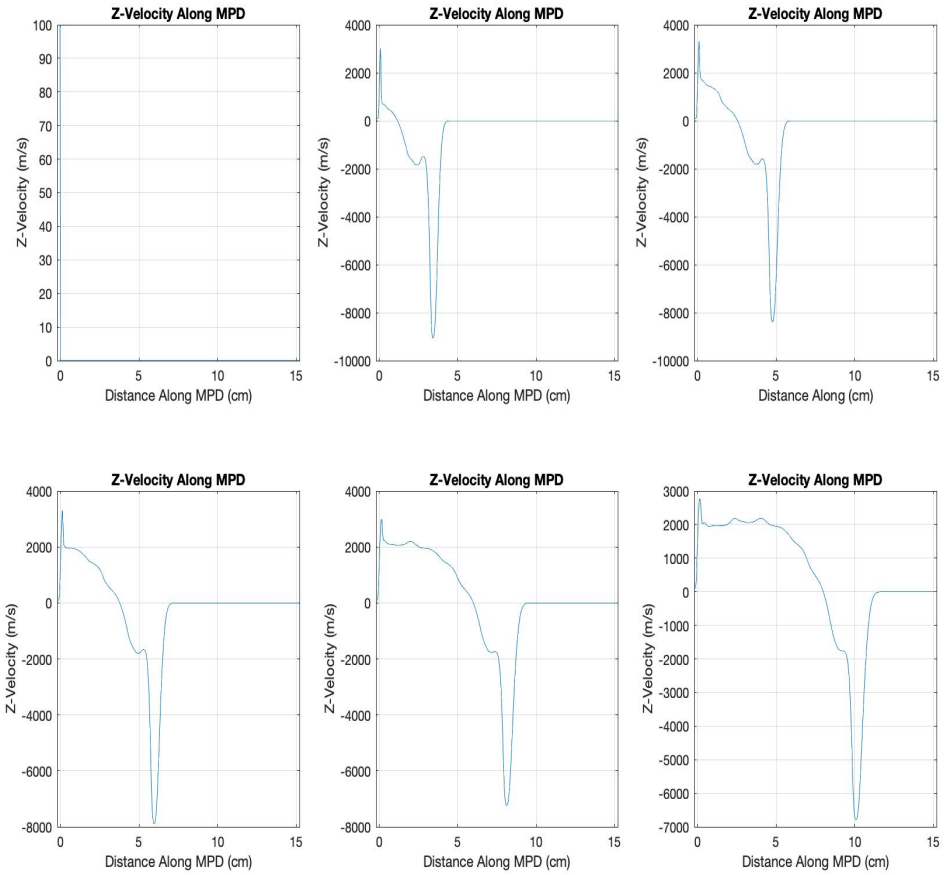

Figure 87: Evolution of the Z velocity for J = $4000A$ with $n = 2 \times 10^{22} m^{-3}$ and vacuum density 10^{-5} that of the plasma density. The upper left figure is at the initial time of $t = 0s$, the upper middle figure is at a time of $t = 1.2 \times 10^{-7}s$, the upper right figure is at a time of $t = 1.8 \times 10^{-7}s$, the bottom left figure is at a time of $t = 2.4 \times 10^{-7}s$, the middle left figure is at a time of $t = 3.0 \times 10^{-7}s$, and the bottom left figure is at a time of $t = 3.6 \times 10^{-7}s$.

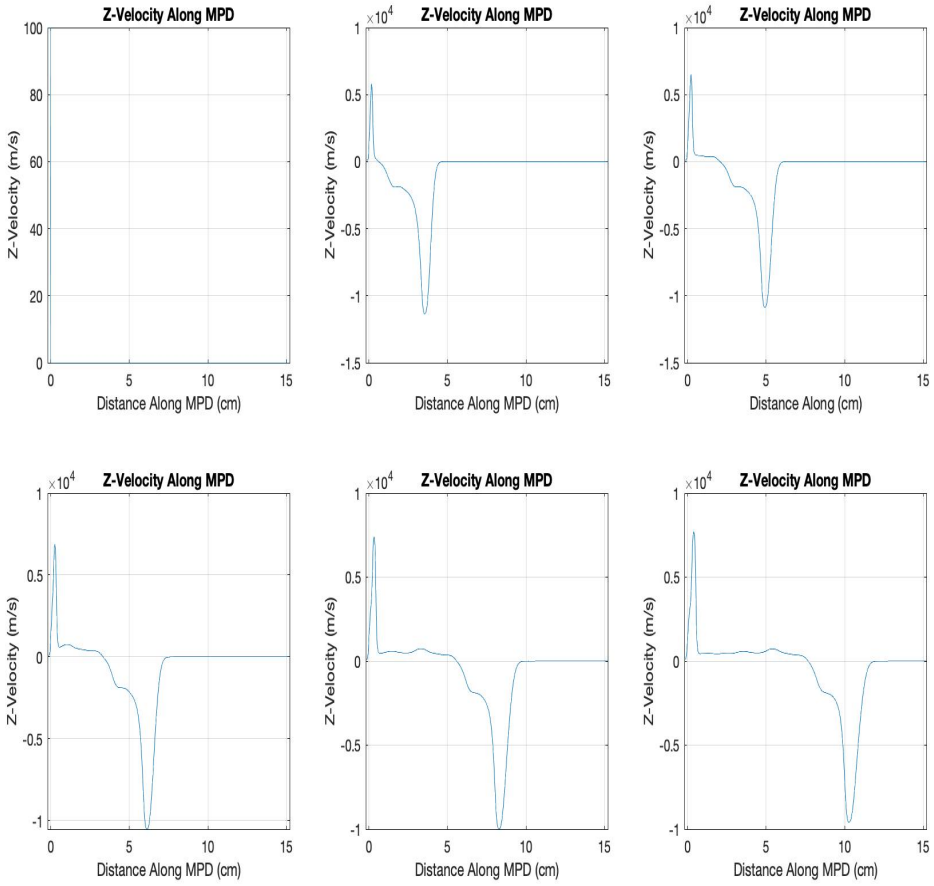

Figure 88: Evolution of the Z velocity for J = $4000A$ with $n = 2 \times 10^{22} m^{-3}$, $B_{app} = 20mT$, and vacuum density 10^{-5} that of the plasma density. The upper left figure is at the initial time of $t = 0s$, the upper middle figure is at a time of $t = 1.2 \times 10^{-7}s$, the upper right figure is at a time of $t = 1.8 \times 10^{-7}s$, the bottom left figure is at a time of $t = 2.4 \times 10^{-7}s$, the middle left figure is at a time of $t = 3.0 \times 10^{-7}s$, and the bottom left figure is at a time of $t = 3.6 \times 10^{-7}s$.

Figures 87 and 88 demonstrate the evolution of the Z velocity along the MPD channel for both cases. It is understood from these figures that the trapping of the plasma column is still observed, but the plasma is able to retain a positive velocity for a longer distance in the chamber due to the increased current. In order to accelerate

a plasma of a high number density, a much higher current is required to accelerate the plasma out of the chamber. The achieved velocities in the Z direction are much smaller than in the previous cases due to the increased number of self interactions in the plasma and, therefore, increased resistivity.

Bibliography

1. Scott Hsu, Jason Cassibry, and F. Douglas Witherspoon. Plasma-Jet-Driven Magneto-Inertial Fusion (PJMIF): Physics and Design for a Plasma Liner Formation Experiment. In *APS Division of Plasma Physics Meeting Abstracts*, volume 2014 of *APS Meeting Abstracts*, page JP8.089, October 2014.

2. Yong Chia Thio, Scott Hsu, F. Witherspoon, Edward Cruz, Andrew Case, Samuel Langendorf, Kevin Yates, John Dunn, Jason Cassibry, Roman Samulyak, Peter Stoltz, Samuel Brockington, Ajoke Williams, Marco Luna, Robert Becker, and Adam Cook. Plasma-jet-driven magneto-inertial fusion. *Fusion Science and Technology*, 75:1–18, 05 2019.

3. Alexander Sivkov, Yuliya Shanenkova, and Yuliya Polovinkina. Obtaining molybdenum-copper composite for effective thermal control in electronic systems. *MATEC Web of Conferences*, 141:01036, 01 2017.

4. Kenichi Kubota, Ikkoh Funaki, and Y Okuno. Numerical study on electrode model for plasma simulation of mpd thruster. 05 2021.

5. R.G. Jahn. *Physics of Electric Propulsion*. Dover Books on Physics. Dover Publications, 2012.

6. M. Coletti. Simple thrust formula for an mpd thruster with applied magnetic field from magnetic stress tensor. 07 2007.

7. Dan Lev. *Investigation of Efficiency in Applied Field MagnetoPlasmaDynamic Thrusters*. PhD thesis, 01 2012.

8. Mahdy Ahangar, Reza Ebrahimi, and Mehrzad Shams. Numerical simulation of non-equilibrium plasma flow in a cylindrical mpd thruster using a high-order flux-difference splitting method. *Acta Astronautica*, 103:129–141, 2014.

9. Peter K. Sweby. *Godunov Methods*, pages 879–898. Springer US, Boston, MA, 2001.

10. Xiaocheng Guo, Vladimir Florinski, and Chi Wang. The hlld riemann solver based on magnetic field decomposition method for the numerical simulation of magneto-hydrodynamics. *Journal of Computational Physics*, 327:543–552, 2016.

11. F.F. Chen and Plenum Publishing. *Introduction to Plasma Physics and Controlled Fusion*. Number v. 1 in Introduction to Plasma Physics and Controlled Fusion. Springer, 1984.

12. A. G. Lynn, E. Merritt, M. Gilmore, S. C. Hsu, F. D. Witherspoon, and J. T. Cassibry. Diagnostics for the plasma liner experiment. *Review of Scientific Instruments*, 81(10):10E115, 2010.

13. J. T. Cassibry, R. J. Cortez, S. C. Hsu, and F. D. Witherspoon. Estimates of confinement time and energy gain for plasma liner driven magnetoinertial fusion using an analytic self-similar converging shock model. *Physics of Plasmas*, 16(11):112707, 2009.

14. T. J. Awe, C. S. Adams, J. S. Davis, D. S. Hanna, S. C. Hsu, and J. T. Cassibry. One-dimensional radiation-hydrodynamic scaling studies of imploding spherical plasma liners. *Physics of Plasmas*, 18(7):072705, 2011.

15. A. Case, S. Messer, R. Bomgardner, and F. D. Witherspoon. Interferometer density measurements of a high-velocity plasmoid. *Physics of Plasmas*, 17(5):053503, 2010.

16. F. Douglas Witherspoon, Andrew Case, Sarah J. Messer, Richard Bomgardner, Michael W. Phillips, Samuel Brockington, and Raymond Elton. A contoured gap coaxial plasma gun with injected plasma armature. *Review of Scientific Instruments*, 80(8):083506, 2009.

17. S. Messer, A. Case, R. Bomgardner, M. Phillips, and F. D. Witherspoon. Fast pressure probe measurements of a high-velocity plasma plume. *Physics of Plasmas*, 16(6):064502, 2009.

18. E. Fischer, Z. Rozkwitalski, and F. K. Kneubühl. Self-field MPD thruster with atomic and molecular propellants. *Applied Physics B: Lasers and Optics*, 38(1):41–49, September 1985.

19. Monika Auweter-Kurtz, Cristian Coclici, Jörg Heiermann, Claus-Dieter Munz, and Christian Sleziona. Magnetoplasmadynamic rocket thruster simulation. In Heinrich Freistühler and Gerald Warnecke, editors, *Hyperbolic Problems: Theory, Numerics, Applications*, pages 99–108, Basel, 2001. Birkhäuser Basel.

20. Mariano Andrenucci. *Magnetoplasmadynamic Thrusters*. American Cancer Society, 2010.

21. R.J. Goldston. *Introduction to Plasma Physics*. CRC Press, 2020.

22. Charles Chelem Mayigué and Rodion Groll. Magneto-plasmadynamic thruster modelling with coaxial induced magnetic field. *International Journal of Computational Methods and Experimental Measurements*, 4:380–392, 11 2016.

23. Charles Chelem Mayigué and Rodion Groll. Magneto-plasmadynamic thruster modelling with coaxial induced magnetic field. *International Journal of Computational Methods and Experimental Measurements*, 4:380–392, 11 2016.

24. Hai-Bin Tang, Jiao Cheng, Chang Liu, and Thomas M. York. Study of applied magnetic field magnetoplasmadynamic thrusters with particle-in-cell and monte carlo collision. ii. investigation of acceleration mechanisms. *Physics of Plasmas*, 19(7):073108, 2012.

25. Roger M. Myers. Applied-field mpd thruster performance with hydrogen and argon propellants. *Journal of Propulsion and Power*, 9(5):781–784, 1993.

26. J. A. Bittencourt. *Plasma Conductivity and Diffusion*, pages 238–268. Springer New York, New York, NY, 2004.

27. Gordon I. Ogilvie. Astrophysical fluid dynamics. *Journal of Plasma Physics*, 82(3), May 2016.

28. T. Andreussi and F. Pegoraro. Magnetized plasma flows and magnetoplasmadynamic thrusters. *Physics of Plasmas*, 17(6):063507, 2010.

29. E. W. (Elliott Ward) Cheney. *Numerical mathematics and computing / Ward Cheney, David Kincaid.* Brooks/Cole, Belmont, CA, sixth edition. edition, 2008.

30. G. Webb and S. Anco. Conservation laws in magnetohydrodynamics and fluid dynamics: Lagrangian approach. volume 2153, page 020024, 09 2019.

31. John David Jackson. *Classical electrodynamics*. Wiley, New York, NY, 3rd ed. edition, 1999.

32. A. Dedner, F. Kemm, D. Kröner, C.-D. Munz, T. Schnitzer, and M. Wesenberg. Hyperbolic divergence cleaning for the mhd equations. *Journal of Computational Physics*, 175(2):645–673, 2002.

33. A.V. Koldoba, G.V. Ustyugova, P.S. Lii, M.L. Comins, S. Dyda, M.M. Romanova, and R.V.E. Lovelace. Numerical mhd codes for modeling astrophysical flows. *New Astronomy*, 45:60–76, May 2016.

34. Sigal Gottlieb and Chi-Wang Shu. Total variation diminishing runge-kutta schemes. *Mathematics of Computation*, 67, 08 1996.

35. S. May and M. Berger. Two-dimensional slope limiters for finite volume schemes on non-coordinate-aligned meshes. *SIAM J. Sci. Comput.*, 35, 2013.

36. Takahiro Miyoshi and Kanya Kusano. A multi-state HLL approximate Riemann solver for ideal magnetohydrodynamics. *Journal of Computational Physics*, 208(1):315–344, September 2005.

37. Toshiki Tajima. *Computational Plasma Physics*. Addison-Wesley Longman Publishing Co., Inc., USA, 1988.

38. Gábor Tóth, Yingjuan Ma, and T. Gombosi. Hall magnetohydodynamics on block-adaptive grids. *Journal of Computational Physics*, 227:6967–6984, 07 2008.

39. K. Tsubouchi. Alfvén wave evolution within corotating interaction regions associated with the formation of magnetic holes/decreases. *Journal of Geophysical Research (Space Physics)*, 114(A2):A02101, February 2009.

40. S. A. Orszag and C. M. Tang. Small-scale structure of two-dimensional magnetohydrodynamic turbulence. *Journal of Fluid Mechanics*, 90:129–143, January 1979.

41. Kamesh Sankaran. Simulation of plasma flows in self-field lorentz force accelerators. 01 2005.

42. T. Andreussi and F. Pegoraro. On the variational approach to axisymmetric magnetohydrodynamic equilibria. *Physics of Plasmas*, 15(9):092108, 2008.

REPORT DOCUMENTATION PAGE

Form Approved
OMB No. 0704–0188

1. REPORT DATE *(DD–MM–YYYY)*	2. REPORT TYPE	3. DATES COVERED *(From — To)*
17–06–2021	Master's Thesis	Sept 2019 — Jun 2021

4. TITLE AND SUBTITLE

One Dimensional Study of Magnetoplasmadynamic Thrusters for a Potential New Class of Heavy Ion Drivers for Plasma Jet Driven Magnetoinertial Fusion

5a. CONTRACT NUMBER

5b. GRANT NUMBER

5c. PROGRAM ELEMENT NUMBER

6. AUTHOR(S)

Patrick M. Brown

5d. PROJECT NUMBER

5e. TASK NUMBER

5f. WORK UNIT NUMBER

7. PERFORMING ORGANIZATION NAME(S) AND ADDRESS(ES)

Air Force Institute of Technology
Graduate School of Engineering and Management (AFIT/EN)
2950 Hobson Way
WPAFB OH 45433-7765

8. PERFORMING ORGANIZATION REPORT NUMBER

AFIT-ENP-MS-21-J-025

9. SPONSORING / MONITORING AGENCY NAME(S) AND ADDRESS(ES)

Defense Threat Reduction Agency
ATTN: Maj Nathaniel Kaminski
8725 John J Kingman Rd
Fort Belvoir, VA 2206-6201
845-938-0532

10. SPONSOR/MONITOR'S ACRONYM(S)

DTRA-RD-NSREC

11. SPONSOR/MONITOR'S REPORT NUMBER(S)

12. DISTRIBUTION / AVAILABILITY STATEMENT

DISTRIBUTION STATEMENT A:
APPROVED FOR PUBLIC RELEASE; DISTRIBUTION UNLIMITED.

13. SUPPLEMENTARY NOTES

14. ABSTRACT

Plasma Jet Driven Magnetoinertial Fusion (PJMIF) requires high velocity heavy ion drivers in order to compress a magnetized target to fusion conditions. Previous work with heavy ion drivers has revealed sub-par accelerations due to plasma instabilities; thus, it is necessary to investigate new methods of heavy ion plasma acceleration. One such method is Magnetoplasmadynamic (MPD) thrusters. Past studies of these thrusters have been conducted at an initial temperature at or below the energy of full ionization. Here MPD thrusters are investigated using a Godunov type MHD solver with an Harten-Lax van Leer-D (HLLD) flux solving scheme assuming the plasma is injected into the MPD thruster fully ionized.

15. SUBJECT TERMS

Plasma Physics, Computational MHD Modeling, Spacecraft Propulsion, Fusion Sciences, and Computational Fluid Modeling

16. SECURITY CLASSIFICATION OF:			17. LIMITATION OF ABSTRACT	18. NUMBER OF PAGES	19a. NAME OF RESPONSIBLE PERSON
a. REPORT	b. ABSTRACT	c. THIS PAGE			Dr. John W. McClory, AFIT/ENP
U	U	U	UU	191	19b. TELEPHONE NUMBER *(include area code)* (937) 255-3636, ext 7308, john.mcclory@afit.edu

Standard Form 298 (Rev. 8–98)
Prescribed by ANSI Std. Z39.18